UNIVERSIDAD AUTÓNOMA DEL ESTADO DE MORELOS

INSTITUTO DE INVESTIGACIÓN EN CIENCIAS BÁSICAS Y APLICADAS

CAMPUS NORTE

Correlación en simulaciones cosmológicas

TESIS QUE PARA OBTENER EL TÍTULO DE

DOCTOR EN CIENCIAS

PRESENTA EL M. EN C.

MIGUEL ENRÍQUEZ VARGAS

DIRECTOR

DR. JUAN CARLOS HIDALGO CUÉLLAR

CUERNAVACA, MORELOS 27 DE MAYO DE 2023

Acknowledgements

A mis padres Isabel y Miguel, que siempre han estado conmigo con su amor incondicional en las buenas y en la malas sabiendo que en cualquier momento podré contar con ellos. Definitivamente no sería la persona que soy ahora sin ellos. También por haberme dado sus consejos y experiencias de vida que me han servido mucho y que me seguirán sirviendo. Han sido mi modelo aseguir. Por todo esto y más, se los agradezco de corazón.

A mi abuelita Isabel que desde que soy pequeño y hasta el día de hoy, ha estado al cuidado de mí. Apoyándome para no salirme del camino con sus consejos, sus dichos y sus pláticas. Sin duda alguna también ha sido una base importante para ir cumpliendo mis metas.

A mis hermanas Carolina y Diana, con quienes siempre tendré un vínculo irrompible. Son y serán las personas en las que siempre contaré y sé que siempre estarán conmigo a pesar de cualquier eventualidad.

A mis asesores Juan Carlos Hidalgo y Octavio Valenzuela por su guía y paciencia en estos años de mis estudios de doctorado. Me abrieron el camino del conocimiento indudablemente.

Contents

List of Figures

Chapter One

Introduction

We present a method to implement relativistic corrections to the evolution of dark matter structures in Newtonian simulations of a ΛCDM universe via the initial conditions. We take the nonlinear correspondence between the Lagrangian (Newtonian) evolution of dark matter inhomogeneities and the synchronous-comoving (relativistic) matter density description, and use it to promote the relativistic constraint as the initial condition for numerical simulations of structure formation. In this case, the incorporation of Primordial non-Gaussianity (PNG) contributions as initial conditions is straightforward. We implement the relativistic, f_{NL} and g_{NL} contributions as initial conditions for the L-PICOLA code, and compute the power spectrum and bispectrum of the evolved matter field. We focus specifically on the case of largest values of non-Gaussianity allowed at $1-\sigma$ by Planck observations ($f_{NL} = -4.2$ and $g_{NL} = -7000$). As a checkup, we show consistency with the one-loop perturbative prescription and with a fully relativistic simulation (GRAMSES) on the adequate scales. Our results confirm that both relativistic and PNG features are most prominent at very large scales and for squeezed triangulations. We discuss future prospects to probe these two contributions in the bispectrum of the matter density distribution.

The expected result was obtained where the greatest difference was

found in the bispectrum, since the 3-point correlation function mostly detects deviations from the Gaussian distribution. This difference was greater at the maximum scale that could be reached, which was at $k = 10^{-2}h/Mpc$. For the case where PNG is included with previously mentioned parameters of f_{NL} and g_{NL}, it was 4% in the difference power spectrum with respect to the Gaussian simulations and 10% in the bispectrum with a squeezed triagulation. In the case of PNG and relativistic contributions, the difference was 6% in the power spectrum and 15% in the bispectrum. In the reduced bispectrum, it was denoted that a local triangulation (squeezed type) there is a greater difference with respect to the Gaussian simulation. There was also agreement with simulations where the initial conditions are Newtonian and the gravitational evolution is relativistic. These results have been published [2].

State of art

In cosmology there are several models that are being accepted or discarded given the observational precision. With current surveys such as DESI [3], [4] and Euclid [5], there is a particular interest in analyzing the Primordial Non-Gaussianity, which is the information on the primordial distribution of matter that contains information on the Universe in the inflation process. These Gaussinity deviations have a slight impact on the distribution of matter today, which is why more precise observations are necessary, such as the previously mentioned surveys. Another phenomenon of interest at present is the inclusion of relativity, which its variation with respect to the Newtonian equations in certain cases usually has an undetectable impact for now (however existing).

The most effective way to test the different models that try to explain the observations is through numerical simulations. To date, there are high-resolution simulations with codes such as Gadget [6] that allow

us to simulate the gravitational evolution of the distribution of matter density. These codes have an adaptive mesh, in order to solve the corresponding Newtonian gravitational equations taking clusters of particles as a single mass that are far away and solving these equations particle by particle in nearby areas. However, these codes tend to be highly computationally expensive. An alternative is the current fixed-grid codes such as L-PICOLA [7], [8] which lose a bit of resolution at small scales with considerably less computational cost, however they have shown good agreement with large-scale adaptive mesh codes. If studies are being carried out where the impact phenomenon is found on large-scales, these codes are usually the most appropriate. There are codes that implement the inclusion of PNG in the initial conditions e.g. [9], [10] through the parameter F_{NL} which corresponds to a parameter in the perturbative expansion of the curvature of space. However, studies are needed that include higher perturbative orders that improve the accuracy of the simulations. Similarly, although there are codes whose gravional evolution is relativistic [11], [12], but more studies are needed to implement relativistic aspects in the initial conditions. This information is usually analyzed with high-order correlation functions such as the bispectrum and the trispectrum. In surveys such as DESI, projects such as the Mock Challenge have emerged to analyze the different existing codes to select those that are going to be used formally for the statistical study of the survey observations.

Thesis outline

Chapter Two presents, first of all, the necessity of an initial scenario where the Universe had to have an era of exponential expansion. The theoretical background to physics of the Inflation is explained, in order to understand the origin of overdensities (primordial perturbations) and

why the detection of Primordial non-gaussianty is not an easy measurement to detect. Also described is the structure formation from these overdensities as the Baryonic Acoustic Oscillation. Through the use of certain astrostatistics tools, such as the two and three point correlation function, we will explain this relationship through Fourier's transform with the matter power spectrum and bispectrum, and how this will give us information about the PNG created by the potential generated in the primordial density perturbation. Also is all the background of the perturbation theory, the importance and utility it has. We describe the Standard Perturbation Theory in the linear regime and with the one-loop correction and we also describe the Zel'dovich approximation. Then we proceed to describe by means of a change of coordinates from Eulerian to Lagrangian through the desplacement field to obtain the Lagrangian Perturbation Theory and how to obtain the correction of one-loop for the Power spectrum through two different ways of expanding the cumulant involved. Then we will apply a chosen resummation to obtain the one-loop correction to the bispectrum. In Chapter Three is the implementation of the said previously into codes such as L-PICOLA, which is the main part of this Thesis we compute the power spectrum and bispectrum to measure the differences between PNG and PNG initial conditions into N-body simulations. And Finally the conclusions and possible work that can be done in the line of this Thesis. We find differences of 10% int he power spectrum and 16% in the bispectrum at large-scales by implementing PNG and relativistic contributions to the initial conditions. For the future work, there is a possible study of the power spectrum and bispectrum of the voids. This is of interest because voids are low matter density zones where the non-linearities due evolution are minimal, so the primordial state of the universe is less affected. Also the formation of halos may be affected due the PNG so is also work that can be done further this project.

Chapter Two

Preliminaries

2.1 Cosmology with General Relativity

In order to have a more profound comprehension of cosmology, what is first needed is to understand the concepts of General Relativity (GR). Also, most of the information is obtained through observations of the electromagnetic spectra, for example, to compute distances we have to consider not just the continuous expansion of space, but also the relativistic effects of the light.

The infinitesimal distance between points in GR is defined by the metric tensor $g_{\mu\nu}$

$$ds^2 = -g_{\mu\nu}dx^\mu dx^\nu \quad . \tag{2.1}$$

We use the convention that the coordinate x^0 denotes time and the metric signature is $\{-,+,+,+\}$.

We will use the cosmological principle that states that viewed on a sufficiently large scale, the properties of the Universe are the same for all observers. The physical conditions of homogeneity and isotropy restrict the space-time to the possibilities of the Friedmann-Lemaitre-Robertson-Walker metric (FLRW metric).

2.1.1 FLRW metric

The FLRW metric in spherical coordinates is

$$ds^2 = dt - a^2(t)\left[\frac{dr^2}{1-kr^2} + r^2(d\theta^2 + \sin^2\theta d\phi^2)\right] \quad , \tag{2.2}$$

where k describes the 3D space curvature which can be positive ($k > 0$), negative ($k < 0$) or flat ($k = 0$). The curvature factor has units of length^{-2}. The term $a(t)$ is the *scale factor* and describes the expansion or contraction of the Universe. We will use the convention as value of the scale factor for today $a(t_0) = 1$. The behavior of the scale factor can be expressed by the expansion rate of the Universe called the Hubble parameter:

$$H(t) = \frac{\dot{a}}{a} \quad . \tag{2.3}$$

From the FLRW metric, the Ricci tensor and scalar can be defined to be introduced in the Einstein equations, which in turn will define the evolution of the scale factor through this Hubble parameter.

2.2 Distances in cosmology

The redshift has been a useful way to measure how far an object is. The redshift is defined as the fractional difference of the emitted wavelenght λ_1 over the observed wave λ_0 as:

$$z \equiv \frac{\lambda_0 - \lambda_1}{\lambda_1} \quad , \tag{2.4}$$

2.2.1 Comoving distance

The light we observe from the objects in the sky, travels along the ξ coodinate which satisfies the geodesic equation. If the light of an object

is emitted at time $t = t_1$ with a comoving distance $\xi = \xi_1$, arrives the observer at $t = t_0$, is a flat space space is considered, we obtain:

$$d_c \equiv \xi_1 = \int_0^{\xi_1} d\xi = -\int_{t_0}^{t_1} \frac{c}{a(t)} dt \quad , \tag{2.5}$$

using the redshift definition (2.4):

$$d_c = \frac{c}{a_0 H_0} \int_0^z \frac{d\tilde{z}}{E(\tilde{z})} \quad , \tag{2.6}$$

where

$$E(z) \equiv \frac{H(z)}{H_0} \tag{2.7}$$

2.3 Contents of the Universe and ΛCDM model

The Einstein field equations relate the metric with the energy content of the Universe in the energy-momentum tensor $T_{\mu\nu}$ as follows:

$$R_{\mu\nu} - \frac{1}{2} g_{\mu\nu} R = -8\pi G T_{mu\nu} - \Lambda g_{\mu\nu} \quad , \tag{2.8}$$

where the Ricci tensor $R_{\mu\nu}$ and the Ricci scalar R are related with the deformation of space-time and G is the gravitational constant. The term Λ was introduced by Einstein in order to have a static Universe, but today it is used to explain the expansion [13].

We can treat the Universe as a perfect fluid considering the cosmological principle and assumptions such as: that the distribution of matter can be considered collisionless and that there is no viscosity. So the energy-momentum tensor in the proper frame would be

$$T_{\mu\nu} = \begin{pmatrix} \rho & 0 & 0 & 0 \\ 0 & p & 0 & 0 \\ 0 & 0 & p & 0 \\ 0 & 0 & 0 & p \end{pmatrix} \tag{2.9}$$

where ρ is the mass density and p the pressure.

With the FLRW metric and the energy-momentum tensor inserted in the Einstein field equations, these can now be derived into the Friedman equations

$$\left(\frac{\dot{a}}{a}\right)^2 = \frac{8\pi G}{3}\rho - \frac{k}{a^2} + \frac{\Lambda}{3} \quad , \tag{2.10}$$

$$\frac{\ddot{a}}{a} = -\frac{4\pi G}{3}(\rho + 3p) + \frac{\Lambda}{3} \quad , \tag{2.11}$$

where (2.10) describes the expansion rate from the components and curvature of the Universe and (2.11) describes the acceleration as function of the pressure and density. From these two equations, or from the energy-momentum conservation equations, one may derive the following energy density conservation equation :

$$\dot{\rho} = -3H(p + \rho). \tag{2.12}$$

The pressure p and the density ρ are related via the equation of state

$$p = w\rho \quad , \tag{2.13}$$

where the parameter w changes accordingly to describe the different ingredients of the Universe; for non-relativistic matter $w = 0$ and for relativistic particles (as neutrinos or photons) $w = 1/3$. The accelerated expansion of the Universe can be achieved via equation ((2.11)) through a fluid with a negative equation of state $w < -1/3$ of a positive cosmological constant.

If we assume that all the components do not interact with each other, then the total density and pressure can be written as:

$$\rho(a) = \rho_m(a) + \rho_r(a) + \rho_\Lambda \quad , \qquad p(a) = \frac{\rho_r(a)}{3} - \rho_\Lambda \quad . \tag{2.14}$$

The parameter left to be determined is the curvature, which tells us if the Universe is flat, closed or open. First, we have to define the *critical*

density which is the total energy density in a flat Universe:

$$\rho_{crit}(a) = \frac{3H^2(a)}{8\pi G} \quad . \tag{2.15}$$

We can normalize the density of each ingredient with ρ_{crit} to obtain the density parameters

$$\Omega_m(a) = \frac{\rho_m}{\rho_{crit}(a)} \ , \Omega_r(a) = \frac{\rho_r}{\rho_{crit}(a)} \ , \Omega_\Lambda(a) = \frac{\rho_\Lambda}{\rho_{crit}} \ , \tag{2.16}$$

so the total density would be:

$$\Omega_{tot}(a) = \Omega_m(a) + \Omega_r(a) + \Omega_\Lambda = 1 + \frac{k}{(aH)^2} \quad , \tag{2.17}$$

where the RHS is obtained from the equations (2.10). If the total density is higher than ρ_{crit} then $k > 0$, this indicates that the Universe is closed. If $\Omega_{tot} > \rho_{crit}$ then $k < 0$, this indicates that the Universe is open and, if $\Omega_{tot} = \rho_{crit}$ then $k = 0$, this indicates that the Universe is flat.

In terms of the density parameters, equation (2.11) can be written as

$$H^2(a) = H_0 \left[\frac{\Omega_r}{a^4} + \frac{\Omega_m}{a^3} + \frac{1 + \Omega_{tot}}{a^2} + \Omega_\Lambda \right] \quad , \tag{2.18}$$

where we can notice how all the components contribute to the expansion of the Universe. We can numerically solve equation (2.18) to have the age of different universes with different components.

Thus we can use observations to compare and have information of our Universe and understand its behavior. For example, it would be possible to know if the Universe will expand forever, if it will reach an equilibrium point between matter and expansion, or if it will have a Big Bounce.

2.3.1 Cosmological observations

Ever since humankind started analyzing the sky, different observations, each more sophisticated than the previous, have been registered. For

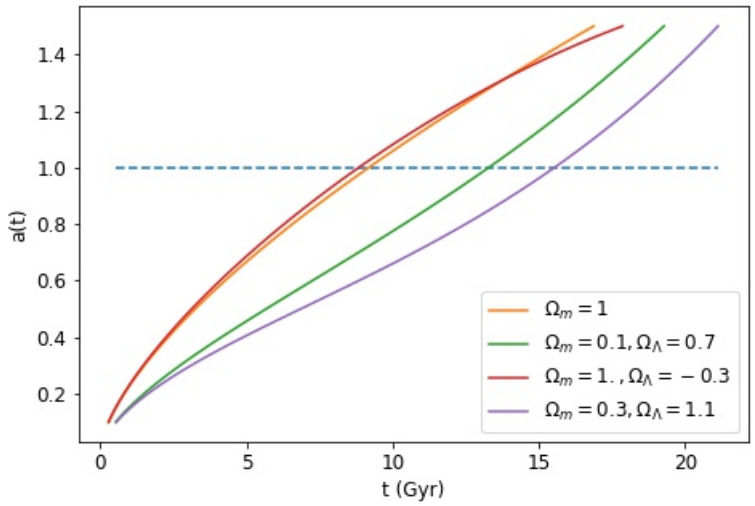

Figure 2.1 $a(t)$ versus t for different values of the components of equation (2.18).

example, in 1929, Edwin Hubble [14] measured the radial velocities of extragalactic nebulae and concluded that the Universe was expanding. This allowed for the establishment of Hubble's law, $v = H_0 D$.

Observations also lead us to understand the different phenomena that have happened in the history of our Universe, like the almost accidental, discovery of cosmic microwave background radiation (CMB) by Penzias & Wilson [15])

Actually the percentage of the components of the Universe hs been very well inferred through the best concordance model with CMB, BAO and SN1A observations (see following sections).In Figure 2.2 we can see the confidence interval for different observations at 68%, 95%, and 99.7% constraints on Ω_Λ and Ω_m, and the three methods of observations agree with a very nearly flat Universe ($k \sim 0$), a content of matter $\Omega_m \sim 0.3$ and a content of cosmological constant $\Omega_\Lambda \sim 0.7$ [16].

We are currently in the era of precision cosmology where observations

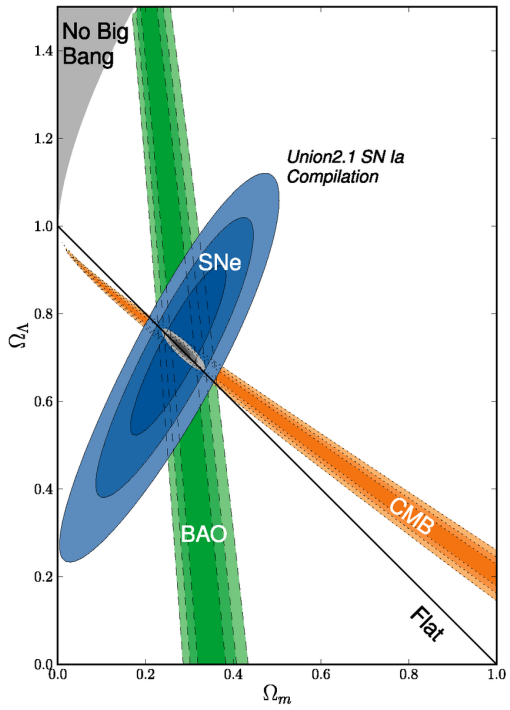

Figure 2.2 Concordance of CMB, BAO, and SNIa observations. The respective error ellipsoids are shown on the $\Omega_m - \Omega_\Lambda$ plane. [16].

now have a statistical minimal error that has never been seen before. This will allow us to compare different cosmological models and know which one better describes our Universe.

Today one of the most important surveys is the Dark Energy Spectroscopic Instrument (DESI), which will produce the best measurement of the Baryonic Acoustic Oscillations (BAO) by a spectroscopic survey over 14,000 sq. degrees. DESI will observe 4 million luminous red galaxies (LRGs), 18 million emission line galaxies (ELGs) and 2.4 million quasars (QSOs) [3].

2.3.2 Big Bang & Thermal history

Different models have tried to explain the origin and evolution of the Universe, but the one that has given more correct answers is the Big Bang model proposed by Georges Lemaître [17], which explains the observations of:
1. Redshift of galaxies. Distant galaxies have shown a shift to lower frequencies in the electromagnetic spectrum. This can be detected by the Lyman-alpha forest [18].
2. Microwave radiation. Our whole Universe was in a very hot, dense state and as it expanded, the heat left a small radiation footprint that can be detected in any direction of the sky [15].
3. Mixture of elements. Some of the elements we detect today were created in the early Universe. The Big Bang predicts in a very precise way how many of these have been made. [19].
4. Looking back in time. Before the Big Bang theory, there was the Steady State theory which established that the Universe is basically the same at any time as well as in any place [20], and this does not explain the different types of stars that we can observe as far as we see.

We can describe the *Thermal history* of the Universe as follows:

The early Universe The early Universe has been full of speculative theories because of the lack of information that we have from this epoch; as well as because our laws of physics can not describe what happened with all the matter contained in a very confined space with huge amounts of pressure and temperature. Alan Guth proposed the inflationary model [21] which happened between 10^{-35} and 10^{-32} caused by a scalar field that dominated the energy density of the Universe. An observational problem of this is that we can not see anything before recombination. The possibility of detecting something further to the CMB with gravitational waves exists but the sensitivity of our instruments is

not high enough. At the end of inflation, the Universe returned to the pre-inflationary temperature, which is called *reheating*.

Radiation domination Given that neutrinos only interact via weak force, these were the first to decouple from the initial plasma. This left a footprint before the CMB, but these particles are too difficult to detect. We can solve equation (2.10) for each component to analyze how the growth factor which is:

$$a(t) \sim t^{1/2} \quad , \tag{2.19}$$

where we can conclude that the expansion no longer has an exponential behavior. The initial density fluctuations started to grow because of the gravitational interactions but baryons and radiation still coupled to each other because of the high pressure and temperature. Figure 2.3 shows solutions for different components of the Universe considering them independent of each other.

Big Bang Nucleosynthesis (BBN)

The Universe kept cooling down until, when it reached few MeV, protons and neutrons could form the first elements. This is limited to Helium because of the slightly existent bonds between them. BBN predicts the primordial abundances of light elements very accurately. In Figure 2.4 we can see the observations (red line) of the Wilkinson Microwave Anisotropy Probe (WMAP) and the predictions of light elements; and as can be seen, a good concordance can be appreciated between them.

Matter domination

We can find a solution for equations (2.11) considering an Einstein-deSitter universe where $\Omega_{tot} = \Omega_m = 1$, this means without cosmological

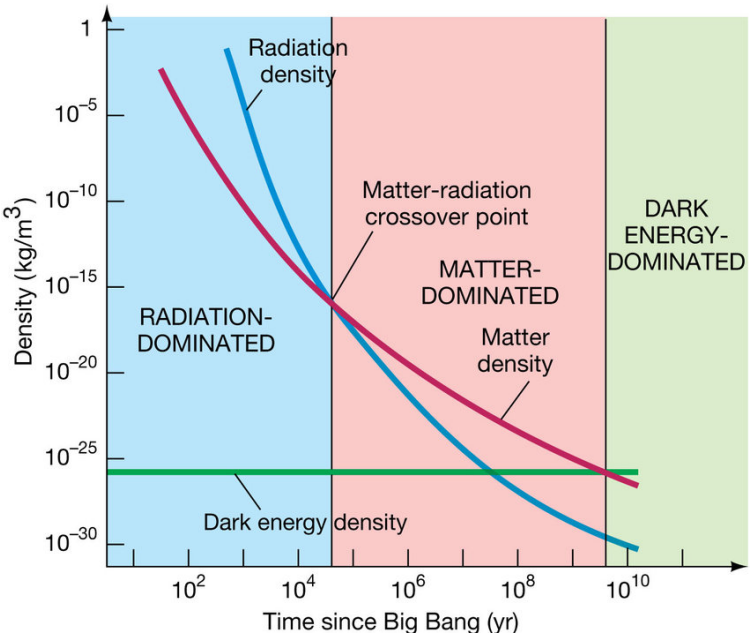

Figure 2.3 Solutions for the scale factor for different components [22].

constant, and the solution is

$$a(t) \sim t^{2/3} \quad . \tag{2.20}$$

In Figure 2.3 we can appreciate that this happened around $z \sim 4800$ and finished in $z \sim 0.6$ where the cosmological constant Λ started to dominate. In this era the universe had a slower expansion rate, and it is here that all the large-scale structures happened. As the astronomical observations became more precise, the amount of visible matter was measured, but the cosmological and astrophysical models could not reproduce the data observed. Fritz Zwicky studied the galaxy clusters [24] by analyzing the Coma Cluster through the virial problem and obtained evidence of unseen mass needed to maintain the galaxy cluster together. Another need of considering more matter than just the visible one is the galaxy rotation curves. The luminous mass density of a spiral galaxy decreases

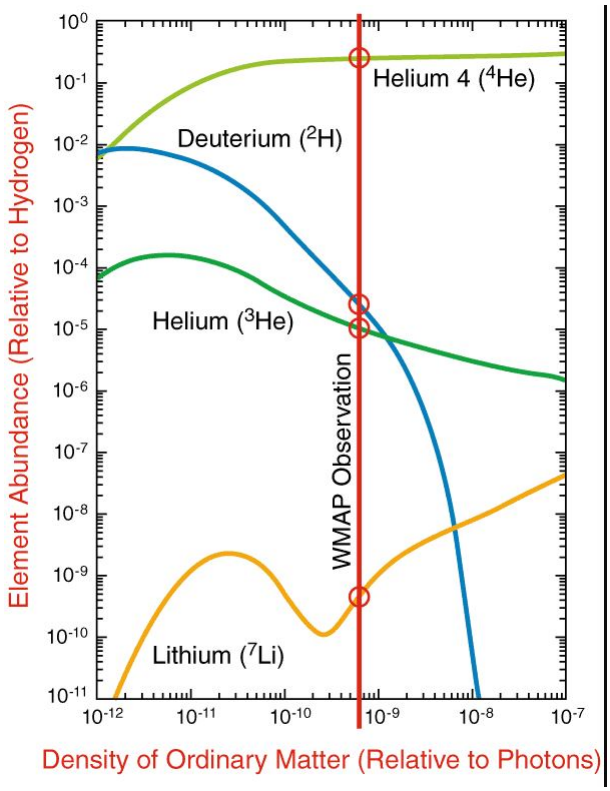

Figure 2.4 WMAP observations and BBN predictions [23].

from the center to the outskirts so, based on Kepler's second law, one would expect that the rotation velocities of stars would be decreasing. However, this is not the case. As we can see in Figure 2.5, the predicted curve of the luminous matter can not reproduce the observations from the NGC 6503 galaxy rotation curve, instead, considering dark matter in and halo around, the observations are clearly well reproduced.

Recombination and CMB Baryons started to fall into the gravitational potentials of dark matter but, due to the remaining coupling of photons, their pressure prevented a collapse of matter. This bouncing is the so-called Baryonic Acoustic Oscillations (BAO) that is imprinted on the CMB and can also be measured in galaxy clustering. The Universe

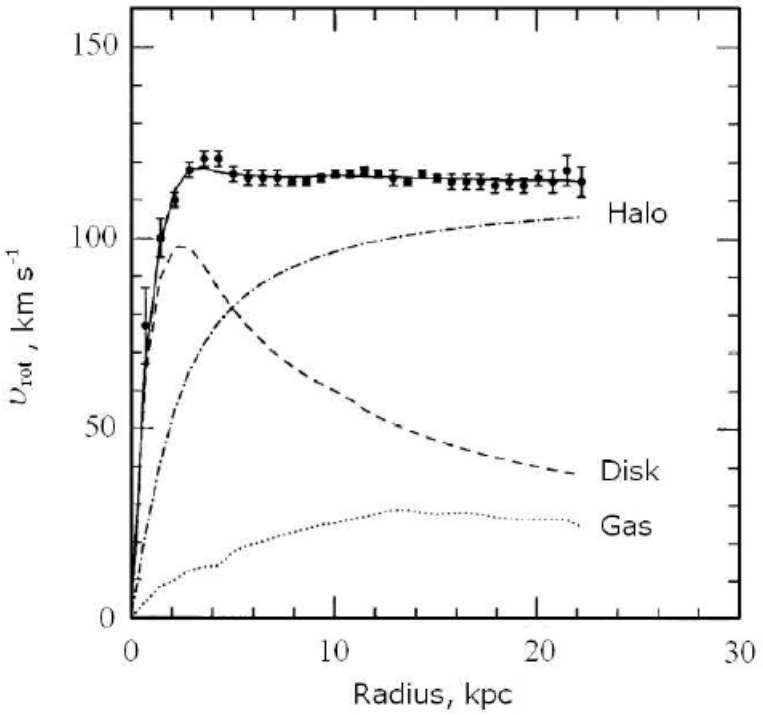

Figure 2.5 Rotation curves predicted and observed [25].

was still cooling down and when it reached ∼4000 K, electrons and photons finally decoupled and electrons combined with protons to neutral H and photons left a footprint which is the CMB. The dark ages of the Universe correspond to when there were no light producing objects such as stars. The overdensities continued to attract more matter until neutral H became so dense that it began a fusion process which generated the first stars and galaxies.

Re-ionization and galaxy formation Now that the Universe is transparent to photons, the radiation of the stars can re-ionize the surrounding neutral medium. The dwarf galaxies play an important role in this epoch because even though their luminosity is low, they are very numerous and were the primary source of ionizing photons. Re-ionization was still not very constrained but estimations suggest between $z = 12$

and $z = 6$ [26].

Cosmological constant domination era The last component of the Universe to dominate the expansion rate is the cosmological constant, solving equation (2.11) for Λ results

$$a(t) \sim e^{H\ t} \quad . \tag{2.21}$$

This is called the late-time accelerated expansion and started at $z \sim 6$, about 5.6 Gyrs ago. The Universe changed from decelerating into accelerating its expansion. The history of expansion has been observed with different objects such as standard candles. As stated before, luminosity is the biggest piece of information we have from astronomical objects, so measuring the distance is not trivial. If we know the physical process of the formation of an object, we van determine their theoretical luminosity and knowing the distance from the absolute magnitude and apparent magnitude through the relation

$$5 \cdot \log_{10} D = m - M - 10 \tag{2.22}$$

A usual standard candle is the type Ia Supernova (SN Ia); the process of formation of them SN has been very well studied. In a binary system, in which one of the is a white dwarf, eventually, because of its high density, the stellar matter of the companion star starts to be accreted into the white dwarf until it reaches the Chandrasekhar mass and generates the SN Ia. The observations of SN Ia are shown in Figure 2.6. The solid red line is ΛCDM model with Ω_m=0.3, Ω_Λ=0.7 and Ω_k=0 and the solid blue line is the cosmological model with Ω_m=1, Ω_Λ=0 and Ω_k=0 and it can be appreciated that the fiducial model ΛCDM is very consistent with the observations.

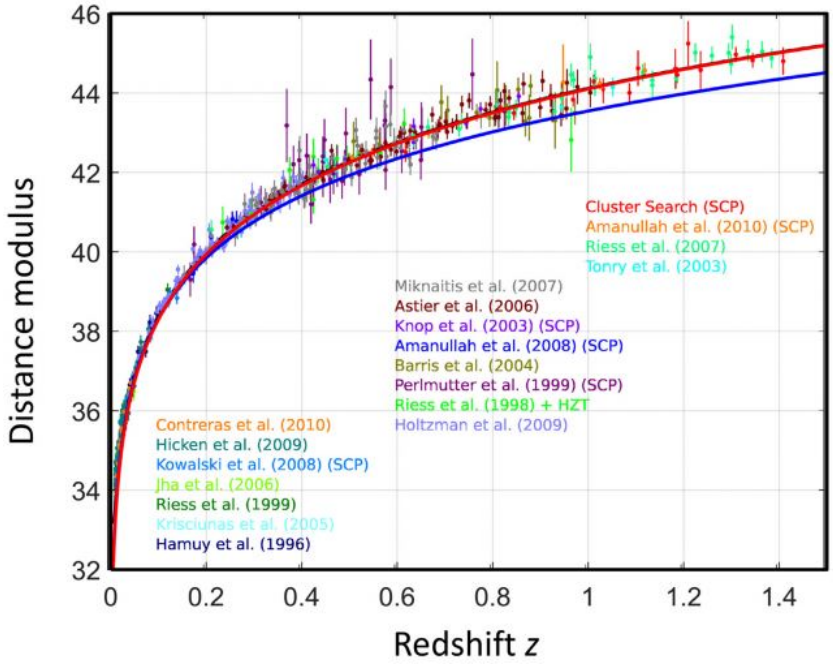

Figure 2.6 Distance modulus of SN Ia, fiducial ΛCDM model (red line) and Ω_m=0.3, Ω_Λ=0.7 and Ω_k=0 model [27].

2.4 Inflation

If we consider a completely homogeneous and isotropic matter distribution in the Universe at all scales, this would simply keep the Universe in an equilibrium state forever. In order to have structures such as stars, galaxies, clusters, etc., the primordial Universe may have had some sort of perturbations. The earliest picture we have with high detail of the Universe, is the CMB which shows temperature differences of the order of 10^{-5} of amplitude. These tiny perturbations correspond to density perturbations where initial overdense regions accrete more matter. The theory of inflation (section 2.4) is used to predict the origin and formation of these primordial overdensities and give answers to the *Flatness problem* and the *Horizon problem* of standard Big Bang cosmology. The recent discovery of the Higgs Boson provided a connection between the

early Universe and the actual standard model of particle physics because most models of inflation depend on one or more scalar fields which were, up to the experimental confirmation of the Higgs existence [28]. Another important component for the origin of the structure of the Universe is the Primordial non-gaussianity (PNG) which can be proof of the inflationary process. The detection of PNG is currently a big observational but, maybe in the near future, with observations of Large-scale structures (LSS) we might have the precision required to detect PNG more precisely and have a better description of the primordial Universe.

The physics of inflation give us the parameter we will need to establish our initial conditions for structure formation. The Inflationary model proposed by Alan Guth [21] provided a solution to more than one problem of the standard big bang theory.

The Flatness Problem: From equation (2.17) we can describe the curvature k as a function of time as

$$1 - \Omega_{tot}(a) = -\frac{k}{(aH)^2} \quad , \tag{2.23}$$

where the term aH is the comoving Hubble radius thus,

$$1 - \Omega(t) = \frac{H_0^2(1-\Omega_0)}{H^2(t)a^2(t)} \quad . \tag{2.24}$$

For when the Universe was dominated by matter and radiation only

$$\frac{H^2}{H_0^2} = \frac{\Omega_{r,0}}{a^4} + \frac{\Omega_{m,0}}{a^3} \quad , \tag{2.25}$$

then equation (2.24) becomes,

$$1 - \Omega(t) = \frac{(1-\Omega_0)a^2}{\Omega_{r,0} + \Omega_{m,0}a} \quad . \tag{2.26}$$

At the matter domination era where $a \sim t^{2/3}$,

$$1 - \Omega(t) = \frac{1-\Omega_0}{\Omega_{m,0}} \left(\frac{t}{t_0}\right)^{2/3} \quad . \tag{2.27}$$

Comparing equation (2.26) and (2.27), we appreciate that the curvature we observe today, which is very close to zero, with Ω_0 very close to 1, means that in the beginning the Universe has even flatter, with the curvature even closer to zero. Another important fact is that the sign of the curvature remains constant, so if the Universe was open in the beginning, it can not become a closed one and vice-versa. This initial flatness of our Universe finds no explanation in a Big Bang Universe dominated by radiation at early times. Primordial inflation provides an answer as we can see below.

The Horizon problem If we consider a beam of light emitted at coordinate r_e and time t_e, recived by an observer at r_o and time t_o in the FLRW metric, then the relation of time and distance is given by:

$$\int_{t_e}^{t_o} \frac{c\ dt}{a(t)} = \int_{r_o}^{r_e} \frac{dr}{\sqrt{1-kr^2}}. \tag{2.28}$$

If the emitted light frequency is ν_e, then the period is $\Delta t_e = 1/\nu_e$, then the second crest of the wave is:

$$\int_{t_e+\Delta t_e}^{t_o+\Delta t_o} \frac{c\ dt}{a(t)} = \int_{r_o}^{r_e} \frac{dr}{\sqrt{1-kr^2}}, \tag{2.29}$$

considering that the difference of Δt_o and Δt_e is small enough to establish that $a(t+\Delta t) \sim a(t)$, then:

$$\frac{\Delta t_o}{\Delta t_e} = \frac{a(t_e)}{a(t_o)} = \frac{\lambda_o}{\lambda_e}\ . \tag{2.30}$$

We define as redshift parameter, the change in the emitted light as:

$$z \equiv \frac{\lambda_o - \lambda_e}{\lambda_e} = \frac{\lambda_o}{\lambda_e} - 1. \tag{2.31}$$

The light speed sets how far the an emitted signal can be reached by an observer located at $r = 0$. The Big Bang model establishes that

$R(t) = 0$, so $R(t)\int_0^t \frac{cdt'}{R(t')}$ is the maximum distance that a light beam emitted at t=0 can reach. We call the proper distances of the horizon:

$$d_H(t) = R(t)\int_0^t \frac{cdt'}{R(t')} = (t)\int_0^{r_H} \frac{dr}{\sqrt{1-kr^2}}, \tag{2.32}$$

if we consider a universe with $k = 0$ at radiation dominated era as $R(t) \propto t^{1/2}$ we obtain:

$$d_H(t) = t^{1/2}\int_0^t \frac{cdt'}{t^{1/2}} = 2ct\ . \tag{2.33}$$

Considering a universe in the matter dominated era where $R(t) \propto t^{2/3}$:

$$d_H(t) = t^{2/3}\int_0^t \frac{cdt'}{t^{2/3}} = 3ct\ . \tag{2.34}$$

For the cosmic background radiation, the physical distance from the source at the time of emission, is:

$$d_{CBR}(t_e) = R(t_e)\int_{t_e}^{t_o} \frac{cdt}{R(t)}. \tag{2.35}$$

But at the time of emission, the radiation was coming from opposite directions, so the physical distance was approximately:

$$d_{sep} = 2d_{CBR}(t_e), \tag{2.36}$$

and the size of the horizon at the time of emission was:

$$d_H(t_e) = R(t_e)\int_0^{t_e} \frac{cdt}{R(t)}. \tag{2.37}$$

We can calculate the separation ratio to the horizon size to know which regions were in causal contact. To do this, we can look to the ratio, if it is greater than 1, the horizon of two regions were outside of each other and if the ratio is greater than 2, there is no causal contact:

$$\frac{d_{sep}(t_e)}{d_H(t_e)} = \frac{2\int_{t_e}^{t_o} \frac{cdt}{R(t)}}{\int_0^{t_e} \frac{cdt}{R(t)}}, \tag{2.38}$$

for a matter-dominated universe and $k = 0$:

$$d_{sep}(t_e) = 2R(t_e) \int_{t_e}^{t_o} \frac{cdt}{R(t)} = \frac{6ct_o R(t_e)}{R(t_o)} \left(1 - \left(\frac{t_e}{t_o}\right)^{1/3}\right) \tag{2.39}$$

$$d_H(t_e) = R(t_e) \int_0^{t_e} \frac{cdt}{R(t)} = \frac{3ct_o R(t_e)}{R(t_o)} \left(\frac{t_e}{t_o}\right)^{1/3} \tag{2.40}$$

$$\frac{d_{sep}(t_e)}{d_H(t_e)} = 2\left(\left(\frac{t_o}{t_e}\right)^{1/3} - 1\right), \tag{2.41}$$

where in terms of the redshift:

$$1 + z = \frac{R(t_o)}{R(t_e)} = \left(\frac{t_o}{t_e}\right)^{2/3} \tag{2.42}$$

$$\frac{d_{sep}(t_e)}{d_H(t_e)} = 2\left((1+z)^{1/2} - 1\right). \tag{2.43}$$

Considering that the microwave background radiation was emitted ad $z = 1500$, the separation distance was 80 times the horizon distance at the time of emission.

2.4.1 Accelerated expansion

The acceleration of the scale factor is defined as:

$$\frac{\ddot{a}}{a} = \dot{H} + H^2 = H^2\left(1 + \frac{\dot{H}}{H^2}\right) = H^2(1 - \varepsilon_H) \quad , \tag{2.44}$$

where ε_H is defined as the first of the slow roll parameters. In order to guarantee the acceleration of the expansion, the equation has to satisfy:

$$\frac{\ddot{a}}{a} > 0 \longrightarrow 0 < \varepsilon_H < 1 \quad . \tag{2.45}$$

The number of e-folds is defines as:

$$dN = -Hdt \quad , \tag{2.46}$$

this parameter refers to the power of e at which the universe expands from the start of the Big Bang (or the end of inflation). Considering a period of primordial inflation, this parameter is thus counted backwards from the end of inflation $N = 0$ and before the end of inflation $N = 60$.

Slow-roll

Given an initial scalar field ϕ_0 that hypothetically dominated the early universe, the inflation evolution would be given by the equation:

$$\ddot{\phi}_0 + 3H\dot{\phi}_0 + V'(\phi_0) = 0 \quad , \tag{2.47}$$

where V is the potential. The slow-roll name is because it is required that $\dot{\phi}_0^2 << V(\phi_0)$. The FLRW equation is then:

$$H^2 \sim \frac{8\pi G}{3} V(\phi_0) \quad , \tag{2.48}$$

where only the inflation is considered as energy contribution of the Universe. The equation of motion is then:

$$3H\dot{\phi}_0 = -V'(\phi_0) \quad , \tag{2.49}$$

now is related $\dot{\phi}_0$ as function of the potential. So the slow-roll model has the condition:

$$\dot{\phi}_0^2 << V(\phi_0). \tag{2.50}$$

2.4.2 Inflation fluctuations

During inflation, quantum fluctuation surged and then imprinted in the curvature fluctuations which grew as matter started accumulating in such a host for condensations. These quantum fluctuations were stretched out of casual contact during inflation. A perturbation in a scalar field (in this

case, the inflation field) ϕ, corresponds to a perturbation of the energy-momentum tensor, $\delta\phi \longrightarrow \delta T_{\mu\nu}$. Which leads to Einstein equations as:

$$\delta R_{\mu\nu} - \frac{1}{2}\delta(g_{\mu\nu}R) = 8\pi G\delta T_{\mu\nu} \quad , \tag{2.51}$$

where it is seen that this perturbations also generates perturbations in the metric $\delta g_{\mu\nu}$, Thus we can evaluate perturbations from the metric the density fluctuations. For instance, perturbing the Klein-Gordon equation we have:

$$\delta\left(-\partial_\mu\partial^\mu\phi + \frac{\partial V}{\partial\phi}\right) = 0 \quad , \tag{2.52}$$

where it is seen that the perturbations of inflation and the perturbations of the metric $\delta\phi \longrightarrow \delta g_{\mu\nu}$ are coupled. For the scalar field with the perturbation $\phi(\boldsymbol{x}) = \phi_0(t) + \delta\phi(\boldsymbol{x})$, it satisfies the equation of motion:

$$\delta\ddot{\phi} + 3_H\delta\dot{\phi} - \frac{\nabla^2\delta\phi}{a^2} + V''\delta\phi = 0 \quad , \tag{2.53}$$

For the limit $k/a << H$, the gradient term can be neglected and yielding that $\dot{\phi}_0$ and $\delta\phi$ solve the same equation, thus both quantities are related just by a constant of proportionality such as:

$$\phi = -\dot{\phi}_0\delta t(\boldsymbol{x}) \quad , \tag{2.54}$$

which lead us to the form of $\phi(\boldsymbol{x}, t)$ as:

$$\phi(\boldsymbol{x}, t) = \phi_0(\boldsymbol{x}, t) - \delta(t, \boldsymbol{x}) \quad . \tag{2.55}$$

This tells us that the inflation field has fluctuations so the scalar field is not homogeneous. These fluctuations have effects in the space curvature that can also be parameterized by the number of e-folds such as:

$$-\zeta = \delta N = \delta N(\phi(\boldsymbol{x}, t)) \implies \frac{\partial N}{\partial\phi}\delta\phi = \frac{\partial N}{\partial t}\frac{\delta\phi}{\ddot{\phi}} = H\frac{\delta\phi}{\ddot{\phi}} \quad , \tag{2.56}$$

where the metric perturbation is expressed in terms of the linear curvature perturbations where non-linear primordial contributions is given by the expansion:

$$\zeta = \frac{\partial N}{\partial \phi}\delta\phi + \frac{1}{2}\frac{\partial^2 N}{\partial \phi^2}\delta\phi \quad . \tag{2.57}$$

Details will be described on later sections.

2.5 Perturbation theory

2.5.1 Newtonian treatment

In cosmology, two common choices of coordinates are: proper coordinates and comoving coordinates. The proper radius r and the comoving coordinate x where the relation between them is:

$$r = ax \quad . \tag{2.58}$$

The Nabla operators ($\nabla = \frac{\partial}{\partial x}$ and $\nabla_r = \frac{\partial}{\partial r}$) are related through

$$\nabla_r = \frac{1}{a}\nabla \tag{2.59}$$

Let us focus on a universe with pressureless matter and no cosmological constant, this is called Einstein de-Sitter Universe. The continuity equation in proper time coordinates is established as:

$$\frac{\partial}{\partial t}\rho + \nabla_r(\rho u) = 0 \tag{2.60}$$

Expanding the second term we get:

$$\frac{\partial}{\partial t}\rho + u \cdot \nabla_r \rho + \rho \nabla_r \cdot u = 0 \tag{2.61}$$

We observe that the first two terms, form the convective derivative of ρ, so the previous equation is:

$$\frac{d}{dt}\rho + \rho \nabla_r \cdot u = 0 \tag{2.62}$$

In comoving coordinates we get:

$$\frac{1}{a}\frac{d}{d\tau}\rho + \frac{1}{a}\rho \nabla \cdot u = 0 \tag{2.63}$$

Using the conformal convective derivative and the absolute velocity u:

$$\frac{d}{dt}\rho + 3H\rho + \nabla \cdot (\rho v) = 0. \tag{2.64}$$

In the formalism of cosmological perturbations, the velocity is split in a background expansion plus a peculiar velocity:

$$\frac{dr}{dt} = \dot{r} = \frac{da}{dt}x + a\frac{dx}{dt} = \mathcal{H}r + a\boldsymbol{v}(t, x), \tag{2.65}$$

and the perturbed potential is:

$$\phi = \phi^{(0)}(t, x) + \delta\phi(t, x). \tag{2.66}$$

The Poisson equation establishes the relation between the gravitational potential and the matter density. In proper coordinates, this equation is:

$$\Delta_r \phi = 4\pi G\rho \tag{2.67}$$

in comoving coordinates it is

$$\Delta\rho = 4\pi G a^2 \rho \tag{2.68}$$

The Euler equations describe how the velocity field changes in time given a gravitational potential, in proper coordinates this is:

$$\frac{\partial}{\partial t}u + u \cdot \nabla_r u = -\nabla_r \phi. \tag{2.69}$$

In comoving coordinates, the Euler equation is:

$$\frac{du}{d\tau} = -\delta\phi \tag{2.70}$$

Using the the total velocity and the convective derivative:

$$\frac{d}{dt}\mathcal{H}\boldsymbol{x} + \frac{d}{dt}\boldsymbol{v} + \mathcal{H}\boldsymbol{v} + \boldsymbol{v} \cdot \nabla\boldsymbol{v} = -\delta\phi \tag{2.71}$$

For the background, the solution to the previous equation:

$$\frac{d}{dt}\mathcal{H} = -\frac{4}{3}\pi G a^2 \rho^{(0)} \tag{2.72}$$

The perturbated equation is on the other hand:

$$\frac{d}{dt}\boldsymbol{v} + \mathcal{H}\boldsymbol{v} + \boldsymbol{v}\cdot\nabla\boldsymbol{v} = -\nabla\delta\phi \tag{2.73}$$

so the perturbed Euler equation yields to scalar terms (the expansion and the shear) and a vectorial vectorial (the vorticity):

$$\frac{d}{dt}\boldsymbol{v} + \mathcal{H}\boldsymbol{v} + \frac{1}{2}\nabla\boldsymbol{v}^2 - \boldsymbol{v}\times\omega = -\nabla\delta\phi \tag{2.74}$$

where

$$\boldsymbol{v} \to \theta = \nabla\boldsymbol{v} \quad , \quad \sigma^i_j\partial\boldsymbol{v} - \delta^i_j\theta = \sigma\Sigma^i_j, \tag{2.75}$$

ω is defined as the vorticity

$$\omega \equiv \nabla\times\boldsymbol{v} \tag{2.76}$$

and the traceless tensor sigma is

$$\Sigma^i_j = \begin{pmatrix} 1 & 0 & 0 \\ 0 & 1 & 0 \\ 0 & 0 & -2 \end{pmatrix} \tag{2.77}$$

2.6 Standard Perturbation Theory

First of all we will analyze the standard perturbation theory where we consider pressureless dust particles and non-relativistic behavior so that relevant velocities are much smaller than the speed of light. For this formalism, the chosen coordinates are the ones where there is no comoving fluid, which are the Eulerian coordinates. The continuity equation in Eulerian coordinates is:

$$\frac{\partial\delta}{\partial\tau} + \nabla\cdot[(1+\delta)\boldsymbol{v}] = 0, \tag{2.78}$$

where $\boldsymbol{v}$ is the velocity and the dot the derivative with respect the conformal time τ. The Euler equation:

$$\frac{\partial \boldsymbol{v}}{\partial \tau} + (\boldsymbol{v} \cdot \nabla)\boldsymbol{v} = -\mathcal{H}\boldsymbol{v} - \nabla\phi \quad , \tag{2.79}$$

where ϕ is the gravitational potential field and the comoving Hubble factor as $\mathcal{H} \equiv d \ln a/d\tau = aH$. The Poisson equation:

$$\nabla^2\phi = 4\pi G a^2 \bar{\rho}\delta \quad , \tag{2.80}$$

Linear solutions for SPT

The linear solution can be used for when density and velocity perturbations are small, so coupled Fourier modes can be neglected, linear form of these equations are:

$$\frac{\partial \delta^{(1)}(\boldsymbol{k},\tau)}{\partial \tau} + \theta^{(1)}(\boldsymbol{k},\tau) = 0, \tag{2.81}$$

$$\frac{\partial \theta^{(1)}(\boldsymbol{k},\tau)}{\tau} + \mathcal{H}(\tau)\theta^{(1)}(\boldsymbol{k},\tau) + \frac{3}{2}\mathcal{H}^2(\tau)\Omega_m(\tau)\delta^{(1)}(\boldsymbol{k},\tau). \tag{2.82}$$

Where the superindex (1) is for the linear part of the expansion. We can solve for δ_1 substituting equation (2.81) into equation (2.82) to obtain:

$$\frac{\partial^2 \delta^{(1)}(\boldsymbol{k},\tau)}{\partial \tau^2} + \mathcal{H}(\tau)\frac{\partial \delta^{(1)}(\boldsymbol{k},\tau)}{\delta \tau} + \frac{3}{2}\mathcal{H}^2(\tau)\Omega_m(\tau)\delta_1(\boldsymbol{k},\tau) = 0 \quad , \tag{2.83}$$

this is a second order differential equation with solution:

$$\delta(\boldsymbol{k},\tau) = D_+\delta_0^+(\boldsymbol{k}) + D_-\delta_0^-(\boldsymbol{k}) \quad . \tag{2.84}$$

Normalizing the time factors to unity at the present time, the growth factors of both the growing (+) and decaying (-) modes, we find that the expansion (2.84), imposes the following definitions where solutions are:

$$D_+(\tau) = \frac{5}{2}\Omega_m \frac{H(a)}{H_0}\int_0^a \frac{da'}{[a'^3 H(a')/H_0]^3} \tag{2.85}$$

$$D_-(\tau) = \frac{H}{H_0} = \frac{1}{a}\frac{\mathcal{H}}{\mathcal{H}_0} \quad . \tag{2.86}$$

These functions have variations depending on the cosmology. With Eq. (2.84) we can have a solution for the continuity equation (2.81) as:

$$\theta(\boldsymbol{k}, \tau) = -\mathcal{H}(\tau)[f(\tau)\delta_0^+ + g(\tau)\delta_0^-] \tag{2.87}$$

where the growth rates denoted by:

$$f(\tau) = \frac{1}{\mathcal{H}(\tau)}\frac{d\ln D_+(\tau)}{d\tau} = \frac{d\ln D_+}{d\ln a} \quad , \quad g(\tau) = \frac{d\ln D_-}{d\ln a} \tag{2.88}$$

If we consider an Einstein-de Sitter cosmology (i.e. flat $K = 0$, only matter without cosmological constant $\Omega_m = 1, \Omega_\Lambda = 0$), that can describe the Universe after matter-radiation equality, we can solve the Friedmann equation, where the scale factor and the conformal expansion rate are:

$$a(\tau) = \left(\frac{H_0}{2}\tau\right)^2 \propto \tau^2 \quad , \tag{2.89}$$

$$\mathcal{H} = \mathcal{H}_0 a^{-1/2} = \frac{2}{\tau} \quad . \tag{2.90}$$

This yields the following solutions:

$$D_+(\tau) = a \ \ , \ \ D_- = a^{-3/2} \ \ , \ \ f_1(\tau) = 1' \ , \ \ g(\tau) = -\frac{3}{2} \quad . \tag{2.91}$$

The fact that the growing mode D_+ is equal to the scale factor a, allows us to compare the amplitude of the metric perturbations at recombination to the local density perturbations. For the case of the decaying mode D_-, disappears fast and becomes subdominant. This mode is usually neglected..

For ΛCDM cosmological model, that corresponds to a universe with cosmological constant Λ, so $\Omega_m \neq, \Omega_\Lambda \neq 0$, the growth function and the growth rate become:

$$D_+ \approx \frac{5}{2}\frac{a\Omega_{m,0}}{\Omega_{m,0}^{4/7} - \Omega_{\Lambda,0}} + (1 + \Omega_{m,0}/2)(1 + \Omega_{m,0}/70) \quad , \tag{2.92}$$

$$f(\tau) \approx [1 - (\Omega_{m,0} + \Omega_{\Lambda,0} - 1)a + \Omega_{\Lambda,0}a^3]^{-4/7} \tag{2.93}$$

Non-linear solution for SPT

For EdS, when decaying mode is neglected, the density contrast and velocity in linear approximations are:

$$\delta^1(\boldsymbol{k},\tau) = a(\tau)\delta_0(\boldsymbol{k}) \quad , \quad \theta^1(\boldsymbol{k},\tau) = -\mathcal{H}(\tau)a(\tau)\delta_0(\boldsymbol{k}) \quad . \tag{2.94}$$

where superindex 1 represents linear approximation. The pertubative expansion to higher orders is:

$$\delta(\boldsymbol{k},\tau) = \sum_{n=1}^{\infty} a^n(\tau)\delta_n(\boldsymbol{k}) \quad , \quad \theta(\boldsymbol{k},\tau) = -\mathcal{H}\sum_{n=1}^{\infty}(\tau)a^n(\tau)\delta_n(\boldsymbol{k}) \quad . \tag{2.95}$$

To obtain this solutions we have to expand the density and velocity k functions as:

$$\delta^n(\boldsymbol{k}) = \int \frac{d^3q_1}{(2\pi)^3} \cdots \int \frac{d^3q_n}{(2\pi)^3}\Big[\delta^1(\boldsymbol{q}_1,\tau),...,\delta^1(\boldsymbol{q}_n,\tau) \times F_n(\boldsymbol{q}_1,...,\tau)\boldsymbol{q}_n\delta_D(\boldsymbol{k}-\boldsymbol{q_1}-...-\boldsymbol{q_n})\Big] \quad , \tag{2.96}$$

$$\theta^n(\boldsymbol{k}) = \int \frac{d^3q_1}{(2\pi)^3} \cdots \int \frac{d^3q_n}{(2\pi)^3}\Big[\delta^1(\boldsymbol{q}_1,\tau),...,\delta^1(\boldsymbol{q}_n,\tau) \times G_n(\boldsymbol{q}_1,...,\tau)\boldsymbol{q}_n\delta_D(\boldsymbol{k}-\boldsymbol{q_1}-...-\boldsymbol{q_n})\Big] \quad , \tag{2.97}$$

where F_n and G_n are kernels for the characterization of the wave modes. These kernels are defined as:

$$\begin{aligned} F_n(\boldsymbol{q}_1,...,\boldsymbol{q}_n) = &\sum_{m=1}^{n-1}\frac{G_m(\boldsymbol{q}_1,...,\boldsymbol{q}_m)}{(2n+3)(n-1)}[(2n+1)\alpha(\boldsymbol{k}_1,\boldsymbol{k_2}) \\ &\times \ F_{n-m}(\boldsymbol{q}_{m+1},...,\boldsymbol{q}_n) + 2\beta(\boldsymbol{k}_1,\boldsymbol{k_2}) \\ &\times \ G_{n-m}(\boldsymbol{q}_{m+1},...,\boldsymbol{q}_n)] \quad , \end{aligned} \tag{2.98}$$

$$
\begin{aligned}
G_n(\boldsymbol{q}_1,...,\boldsymbol{q}_n) = & \sum_{m=1}^{n-1} \frac{G_m(\boldsymbol{q}_1,...,\boldsymbol{q}_m)}{(2n+3)(n-1)}[3\alpha(\boldsymbol{k}_1,\boldsymbol{k_2}))\\
& \times \ F_{n-m}(\boldsymbol{q}_{m+1},...,\boldsymbol{q}_n) + 2n\beta(\boldsymbol{k}_1,\boldsymbol{k_2})\\
& \times \ G_{n-m}(\boldsymbol{q}_{m+1},...,\boldsymbol{q}_n)] \quad ,
\end{aligned}
\tag{2.99}
$$

where $\boldsymbol{k}_1 \equiv \boldsymbol{q}_1 + ... + \boldsymbol{q}_m, \boldsymbol{k}_2 \equiv \boldsymbol{q}_{m+1} + ... + \boldsymbol{q}_n$ and $F_1 = G_1 \equiv 1$. The kernels $\alpha(\boldsymbol{k}_1, \boldsymbol{k_2})$ and $\beta(\boldsymbol{k}_1, \boldsymbol{k_2})$ are given by

$$
\alpha(\boldsymbol{k}_1,\boldsymbol{k_2}) \equiv \frac{(\boldsymbol{k}_1+\boldsymbol{k}_2)\cdot\boldsymbol{k}_1}{k_1^2} \quad , \tag{2.100}
$$

$$
\beta(\boldsymbol{k}_1,\boldsymbol{k_2}) \equiv \frac{(\boldsymbol{k}_1+\boldsymbol{k}_2)^2(\boldsymbol{k}_1\cdot\boldsymbol{k}_2)\boldsymbol{k}_1}{2k_1^2k_2^2} \quad , \tag{2.101}
$$

where n is the order desired for the kernel, and $k = |\boldsymbol{k}|$. For linear order $F_1 = 1$ and $G_1 = 1$. For second order, the kernels are:

$$
F_2(\boldsymbol{k}_1,\boldsymbol{k}_2) = \frac{5}{7} + \frac{2}{7}\frac{(\boldsymbol{k}_1\cdot\boldsymbol{k}_2)^2}{k_1^2k_2^2} + \frac{\boldsymbol{k}_1\cdot\boldsymbol{k}_2}{2}\left(\frac{1}{k_1^2}+\frac{1}{k_2^2}\right) \quad , \tag{2.102}
$$

$$
G_2(\boldsymbol{k}_1,\boldsymbol{k}_2) = \frac{3}{7} + \frac{4}{7}\frac{(\boldsymbol{k}_1\cdot\boldsymbol{k}_2)^2}{k_1^2k_2^2} + \frac{\boldsymbol{k}_1\cdot\boldsymbol{k}_2}{2}\left(\frac{1}{k_1^2}+\frac{1}{k_2^2}\right) \quad , \tag{2.103}
$$

For third order:

$$
\begin{aligned}
F_3(\boldsymbol{k}_1,\boldsymbol{k}_2,\boldsymbol{k}_3) = & \frac{2k^2}{54}\left[\frac{\boldsymbol{k}_1\cdot\boldsymbol{k}_{23}}{k_1^2k_{23}^2}G_2(\boldsymbol{k}_2,\boldsymbol{k}_3) + (2\ cyclic)\right]\\
& + \frac{7}{54}\boldsymbol{k}\cdot\left[\frac{\boldsymbol{k}_{12}}{k_{12}^2}G_2(\boldsymbol{k}_1,\boldsymbol{k}_2) + (2\ cyclic)\right]\\
& + \frac{7}{54}\boldsymbol{k}\cdot\left[\frac{\boldsymbol{k}_1}{k_1^2}F_2(\boldsymbol{k}_2,\boldsymbol{k}_3) + (2\ cyclic)\right]
\end{aligned}
\tag{2.104}
$$

$$
\begin{aligned}
G_3(\boldsymbol{k}_1,\boldsymbol{k}_2,\boldsymbol{k}_3) = & \frac{k^2}{9}\left[\frac{\boldsymbol{k}_1\cdot\boldsymbol{k}_{23}}{k_1^2k_{23}^2}G_2(\boldsymbol{k}_2,\boldsymbol{k}_3) + (2\ cyclic)\right]\\
& + \frac{1}{18}\boldsymbol{k}\cdot\left[\frac{\boldsymbol{k}_{12}}{k_{12}^2}G_2(\boldsymbol{k}_1,\boldsymbol{k}_2) + (2\ cyclic)\right]\\
& + \frac{1}{18}\boldsymbol{k}\cdot\left[\frac{\boldsymbol{k}_1}{k_1^2}F_2(\boldsymbol{k}_2,\boldsymbol{k}_3) + (2\ cyclic)\right]
\end{aligned}
\tag{2.105}
$$

For non-linear solutions other than EdS cosmologies, the treatment is more complicated since solutions at higher orders are functions with conformal time and the momentum k dependence is not separable, so it can not be integrated in conventional ways. This implies that growing modes at n-th order are not proportional to the scale factor. Also there are not necessarily kernels with recursive behavior, but the dependence of the cosmological ingredients Ω_m and Ω_Λ is so weak that we can use a recursion relation similar to that of EdS in order to approximate the ΛCDM cases.

Lagrangian dynamics

In a Lagrangian scheme we are describing the density and velocity vector fields in a comoving displacement coordinate q. Where the displacement field $\Psi(\boldsymbol{q}, t)$ is defined as:

$$\boldsymbol{x}(\boldsymbol{q}, t) = \boldsymbol{q} + \Psi(\boldsymbol{q}, t) \quad . \tag{2.106}$$

The equations of motion for a trajectory $\boldsymbol{x}(t)$ is then:

$$\frac{d^2\boldsymbol{x}}{dt^2} + \mathcal{H}(t)\frac{d\boldsymbol{x}}{dt} = -\nabla_{\boldsymbol{x}}\Phi \quad . \tag{2.107}$$

Taking the divergence of this equation we obtain:

$$\nabla_{\boldsymbol{x}} \cdot \left[\frac{d^2\boldsymbol{x}}{dt^2} + \mathcal{H}(t)\frac{d\boldsymbol{x}}{dt}\right] = -\nabla^2_{\boldsymbol{x}}\Phi = -\frac{3}{2}\mathcal{H}^2\Omega_m\delta(\boldsymbol{x}) \quad , \tag{2.108}$$

where the density contrast is defined as:

$$\delta(\boldsymbol{x}) \equiv \frac{\rho(\boldsymbol{x})}{\bar{\rho}} - 1 \quad . \tag{2.109}$$

Via the mass conservation, we have:

$$\bar{\rho}d^3q = \rho(\boldsymbol{x}, \tau)d^3x = \bar{\rho}(\tau)[1 + \delta(\boldsymbol{x}, \tau)]d^3x \quad . \tag{2.110}$$

We can relate the density contrast in the Eulerian scheme with the displacement on the Lagrangian formalism as:

$$1 + \delta(\boldsymbol{x}, \tau) = \left| \frac{d^3\boldsymbol{q}}{d^3x} \right| = \frac{1}{J(\boldsymbol{q}, \tau)} \quad , \tag{2.111}$$

where the Jacobian is defined from Eq. (2.106) as $J(\boldsymbol{q}, \tau) = \mathrm{Det}(\delta_{ij} + \psi_{ij}(\boldsymbol{q}, \tau))$ and transforms Lagrangian o Eulerian coordinates. And the partial derivative of the displacement field as $\psi_{i,j} \equiv \partial\psi_i/\partial q_j$. If we use the SPT to Lagrangian relationship (2.111) in the equation of motion (2.108) we obtain:

$$J(\boldsymbol{q}, (\tau))\nabla_{\boldsymbol{x}} \cdot \left[\frac{d^2\boldsymbol{x}}{dt^2} + \mathcal{H}(t)\frac{d\boldsymbol{x}}{dt} \right] = \frac{3}{2}\mathcal{H}^2(\tau)\Omega_m(\tau)(J-1) \quad . \tag{2.112}$$

Using the chain rule we obtain the equation for the displacement field:

$$\begin{aligned} J(\boldsymbol{q}, \tau) \left[\frac{d^2\Psi_{i,j}(\boldsymbol{q}, \tau)}{d\tau^2} + \mathcal{H}(\tau)\frac{d\Psi_{i,j}(\boldsymbol{q}, \tau)}{dt} \right] = \\ \frac{3}{2}\frac{\mathcal{H}^2(\tau)\Omega_m(\tau)[J(\boldsymbol{q}, \tau) - 1]}{\delta_{ij} + \Psi_{i,j}}. \end{aligned} \tag{2.113}$$

Lagrangian Perturbation Theory (LPT)

We can solve the equation (2.113) with a perturbative treatment, so we make the expression for the displacement field as:

$$\Psi(\boldsymbol{q}, \tau) = \Psi^{(1)}(\boldsymbol{q}, \tau) + \Psi^{(1)}(\boldsymbol{q}, \tau) + ... \quad . \tag{2.114}$$

Where we can determine the order of the solution depending on the approximation we need.

Linear order LPT

To find the linear equation for the displacement field Ψ we need to approximate the Jacobian as:

$$J(\boldsymbol{q}, \tau) = \mathrm{Det}\left[\delta_{ij} + \Psi_{i,j}(\boldsymbol{q}, \tau)\right] \approx 1 + \Psi_{i,i}(\boldsymbol{q}, \tau) \quad , \tag{2.115}$$

also the inverse of the Jacobian matrix:

$$[\delta_{ij} + \Psi_{i,j}]^{-1} \approx \delta_{ij} - \Psi_{i,j} \quad . \tag{2.116}$$

With this approximations, the equation (2.113) of the displacement field Ψ in the linear approximation of the Jacobian becomes:

$$(1 + \Psi_{k,k})[\delta_{ij} - \Psi_{i,j}] \left(\frac{d^2\Psi_{i,j}}{d\tau^2} + \mathcal{H}(\tau) \frac{d\Psi_{i,j}}{d\tau} \right) = \frac{3}{2} \mathcal{H}^2(\tau) \omega_m(\tau) \Psi_{k,k} \quad , \tag{2.117}$$

where the equation at linear order for $\Psi^{(1)}$ is reduced to:

$$\frac{d^2\Psi^{(1)}_{i,i}}{d\tau^2} + \mathcal{H}(\tau) \frac{d\Psi^{(1)}_{i,i}}{d\tau} = \frac{3}{2} \mathcal{H}^2(\tau) \omega_m(\tau) \Psi_{i,i} \quad . \tag{2.118}$$

Given the relation to the matter density contrast in Eq. (2.111) and the governing equation for δ in Eq. (2.83) we can conclude that:

$$\nabla_q \cdot \Psi^{(1)} = -\delta_1(\boldsymbol{x}, \tau) \quad , \tag{2.119}$$

and just as before, the equation for the growth function is:

$$D_1^{''}(\tau) + \mathcal{H}(\tau) D_1''(\tau) = \frac{3}{2} \mathcal{H}^2(\tau) \Omega_m(\tau) D_1(\tau) \tag{2.120}$$

In terms of Eulerian coordinates, the position of the particle is thus:

$$\boldsymbol{x} = \boldsymbol{q} - \nabla_q^{-1} \delta_q(\boldsymbol{x}\tau) \tag{2.121}$$

and the peculiar velocity is just the time derivative. In Lagrangian coordinates, where the position $\mathbf{q}$ is fixed,

$$\boldsymbol{v} \equiv \frac{d\boldsymbol{x}}{d\tau} = -\mathcal{H} f_1 \nabla_q^{-1} \delta_q(\boldsymbol{x}, \tau) \quad , \tag{2.122}$$

here f_1 is the logarithmic derivative of the linear growth factor defined as:

$$f_1 \equiv \frac{d \ln D_1}{d \ln a}. \tag{2.123}$$

The curl-free condition of the Lagrangian displacement, implies the existence of a scalar potential. At linear order:

$$\Psi^{(1)}(\boldsymbol{q},\tau) = -\nabla_q \phi^{(1)}(\boldsymbol{q},\tau) \quad , \tag{2.124}$$

where ϕ is the linear Lagrangian potential related to the density field:

$$\nabla_q \cdot \Psi^{(1)}(\boldsymbol{q},\tau) = -\nabla_q^2 \phi^{(1)}(\boldsymbol{q},\tau) = -\delta(\boldsymbol{x},\tau) \quad . \tag{2.125}$$

so the solutions for the position and peculiar velocity in terms of the Lagrangian potential ϕ are:

$$\boldsymbol{x}(\boldsymbol{q},\tau) = \boldsymbol{q} - \nabla_q \phi^{(1)}(\boldsymbol{q},\tau) \tag{2.126}$$

$$\boldsymbol{v}(\boldsymbol{q},\tau) = -\mathcal{H}_q \phi^{(1)}(\boldsymbol{q},\tau) \quad . \tag{2.127}$$

Zel'dovich approximation

When matter behavior starts to deviate from linear approximation such to when the perturbations grow similar as the background density, the interactions are stronger. If we assume non-rotational perturbation, using a linear potential, we have a diagonalized Jacobian Matrix such as:

$$J(\boldsymbol{q},\tau) = \begin{vmatrix} 1-\lambda_1 D_1(\tau) & 0 & 0 \\ 0 & 1-\lambda_2 D_1(\tau) & 0 \\ 0 & 0 & 1-\lambda_3 D_1(\tau) \end{vmatrix} \tag{2.128}$$

where λ_i are the eigenvalues, here conveniently sorted as $\lambda_1 \geq \lambda_2 \geq \lambda_3$. Without loss of generality, this describes the geometry of the fluid as indicator of collapse or expansion. If $\lambda_i > 0$ the fluid is contracting, if $\lambda_i < 0$, it is expanding in the same direction. We describe the density contrast as:

$$1 + \delta(\boldsymbol{x},\tau) = \frac{1}{[1-\lambda_1 D_1(\tau)][1-\lambda_2 D_1(\tau)][1-\lambda_3 D_1(\tau)]} \quad . \tag{2.129}$$

The Zel'dovich approximation is typically used to set the initial conditions of cosmological simulations where non-linearity from evolution is not relevant yet.

Second order LPT (2LPT)

Using the expansion of the density field of (2.114), at second order, we obtain the Jacobian until the second order:

$$J \approx 1 + \Psi^{(2)}_{k,k} + \frac{1}{2}\left[\left(\Psi^{(1)}_{k,k}\right) - \Psi^{(1)}_{j,i}\Psi^{(1)}_{j,i}\right] \quad . \tag{2.130}$$

The equation of motion given the Jacobian at second order is:

$$\left(\frac{d^2\Psi^{(2)}_{i,i}}{d\tau^2} + \mathcal{H}\frac{d\Psi^{(2)}_{i,i}}{d\tau}\right) + \Psi^{(1)}_{k,k}\left(\frac{d^2\Psi^{(1)}_{i,i}}{d\tau^2} + \mathcal{H}\frac{d\Psi^{(1)}_{i,i}}{d\tau}\right) - \Psi^{(1)}_{k,k}\left(\frac{d^2\Psi^{(1)}_{i,i}}{d\tau^2} + \mathcal{H}\frac{d\Psi^{(1)}_{i,j}}{d\tau}\right)$$
$$= \frac{3}{2}\mathcal{H}^2\Omega_m\left[\Psi^{(2)}_{k,k} + \frac{1}{2}\left(\Psi^{(2)}_{k,k} - \frac{1}{2}\Psi^{(1)}_{i,j}\Psi^{(1)}_{j,i}\right)^2\right] \quad . \tag{2.131}$$

The solution for the linear displacement (2.118) is used to obtain the equation of motion as:

$$\left(\frac{d^2\Psi^{(2)}_{i,i}}{d\tau^2} + \mathcal{H}\frac{d\Psi^{(2)}_{i,i}}{d\tau} - \frac{3}{2}\mathcal{H}^2\Omega_m\Psi^{(2)}_{i,i}\right) = \frac{3}{2}\mathcal{H}^2\Omega_m\left[\frac{1}{2}\left(\Psi^{(2)}_{k,k} - \frac{1}{2}\Psi^{(1)}_{i,j}\Psi^{(1)}_{j,i}\right)^2\right] \quad . \tag{2.132}$$

Consequently, the growth function at second order is:

$$D_2''(\tau) + \mathcal{H}D_2'(\tau) - \frac{3}{2}\mathbf{H}^2\Omega_m D_2(\tau) = -\frac{3}{2}\mathcal{H}^2\Omega_m[D_1(\tau)]^2 \quad . \tag{2.133}$$

Similar to the linear approximation, we can introduce a second order scalar potential as:

$$\Psi^{(2)}(\boldsymbol{q},\tau) = \nabla_q\phi^{(2)}(\boldsymbol{q},\tau) \tag{2.134}$$

The position and velocity at second order are described by:

$$\boldsymbol{x}(\boldsymbol{q},\tau) = \boldsymbol{q} - \nabla_q \phi^{(1)}(\boldsymbol{q},\tau) + \nabla_q \phi^{(2)}(\boldsymbol{q},\tau) \tag{2.135}$$

$$\boldsymbol{v}(\boldsymbol{q},\tau) = \frac{d\boldsymbol{x}}{d\tau} = \mathcal{H} f_1 \nabla_q \phi^{(1)}(\boldsymbol{q},\tau) + \mathcal{H} f_1 \nabla_q \phi^{(2)}(\boldsymbol{q},\tau) \tag{2.136}$$

2.7 Relativistic perturbations

3+1 formalism

In GR, four-dimensional spacetime can be sliced into hypersurfaces with 3 space coordinates and 1 time coordinate. Two of the useful approaches are the 1+3 formalisms. The differences are subtle but important for manipulation and interpretation of the equations. In general, in 3+1 formalism space-time is foiled through a given family of hypersurfaces. In the 1+3 formalism the spacetime is threaded using a family of time-integrals that can connect the points representing positions in different hypersurfaces. In cosmology, it is usual to pick a preferred direction of motion of the objects in the Universe: the preferential 4-velocity (comoving observers) that is congruent with the geodesics that thread space-time.

With the established coordinate split it is convenient to define local comoving coordinates $x^\mu = (t, y^i)$ choosing a surface S that intersects each world line only once at points labelled as $y^i, i = 1, 2, 3$. The preferential motion along the flux lines allow us to define the comoving coordinates and implies the existence of a preferential 4-velocity defined by the local coordinates $x^\mu = x^\mu(\tau)$ where τ is the proper time along the world lines. So the 4 velocity is defined as:

$$u^\mu = \frac{dx^\mu}{d\tau}, \quad \text{with} \quad u^\mu u_\mu = -1 \ . \tag{2.137}$$

The normalization thus defines the comoving coordinates as those with

a fixed position, and a normalized proper time s such that:

$$u^{\mu} = \delta^{\mu}_{0} \longrightarrow \frac{ds}{d\tau} = 1 \quad , \quad \frac{dy^{i}}{d\tau} = 0 \quad , \tag{2.138}$$

where s is the normalized proper time.

We can define a projector tensor (h_{ab}) which defines the components orthogonal to u^{a} for general tensors in spacetime of the spatial orthogonal hypersurfaces to a^{a}. This tensor acts as spatial metric to this hypersurfaces

$$h_{ab} = g_{ab} + u_{a}u_{b} \quad . \tag{2.139}$$

This tensor satisfies the relations $h^{a}_{b}h^{b}_{c}h^{c}_{a} = 3$ and $h^{a}_{b}u^{b} = 0$. In this way, any vector V_{a} and tensors S_{ab}, we can obtain the Projected Symmetric Tracefree part (PSTF) by:

$$V_{<a>} = h^{b}_{a}V_{b} \quad , \quad S_{<ab>} = \left\{ h^{c}_{(a}h^{d}_{b)} - \frac{1}{3}h_{ab}h^{cd} \right\} S_{cd} \quad . \tag{2.140}$$

With the 4-velocity and the projection tensor we can define the time derivative through the flux lines and the projected derivative to the orthogonal hypersurfaces. The time derivative for an arbitrary tensor $S^{a_{1}\ldots a_{k}}_{b_{a}\ldots b_{l}}$ is:

$$\dot{S}^{a_{1}\ldots a_{k}}_{b_{a}\ldots b_{l}} = u^{c}\nabla_{c}S^{a_{1}\ldots a_{k}}_{b_{a}\ldots b_{l}} \quad , \tag{2.141}$$

and thus we can define the acceleration vector as

$$\dot{u}^{a} = u^{b}\nabla_{b}u^{a} \longrightarrow \dot{u}^{a}u_{a} = 0 \quad . \tag{2.142}$$

The projected derivative (which is the covariant derivative to the orthogonal hypersurfaces to u^{a}) is defined by:

$$\bar{\nabla}_{c}S^{a_{1}\ldots a_{k}}_{b_{1}\ldots b_{l}} = h^{f}_{c}h^{a1}_{d1}\ldots h^{a_{k}}_{d_{k}}h^{b_{k}}_{e_{k}}\ldots h^{b_{l}}_{e_{l}}\nabla_{f}S^{d1\ldots dk}_{e1\ldots e_{l}} \quad , \tag{2.143}$$

with this definition we can split the covariant derivative of u^{a} as:

$$\nabla_{b}u_{a} = \bar{\nabla}_{b}u_{a} - \dot{u}_{a}u_{b} \quad . \tag{2.144}$$

For a spatial surface S where $t = const.$, we can define a relative position vector to the comoving coordinates $x^\mu(t, y^i)$ as follows:

$$\beta^\mu = \left(\frac{\partial x^\mu}{\partial y^i}\right)_{t=cnt.} \delta y^i \quad , \tag{2.145}$$

this vector is not orthogonal no the flux lines, so is projected to have a relative position vector to u^a

$$\beta^{<a>} = e^a \delta l \ , \quad e^a u_a = 0 \ \ \& \ \ \beta^{<a>}\beta_{<a>} = \delta l^2 \quad , \tag{2.146}$$

where e^a is an orthogonal unitary vector to u^a and the relative distance δl. The time derivative of this vector yields the relative velocity between point in that hypersurface

$$v^a = v_{<a>} = h^a_b u^d \nabla_d (h^b_c \beta^c) = \dot{\beta}^{<a>} \quad . \tag{2.147}$$

This vector satisfies the fact that the Lie derivative along u^a is null $\pounds_u v^a = 0$, so the relative velocity between particles, is given by the linear transformation from the relative position $v^a = V^b_a \beta^{<b>}$ where $V^b_a = \bar{\nabla}_b u_a$ and

$$V_{ab} = \bar{\nabla}_b u_a = V_{(ab)} + V_{[ab]} = \Theta_{ab} + \omega_{ab} = \sigma_{ab} + \frac{1}{3}\Theta h_{ab} + \omega_{ab} \quad , \tag{2.148}$$

where Θ_{ab} is the expansion tensor, ω_{ab} is the vorticity tensor, σ_{ab} the shear tensor and Θ the scalar related to the expansion. With these quantities it is possible to define a generalized Hubble relation as:

$$\frac{\dot{\delta l}}{\delta l} = \Theta_{ab} e^a e^b = \frac{1}{3}\Theta + \sigma_{ab} e^a e^b \quad , \tag{2.149}$$

The Hubble scalar can be defined as the proportional to the volume expansion Θ as:

$$H = \frac{\dot{l}}{l} = \frac{1}{3}\Theta \quad . \tag{2.150}$$

The covariant derivative in terms of the kinematic variables is the sum of the projected derivative (2.148) plus the derivative along the velocity vector u^a, thus:

$$\nabla_b u_a = \omega_{ab} + \sigma_{ab} + \frac{1}{3}\Theta h_{ab} - \dot{u}_a u_b \quad . \tag{2.151}$$

These quantities are observables which are in principle realized in galaxy surveys.

2.8 Perturbative Initial Conditions

2.8.1 Evolution equations

In the last section we defined the relativistic covariant quantities that describe the evolution of elements in a general spacetime, within the 1+3 formalism. We shall follow such definitions to derive non-linear quantities in cosmological perturbation theory, which will thus constitute the synchronous-comoving gauge. Often is chosen for evolution equations for the density contrast to represent a suitable Lagrangian frame in GR and to define a local Lagrangian galaxy bias up to second order [29]. Taking only scalar degrees of freedom on account of the line element is

$$ds^2 = a^2(\eta)[-(1+2\phi)d\eta^2 + 2\omega_{,i}d\eta dx^i + \gamma_{ij}dx^i dx^j] \quad , \tag{2.152}$$

where a is the scale factor, η is the conformal time. ϕ and ω are scalar metric perturbations and γ_{ij} is the spatial metric, with latin indices accounting for the three spatial coordinates. Working in the synchronous-comoving gauge, we set $\phi = \omega_{,i} = 0$. This is useful to evolve, as a matter content, a pressureless fluid as described by comoving observers. This defines the four-velocity as $u_\mu = (-a, 0, 0, 0)$ (with greek indices running from 0 to 3 and representing spacetime coordinates). With the

above elements at hand, we define the deformation tensor is [30],

$$\vartheta^{\mu}{}_{\nu} \equiv a u^{\mu}{}_{;\nu} - \mathcal{H}\delta^{\mu}{}_{\nu} \quad . \tag{2.153}$$

This tensor presents only non-trivial spatial components proportional to the extrinsic curvature K^i_j of the conformal spatial metric γ_{ij}

$$\vartheta^i_j = -K^i_j \quad , \tag{2.154}$$

where the extrinsic curvature is given by

$$K^i_j \equiv -\frac{1}{2}\gamma^{ik}\gamma'_{kj} \quad , \tag{2.155}$$

(where a prime stands for $' \equiv \partial/\partial\eta$).

The above is the basis for the covariant fluid approach to perturbation theory [31], [32]. The density field ρ can be split in a density background $\bar{\rho}(\eta)$ and a fluctuation $\delta\rho(x,\eta)$ is

$$\rho(x,\eta) = \bar{\rho}(\eta) + \delta\rho(x,\eta) = \bar{\rho}(\eta)(1+\delta(x,\eta)) \quad . \tag{2.156}$$

The continuity equation for the evolution of the density contrast $\delta(\mathbf{x},\eta)$ is

$$\delta' + (1+\delta)\vartheta = 0 \quad , \tag{2.157}$$

where $\vartheta = \vartheta_{\alpha}{}^{\alpha}$ is the trace of $\vartheta_{\nu}{}^{\mu}$. The evolution of ϑ is described by the Raychaudhuri equation which is

$$\vartheta' + \mathcal{H}\vartheta + \vartheta^i{}_j\vartheta^j{}_i + 4\pi G a^2\bar{\rho}\delta = 0 \quad . \tag{2.158}$$

The Raychaudhuri equation is analog to Euler's equation, but in this case in the GR regime which describes the motion of particles [30]. Equations (2.157) and (2.158) describe the evolution of a dust component in a cosmological de-Sitter or ΛCDM background. Note that these two equations find a non-linear equivalence with the Newtonian continuity and Euler

equations in the Lagrangian frame, when the following equivalences are drawn (see e.g. [33]):

$$\textit{Newtonian Lagrangian} \longleftrightarrow \textit{Relativistic comoving}$$

$$\frac{d}{dt} \longleftrightarrow \frac{\partial}{\partial \eta}$$

$$\partial^i v_j \longleftrightarrow \vartheta^i_j$$

$$\delta_N \longleftrightarrow \delta$$

After the consideration of a geometrical equivalence between the deformation tensor and the Ricci curvature, the 00-component of the Einstein field equation, the energy constraint, can be written as [31]

$$\vartheta^2 - \vartheta^i{}_j \vartheta^j{}_i + 4\mathcal{H}\vartheta + {}^3R = 16\pi G a^2 \bar{\rho}\delta \quad , \tag{2.159}$$

A similar equation can be derived from the Newtonian conservation of energy equation with the total energy given by $E_N = 1/2v^2 - \phi_N$. In that case, one can show that, at first order, the pertrurbative part of the Newtonian (conserved) energy is equal to the spatial curvature ${}^3R^{(1)} = -4\nabla^2\delta E_N^{(1)}$.

At non-linear order the correspondence with the Newtonian energy conservation is broken but the Ricci three-curvature is still time-independent as shown in [34] and can be expanded in terms of the (non-linear) metric potentials encoded in γ_{ij} as we shall show below.

At large scales, the differences between the Newtonian and relativistic descriptions of the non-linear inhomogeneities lie within the constraint equation, and are dominated by the spatial curvature term. This is justified in the following through a gradient expansion. In particular, we show that the curvature terms are dominant at early times in the relativistic constraint (2.159). As we shall see, such contributions also include the primordial non-Gaussianity, if present.

2.8.2 Perturbative and gradient expansion of the relativistic contribution

Restoring to a perturbative expansion, the scalar quantities can be written such:

$$\delta = \delta^{(1)} + \frac{1}{2}\delta^{(2)} + \frac{1}{6}\delta^{(3)} + \dots \tag{2.160}$$

where the superscript in parenthesis indicates the perturbative expansion order.

For the linear order, the solution for the density contrast is

$$\delta^{(1)} = \frac{D_+(\eta)}{10\mathcal{H}_{IN}D_{+IN}}(-4\nabla^2\zeta^{(1)}) \ , \tag{2.161}$$

where the growth factor in Einstein-de Sitter Universe is [35]

$$D_+ = \frac{D_{+IN}\mathcal{H}_{IN}^2}{\mathcal{H}^2} \ , \tag{2.162}$$

and where the subindex IN represents values at an arbitrary initial time in the matter-dominated universe. This is in complete equivalence with the Newtonian standard perturbation theory case, if we identify the curvature perturbation ζ and $-\phi_N$.

The curvature perturbation ζ is one of two scalar degrees of freedom that are encoded in the spatial metric, this perturbation is considered to have nearly Gaussian distribution from the slow-roll inflation model. The other scalar of the metric in this gauge is χ. Which is the traceless part of γ, and thus it has no equivalence with the longitudinal functions of the Newtonian theory. Considering the synchronous-comoving gauge, the expansion for γ_{ij} is

$$\begin{aligned}\gamma_{ij} =& \exp[2\zeta]\delta_{ij} + \left(\partial_i\partial_j - \frac{1}{3}\nabla^2\right)\chi \\ =& \left[1 + \zeta^{(1)} + 2\zeta^{(1)2} + \zeta^{(2)} + (\partial_i\partial_j - \frac{1}{3}\nabla^2)\left(\chi^{(2)} + \frac{1}{2}\chi^{(2)}\right)\right] + \dots\end{aligned} \tag{2.163}$$

note that χ encodes the traceless perturbation of the spatial metric through derivatives. This makes χ a subdominant variable in a gradient expansion. The large scales contributions are thus dominated by the conformal perturbation ζ, which besides corresponds to the curvature perturbation in the uniform density gauge [36], then it can be written as

$$g_{ij} = a^2\gamma_{ij} = a^2 e^{2\zeta}\bar{\gamma}_{ij}, \tag{2.164}$$

where $\bar{\gamma_{ij}}$ is the conformal part of the spatial metric. This explicitly shows that ζ is responsible for all inhomogeneous part of the isotropic expansion. The above can be used to set initial conditions in the early Universe after inflation. In such scenario, the curvature perturbation ζ is nearly scale-invariant and remains constant for modes outside the cosmological horizon. Then, in order to capture the contribution of relativistic terms, we perform a gradient expansion (long-wavelength approximation), where the spatial gradients are small compared to time derivatives. We thus note that the following perturbed quantities are of second order:

$$\delta \sim \vartheta \sim {}^3R \sim \mathcal{O}\left[\nabla^2\right] \quad . \tag{2.165}$$

If we stick to the large-scales in a gradient expansion in powers of $\nabla/\mathcal{H}$, which is the regime where the relativistic corrections are expected to be significant, then it can be shown that the dominant contribution to the three-curvature, the relativistic counterpart of the gravitational energy, comes from the conformal metric potential ζ. Given the conformal transformation $g_{ij} = a^2 e^{2\zeta}\bar{\gamma}_{ij}$ where the conformal factor is $e^{2\zeta}$ the spatial curvature is then:

$${}^3R = e^{-2\zeta}\left[-4\nabla^2\zeta - 2(\nabla\zeta)^2\right] \quad , \tag{2.166}$$

Consequently we can safely adopt the approximation $\bar{\gamma}_{ij} \simeq \delta_{ij}$ which leaves out the traceless parts of the curvature. Thus the spatial curvature

takes the form

$$ {}^3R = -4\nabla^2\zeta + \sum_{m=0}^{\infty} \frac{(-2)^{m+1}}{(m+1)!}[(m+a)(\nabla\zeta)^2 - 4\zeta\nabla^2\zeta]\zeta^m, \qquad (2.167) $$

valid at large scales and at non-linear order [34], [37].

With the equation (2.222), one can obtain solutions for the density contrast at higher orders. Even for $m = 1$ in equation (2.167) one can find third order corrections as follows

$$ {}^3R = -4\nabla^2\zeta + (-2)[(\nabla\zeta)^2 - 4\zeta\nabla^2\zeta] + 2[2(\nabla\zeta)^2 - 4\zeta\nabla^2\zeta]\zeta \quad . \ (2.168) $$

The Ricci scalar at large scales (at second order in a gradient expansion) and considering scalars only in light of non-Gaussian initial fields, is given in terms of the first order perturbation field factors as

$$ \begin{aligned} {}^3R \simeq -4\nabla^2\zeta^{(1)} &+ \left(\nabla\zeta^{(1)}\right)^2 \left[-2 - \frac{24}{5}f_{\rm NL}\right] + \zeta^{(1)}\nabla^2\zeta^{(1)} \left[-\frac{24}{5}f_{\rm NL} + 8\right] \\ &+\zeta^{(1)} \left(\nabla\zeta^{(1)}\right)^2 \left[-\frac{216}{25}g_{\rm NL} + \frac{24}{5}f_{\rm NL} + 4\right] \\ &+\zeta^{(1)2}\nabla^2\zeta^{(1)} \left[-\frac{108}{25}g_{\rm NL} + \frac{72}{5}f_{\rm NL} - 8\right] + O(\zeta^{(1)4}) \quad . \end{aligned} \qquad (2.169) $$

This expression sums up the justification for the present work: The three-curvature ${}^3R$ encodes the differences, at the level of constraints, between the Newtonian and the Relativistic formalisms of structure formation, since the evolution equations (2.157) and (2.158) for a cold dark matter component are identical at non-linear level between these two formalisms (at large scales, where the gradient expansion remains valid). This means that Relativistic initial conditions included in ${}^3R$ can be evolved employing a Newtonian hydrodynamical code, or its equivalents, and the results remain consistent with GR. Moreover, we notice that even

in the case that initial conditions limited to relatively large scales, i.e., at lowest order in the gradient expansion $\nabla/\mathcal{H}$, we can still express the relativistic contributions in terms of ζ, and also allow for a non-linear primordial ζ, that is, to include primordial non-Gaussianities.

These considerations argue that the formalism presented can be implemented in hydrodynamic codes (e.g. [38] or [39]) or codes which show equivalence with the hydrodynamical description at large scales, such as L-PICOLA [7], which we discuss in more detail in the following Sec. 3.1. This allows for the evolution of initial conditions which include relativistic constraints through Newtonian equations[1].

As conclusion this section, we explicitly present the matter density field up to third order in perturbation theory which will be specifically employed in setting initial conditions for numerical simulations. This represents the homogeneous part of the solution to the constraint (2.159) (valid at second order in a gradient expansion) [37], [42].

$$\frac{1}{2}\delta^{(2)} = \frac{D_+(\eta)}{10\mathcal{H}^2 D_{+IN}}\frac{24}{5}\left[-(\nabla\zeta^{(1)})^2\left(\frac{5}{12}+f_{\rm NL}\right)+\zeta^{(1)}\nabla^2\zeta^{(1)}\left(\frac{5}{3}-f_{\rm NL}\right)\right] \quad , \tag{2.170}$$

$$\frac{1}{6}\delta^{(3)} = \frac{D_+(\eta)}{10\mathcal{H}_{IN}^2 D_{+IN}}\frac{108}{25}\Bigg[2\zeta^{(1)}(\nabla\zeta^{(1)})^2\left(-g_{\rm NL}+\frac{5}{9}f_{\rm NL}+\frac{25}{54}\right) + \zeta^{(1)2}\nabla^2\zeta^{(1)}\left(-g_{\rm NL}+\frac{10}{3}f_{\rm NL}-\frac{50}{27}\right)\Bigg] \quad . \tag{2.171}$$

Afetrwards in the section 3.2 we implement these solutions as initial conditions for a numerical simulation in order to compute the polyspectra of the evolved density field for cases of interest. We also employ these last two expressions to complement the usual (Newtonian) one-loop contributions to the power spectrum as detailed in Ref. [42], and implement

[1]Expressions for the Lagrangian displacement with relativistic input have been discussed in previous works, [40], [41]. These can be regarded as strategies to modify the initial conditions generating code to support directly the grid-based setup.

them as discussed in Sec. 3.2.1.

2.9 Statistical description of matter

2.9.1 2-point correlation function

From inflation theory and observations, it is determined that the primordial perturbations have a nearly Gaussian distribution and the same stands for the density field. The 2PCF is defined as the excess of probability of finding an object given a Gaussian distribution. Considering $n = 2$, we have the two point correlation function as:

$$\zeta_{2pcf}(\boldsymbol{x}_1, \boldsymbol{x}_2) =< \delta_1(\boldsymbol{x}_1)\delta_1(\boldsymbol{x}_2) >= \frac{1}{C(\boldsymbol{x}_1, \boldsymbol{x}_2)}, \tag{2.172}$$

with the help of Wick's theorem one can calculate the average of a product of an even number of δ_1, which is the sum over all the possible parings of δ_1 with each other:

$$< \delta_1(\boldsymbol{x_1})\delta_1(\boldsymbol{x_2})... >= \sum_{pairings} \prod_{pairs} < \delta_1\delta_1 > \quad . \tag{2.173}$$

Considering the Gaussian case, all high order (n>2) correlation functions are thus products of the two point correlation function if n is even, and vanish is n is odd. From equation (2.172), the covariance matrix is related to the correlation function as:

$$\int d^3z \zeta_{2pcf}(\boldsymbol{x}, \boldsymbol{z}) C^{-1}(\boldsymbol{z}, \boldsymbol{y}) = \delta^3(\boldsymbol{x} - \boldsymbol{y}) \quad . \tag{2.174}$$

At large scales, the Universe behaves statistically homogeneous and isotropic, so $\zeta(\boldsymbol{x}, \boldsymbol{z})$ and $C(\boldsymbol{x}, \boldsymbol{z})$ depend only on the coordinates separation:

$$\int d^3z \zeta_{2pcf}(\boldsymbol{x} - \boldsymbol{z}) C^{-1}(\boldsymbol{z} - \boldsymbol{y}) = \delta^3(\boldsymbol{x} - \boldsymbol{y}) \quad , \tag{2.175}$$

in Fourier space, this equation is:

$$C(\boldsymbol{q}) = \frac{1}{P_L(q)} \quad , \tag{2.176}$$

where $P_L(q)$ is the linear power spectrum, which is related to the two point correlation function (2PCF) via the Fourier transform

$$\zeta(r) = \int \frac{d^3q}{(2\pi)^3} P_L(q) e^{i\boldsymbol{q}\cdot\boldsymbol{r}} \quad . \tag{2.177}$$

2.9.2 One-loop approximation

We describe the perturbations in the Lagrangian Perturbation Theory and in real space displacement as

$$\delta(\boldsymbol{x}) = \int d^3q \delta^3[\boldsymbol{x} - \boldsymbol{q} - \Psi(\boldsymbol{q})] - 1 \quad , \tag{2.178}$$

The power spectrum can be defined as the correlation between $\tilde{\delta}(\boldsymbol{k})$ and $\tilde{\delta}(\boldsymbol{k'})$

$$\langle \tilde{\delta}(\boldsymbol{k}) \tilde{\delta}(\boldsymbol{k'}) \rangle = (2\pi)^3 \delta^3(\boldsymbol{k} + \boldsymbol{k'}) P(\boldsymbol{k}) \tag{2.179}$$

where $\tilde{\delta}$ is the Fourier transform of the density contrast

$$\tilde{\delta}(\boldsymbol{k}) = \int d^3x e^{-i\boldsymbol{k}\cdot\boldsymbol{x}} \delta(\boldsymbol{x}) \tag{2.180}$$

In terms of the Lagrangian displacement, the power spectrum is

$$P(\boldsymbol{k}) = \int d^3q e^{-i\boldsymbol{k}\cdot\boldsymbol{q}} \left(\langle e^{-\boldsymbol{k}[\Psi(\boldsymbol{q_1}) - \Psi(\boldsymbol{q_2})]} \rangle - 1 \right) \tag{2.181}$$

The cumulant of equation (2.181) can be expanded through the expansion theorem for the expected value of the exponential function

$$K = \langle e^{-iX} \rangle = \exp \left[\sum_{N=1}^{\infty} \frac{(-i)^N}{N!} \langle X^N \rangle_c \right] \tag{2.182}$$

where we can have two approaches depending on how the resummation is done. One called Integrated Perturbation theory (IPT) where the exponential terms evaluated at $q = 0$ are kept and the other called CLPT (Convolution Lagrangian Theory) where the terms that go to zero as $q \longrightarrow \infty$ are expanded.

Integrated Perturbation Theory

Applying the cumulant expansion theorem to the exponent of eq. (2.181)

$$\left\langle \{\boldsymbol{k}\cdot[\Psi(\boldsymbol{q}_1)-\Psi(\boldsymbol{q}_2)]\}^N \right\rangle_c = [1+(-1)^N]\left\langle [\boldsymbol{k}\cdot\Psi(0)]^N \right\rangle_c + \sum_{j=1}^{N-1}(-1)^{N-j}\binom{1}{a}\left\langle [\boldsymbol{k}\cdot\Psi(\boldsymbol{q}_1)]^j [\boldsymbol{k}\cdot\Psi(\boldsymbol{q}_2)]^{N-j}\right\rangle_c \quad , \tag{2.183}$$

In this equation, only $N >= 2$ cases survive because $< \Psi >= 0$ to maintain parity symmetry, and the power spectrum expression can thus be expressed as:

$$P(\boldsymbol{k}) = \exp\left[-2\sum_{n=1}^{\infty}\frac{k_{i_1}...k_{i_N}}{(2n)!}A^{(2n)}_{i_1...i_{2n}}\int d^3q e^{-i\boldsymbol{k}\cdot\boldsymbol{q}}\times \left\{\exp\left[\sum_{N=2}^{\infty}\frac{k_{i_1}...k_{i_N}}{N!}B^{(N)}_{i_1...i_N}\right]-1\right\} \quad , \tag{2.184}$$

where:

$$A^{(2n)}_{i_1...i_{2n}} = (-1)^{n-1}\left\langle \Psi_{i_1}(0)...\Psi_{i_{2n}}(0)\right\rangle_c \tag{2.185}$$

$$B^{(N)}_{i_1...i_N}(\boldsymbol{q}) = \mathrm{i}^N\sum_{j=1}^{N-1}(-1)^j\binom{N}{J}\times\left\langle \Psi_{i_1}(\boldsymbol{q}_1)...\Psi_{i_{j+1}}(\boldsymbol{q}_1)\Psi_{i_{j+1}}(\boldsymbol{q}_2)...\Psi_{i_N}(\boldsymbol{q}_2)\right\rangle_c \quad . \tag{2.186}$$

The term A is the cumulant for a single position displacement vector and B the cumulant where the displacement vector lies at a distance q_i.

These quantities are useful to used them in terms of polyspectra of the displacement field $C_{i_1...i_N}$ (i.e. using high order spectra terms) that are defined as:

$$\left\langle \tilde{\Psi}_{i_1}(\boldsymbol{p}_1)...\tilde{\Psi}_{i_N}(\boldsymbol{p}_N) \right\rangle_c = (2\pi)^3\delta^3(\boldsymbol{p}_1+...+\boldsymbol{p}_N)(-i)^{N-1}C_{i_1...i_N}(\boldsymbol{p}_1,...,\boldsymbol{p}_N) \quad , \tag{2.187}$$

where the Fourier transform of the displacement field is:

$$\tilde{\Psi}_i(\boldsymbol{p}) = \int d^3q e^{-i\boldsymbol{p}\cdot\boldsymbol{q}}\Psi_i(\boldsymbol{q}) \quad . \tag{2.188}$$

To ensure that the polyspectra are real numbers, they must satisfy the relation:

$$\left\langle \tilde{\Psi}_{i_1}(\boldsymbol{p_1})...\tilde{\Psi}_{i_N}(\boldsymbol{p_N}) \right\rangle_c^* = (-1)^N \left\langle \tilde{\Psi}_{i_1}(\boldsymbol{p_1})...\tilde{\Psi}_{i_N}(\boldsymbol{p_N}) \right\rangle_c \quad , \tag{2.189}$$

so the polyspectra meets:

$$C_{i_1...i_N}(-\boldsymbol{p}_1,...,-\boldsymbol{p}_N) = (-1)^N C_{i_1...i_N}(\boldsymbol{p}_1,...,\boldsymbol{p}_N) \quad . \tag{2.190}$$

Given these identities, the equations (2.185) and (2.186) in terms of the polyspectra are:

$$A^{(2n)}_{i_1...i_{2n}} = \int \frac{d^3p_1}{(2\pi)^3}...\frac{d^3p_2}{(2\pi)^3}\delta^3(\boldsymbol{p}_1+...+\boldsymbol{p}_{2n}) \times C_{i_1...i_{2n}}(\boldsymbol{p}_1,...,\boldsymbol{p}_{2n}) \quad , \tag{2.191}$$

$$B^{(N)}_{i_1...i_N}(\boldsymbol{q}) = \sum_{j=1}^{N-1}(-1)^j(NJ) \times \int \frac{d^3p_1}{(2\pi)^3}...\frac{d^3p_2}{(2\pi)^3}\delta^3(\boldsymbol{p}_1+...+\boldsymbol{p}_N)\times e^{i(\boldsymbol{p}_1+...+\boldsymbol{p}_j)\cdot\boldsymbol{q}}C_{i_1...i_N}(\boldsymbol{p}_1,...,\boldsymbol{p}_N) \quad . \tag{2.192}$$

The perturbative displacement field terms in Foruier space can be expressed in perturbative kernel L expansions as:

$$\tilde{\Psi}^{(n)}(\boldsymbol{p}) = \frac{iD^n}{n!}\int \frac{d^3p1}{(2\pi)^3}...\frac{d^3p_n}{(2\pi)^3}(2\pi)^3\delta^3\left(\sum_{j=1}^{n}\boldsymbol{p}_j - \boldsymbol{p}\right) L^{(n)}(\boldsymbol{p_1},...,\boldsymbol{p_n})\delta^{(1)}(\boldsymbol{p_1})...\delta^{(1)}(\boldsymbol{p_n}) \tag{2.193}$$

The L kernels up to third order have the forms:

$$L^{(1)}(\boldsymbol{p_1}) = \frac{\boldsymbol{k}}{k^2} \tag{2.194}$$

$$L^{(2)}(\boldsymbol{p_1}, \boldsymbol{p_2}) = \frac{3}{7}\frac{\boldsymbol{k}}{k^2}\left[1 - \left(\frac{\boldsymbol{p_1}\cdot\boldsymbol{p_2}}{p_1 p_2}\right)\right] \tag{2.195}$$

$$L^{(3a)}(\boldsymbol{p_1}, \boldsymbol{p_2}, \boldsymbol{p_3}) = \frac{5}{7}\frac{\boldsymbol{k}}{k^2}\left[1 - \left(\frac{\boldsymbol{p_1}\cdot\boldsymbol{p_2}}{p_1 p_2}\right)\right]\left\{1 - \left[\frac{(\boldsymbol{p_1}+\boldsymbol{p_2})\cdot\boldsymbol{p_3}}{|\boldsymbol{p_1}+\boldsymbol{p_2}|p_3}\right]^2\right\}$$
$$- \frac{1}{3}\frac{\boldsymbol{k}}{k^2}\left[1 - \left(\frac{\boldsymbol{p_1}\cdot\boldsymbol{p_2}}{p_1 p_2}\right)^2 + 2\frac{(\boldsymbol{p_1}\cdot\boldsymbol{p_2})(\boldsymbol{p_2}\cdot\boldsymbol{p_3})(\boldsymbol{p_3}\cdot\boldsymbol{p_1})}{p_1^2 p_2^2 p_3^2}\right]\boldsymbol{k}\times\boldsymbol{T}(\boldsymbol{p_1}, \boldsymbol{p_2}, \boldsymbol{p_3}) \tag{2.196}$$

where T is the transverse part. The relation of the perturbative terms of the displacement field with the polyspectra for two and three terms are:

$$\left\langle \tilde{\Psi}_i^{(n)}(\boldsymbol{p})\tilde{\Psi}_j^{(m)}(\boldsymbol{p'})\right\rangle_c = (2\pi)^3\delta^3(\boldsymbol{p}+\boldsymbol{p'})C_{ij}^{(nm)}(\boldsymbol{p}) \quad , \tag{2.197}$$

$$\left\langle \tilde{\Psi}_i^{(n)}(\boldsymbol{p_1})\tilde{\Psi}_j^{(m)}(\boldsymbol{p_2})\tilde{\Psi}_k^{(l)}(\boldsymbol{p_3})\right\rangle_c = (2\pi)^3\delta^3(\boldsymbol{p_1}+\boldsymbol{p_2}+\boldsymbol{p_3})C_{ijk}^{(nml)}(\boldsymbol{p1}, \boldsymbol{p2}, \boldsymbol{p3}) \quad . \tag{2.198}$$

The polyspectra in terms of the kernels REF are:

$$C_{ij}^{(11)}(\boldsymbol{p}) = L_i(\boldsymbol{p})^{(1)}L_j(\boldsymbol{p})^{(1)}P_L(p) \tag{2.199}$$

$$C_{ij}^{(22)}(\boldsymbol{p}) = \frac{1}{2}\int\frac{d^3p'}{(2\pi)^3}L_i^{(2)}(\boldsymbol{p'}, \boldsymbol{p}-\boldsymbol{p'})P_L(p')P_L(|\boldsymbol{p}-\boldsymbol{p'}|) \tag{2.200}$$

$$C_{ij}^{(13)} = C_{ji}^{(31)} = \frac{1}{2}L_i^{(1)}(\boldsymbol{p})P_L(\boldsymbol{p})\int\frac{d^3p'}{(2\pi)^3}L_j^{(3)}(\boldsymbol{p}, -\boldsymbol{p'}, \boldsymbol{p'})P_L(p') \tag{2.201}$$

$$\begin{aligned} C_{ijk}^{(112)}(\boldsymbol{p_1}, \boldsymbol{p_2}, \boldsymbol{p_3}) = C_{kij}^{(211)}(\boldsymbol{p_3}, \boldsymbol{p_1}, \boldsymbol{p_2}) = C_{jki}^{(121)}(\boldsymbol{p_2}, \boldsymbol{p_3}, \boldsymbol{p_1}) = \\ - L_i^{(1)}(\boldsymbol{p_1})L_j^{(1)}(\boldsymbol{p_2})L_k^{(2)}(\boldsymbol{p_1}, \boldsymbol{p_2})P_L(p_1)P_L(p_2) \end{aligned} \tag{2.202}$$

So the expression of the power spectrum from quantities A and B in terms of polyspectra is:

$$P(\boldsymbol{k}) = \exp\left[-k_i k_j \int \frac{d^3p}{(2\pi)^3} C_{ij}^{(11)}(\boldsymbol{p})\right] \times \Big\{ k_i k_j \left[C_{ij}^{(11)}(\boldsymbol{k}) + C_{ij}^{(22)}(\boldsymbol{k}) + C_{ij}^{(13)}(\boldsymbol{k}) + C_{ij}^{(31)}(\boldsymbol{k}) + k_i k_j k_k \int \frac{d^3p}{(2\pi)^3} \left[C_{ijk}^{(112)}(\boldsymbol{k}, -\boldsymbol{p}, \boldsymbol{p}-\boldsymbol{k}) + C_{ijk}^{(121)}(\boldsymbol{k}, -\boldsymbol{p}, \boldsymbol{p}-\boldsymbol{k}) + C_{ijk}^{(211)}(\boldsymbol{k}, -\boldsymbol{p}, \boldsymbol{p}-\boldsymbol{k}) + \frac{1}{2} k_i k_j k_k k_l \int \frac{d^3p}{(2\pi)^3} C_{ij}^{(}11)(\boldsymbol{p}) C_{kl}^{(11)}(\boldsymbol{k}-\boldsymbol{p}) \Big\} \quad , \tag{2.203}$$

where integrating the cumulants, the nonlinear power spectrum at one loop in the Integrated Perturbation theory is:

$$P(k) = \left[-\frac{k^2}{6\pi^2} \int dp P_L(p)\right] \times \Big\{ P_L(k) + \frac{1}{98} \frac{k^3}{4\pi^2} \int_0^\infty dr P_L(kr) \int_{-1}^1 dx P_L[k(1+r^2-2rx)^{1/2}] \frac{(3r+7x-10rx^2)^2}{(1+r^2-2rx)^2} + \frac{1}{252} \frac{k^3}{4\pi^2} P_L(k) \int_0^\infty dr P_L(kr) \left[\frac{12}{r^2} + 10 + 100r^2 - 42r^4 + \frac{3}{r^3}(r^2-1)^3(7r^2+2) \ln\left|\frac{1+r}{1-r}\right| \right] \Big\} \quad . \tag{2.204}$$

2.9.3 Convolution Lagrangian Perturbation Theory

Using the displacement vector field as:

$$\Delta = \Psi(\boldsymbol{q}_2) - \Psi(\boldsymbol{q}_1) \quad , \tag{2.205}$$

equation (2.182) is expressed as:

$$\log K = \sum_{N=1}^{\infty} \frac{(-i)^N}{N!} \left\langle (\boldsymbol{k} \cdot \Delta)^N \right\rangle_c \tag{2.206}$$

So the power spectrum from REF can be written as

$$(2\pi)^3 \delta_D(\boldsymbol{k}) + P(k) = \int d^3q \, e^{i\boldsymbol{k}\cdot\boldsymbol{q}} \exp\left[-\frac{1}{2} k_i k_j \langle \Delta^i \Delta^j \rangle_c - \frac{1}{6} k_i k_j k_k \langle \Delta^i \Delta^j \Delta^k \rangle_c \right], \tag{2.207}$$

where different resummation schemes will lead us to different expressions for the power spectrum.In the previous section, we adopted the resummation evaluating the exponential terms in $\boldsymbol{q} = 0$ [43]. In this section we expand the terms that goes to zero as $\boldsymbol{q} \longrightarrow \infty$. Considering up to the third cummulant using the expansion at $\boldsymbol{q} \longrightarrow \infty$ we obtain

$$\log K = -\frac{1}{2}k_i k_k A_{ij}(\boldsymbol{q}) + \frac{i}{6}k_i k_j k_l W_{ijl}(\boldsymbol{q}) \quad . \tag{2.208}$$

Which implies the evaluation of two cumulants

$$A_{ij}(\boldsymbol{q}) = \langle \Delta_i \Delta_j \rangle_c$$

$$W_{ijk}(\boldsymbol{q}) = \langle \Delta_i \Delta_j \Delta_k \rangle_c \tag{2.209}$$

So the expression for the PS is

$$(2\pi)^3 \delta_D(\boldsymbol{k}) + P(k) = \int d^3q \, e^{i\cdot\boldsymbol{q}} \exp\left[-\frac{1}{2}k_i k_j A_{ij}(\boldsymbol{q}) + \frac{i}{6}k_i k_j k_l W_{ijl}(\boldsymbol{q})\right] \quad . \tag{2.210}$$

The displacement cumulant can de decomposed as

$$A_{ij}(\boldsymbol{q}) = X(q)\delta^K_{ij} + Y(q)\hat{q}_i\hat{q}_j \tag{2.211}$$

$$W_{ijk}(\boldsymbol{q}) = V(q)\hat{q}_{\{i\delta^K_{jk}\}} + T(q)\hat{q}_i\hat{q}_j\hat{q}_k \tag{2.212}$$

$X(q)$,$Y(q)$,$V(q)$ and $T(q)$ are scalar functions that depend of the amplitude of separation q. Contracting the indexes of the tensors and solving the system we get

$$\left.\begin{array}{l} A_0 \equiv \delta^K_{ij} A_{ij} = 3X + Y \\ \vec{A} \equiv \hat{q}_i\hat{q}_j A_{ij} = X + Y \end{array}\right\} \longrightarrow \quad \begin{array}{l} X = 1/2\ (A_0 - \vec{A}) \\ Y = 1/2\ (3\vec{A} - A_0) \end{array} \quad , \tag{2.213}$$

for the second cumulant we have

$$\left.\begin{array}{l} W_0 \equiv \hat{q}_i\delta^K_{ij} W_{ijk} = 5V + T \\ \vec{W} \equiv \hat{q}_i\hat{q}_j\hat{q}_k W_{ijk} = 3V + T \end{array}\right\} \longrightarrow \quad \begin{array}{l} V = 1/2\ (W_0 - \vec{W}) \\ T = 1/2\ (5\vec{W} - 3W_0) \end{array} \quad . \tag{2.214}$$

Thus PS can be re-written as

$$(2\pi)^3\delta^D(k)+P(k) = \int d^3q e^{i\mu k(q-\frac{1}{2}k^2V)}\exp\left[-\frac{1}{2}k^2(X+\mu^2Y)-\frac{i}{6}\mu^3k^3T\right] \tag{2.215}$$

2.10 Primordial non-Gaussianity

The behavior of the quantum fluctuation during inflation, determined the well potentials where matter eventually fell into them, that distribution is printed in the actual halos and galaxies distribution. From the CMB which is the earliest information we have, we can measure the primordial distribution and it tells us that it is not strictly Gaussian; it has some deviations that, as will be mentioned afterwards, can be parametrized into parameters from the curvature perturbations such as $f_{NL}, g_{NL}, h_{NL,...}$ (these parameters will be described in later sections). The restriction for non-Gaussianity parameters from the CMB are $-154 < f_{NL} < 94$ and $-5.6\times10^5 < g_{NL} < 6.4\times10^5$.

On the other hand, considering a single scalar field ($_\varphi$) and radiation fluid ($_\gamma$) , we can use the fact that the total second-order curvature perturbation, can be written in terms of first-order perturbations such as:

$$\zeta^{(2)} = -\mathcal{H}\frac{\delta^{(2)}\rho}{\rho'} - \left[f\zeta_\varphi^{(1)}+(1-f)\zeta_\gamma^{(1)}\right]\left[f^2\zeta_\varphi^{(1)}+(1+f)(2+f)\zeta_\gamma^{(1)}\right], \tag{2.216}$$

where

$$\zeta_\varphi^{(1)} = -\mathcal{H}\left(\frac{\delta^{(1)}\rho_\varphi}{\rho'_\varphi}\right) \tag{2.217}$$

$$\zeta_\gamma^{(1)} = -\mathcal{H}\left(\frac{\delta^{(1)}\rho_\gamma}{\rho'_\gamma}\right). \tag{2.218}$$

In a longitudinal gauge, for large scales, the relation between the density curvature perturbation $\zeta^{(1)}$ and the comoving curvature perturbation

$\mathcal{R}^{(1)}$ is $\zeta^{(1)} \sim -\mathcal{R}^{(1)}$. The second-order curvature perturbation in terms of the first-order element in a slow-roll scenario is:

$$\mathcal{R}^{(2)} = (\eta - 3\varepsilon)\left(\mathcal{R}^{(1)}\right)^2 + \mathcal{I}, \tag{2.219}$$

where $\mathcal{I}$ is an integral of non-local operators. In Fourier space, the curvature perturbation is:

$$\begin{aligned}\mathcal{R}(\mathbf{k}) =& \mathcal{R}^{(1)}(\mathbf{k}) + \frac{1}{(2\pi)^3}\int d^3k_1 d^3k_2 \delta^{(3)}(\mathbf{k}_1 + \mathbf{k}_2 - \mathbf{k})\times \\ & f_{NL}(\mathbf{k}_1, \mathbf{k}_2)\mathcal{R}^{(1)}(\mathbf{k}_1)\mathcal{R}^{(1)}(\mathbf{k}_2),\end{aligned} \tag{2.220}$$

where the f_{NL} have the slow-roll parameters such as:

$$f_{NL}(\mathbf{k}_1, \mathbf{k}_2) = \frac{1}{2}(\eta - 3\varepsilon) + I(\mathbf{k}_1, \mathbf{k}_2). \tag{2.221}$$

2.10.1 Primordial Non-Gaussianity triangle configurations

The expansion for the curvature perturbations in terms of a Gaussian random field, are:

$$\zeta = \zeta^{(1)} + \frac{3}{5}f_{NL}\zeta^{(1)2} + \frac{9}{25}g_{NL}\zeta^{(1)3} + \frac{27}{125}h_{NL}\zeta^{(1)4} + ... \quad . \tag{2.222}$$

where $\zeta^{(1)}$ is the Gaussian random field and the parameters f_{NL}, g_{NL}, h_{NL} are the amplitude of the different orders of the expansion. Considering just a second order and local effects, we have the curvature perturbations as:

$$\zeta = \zeta^{(1)} + \frac{3}{5}f_{NL}^{local}\left[\zeta^{(1)2} - \left\langle\zeta^{(1)2}\right\rangle\right] \quad . \tag{2.223}$$

As the power spectrum, we analyze the correlation of 2 points that take form of a line, the bispectrum forms triangle due we correlate 3 points of k:

$$B(k_1, k_2, k_3) = \frac{6}{5}f_{NL}^{local}\left[P(k_1)P(k_2) + P(k_2)P(k_3) + P(k_3)P(k_1)\right] \quad , \tag{2.224}$$

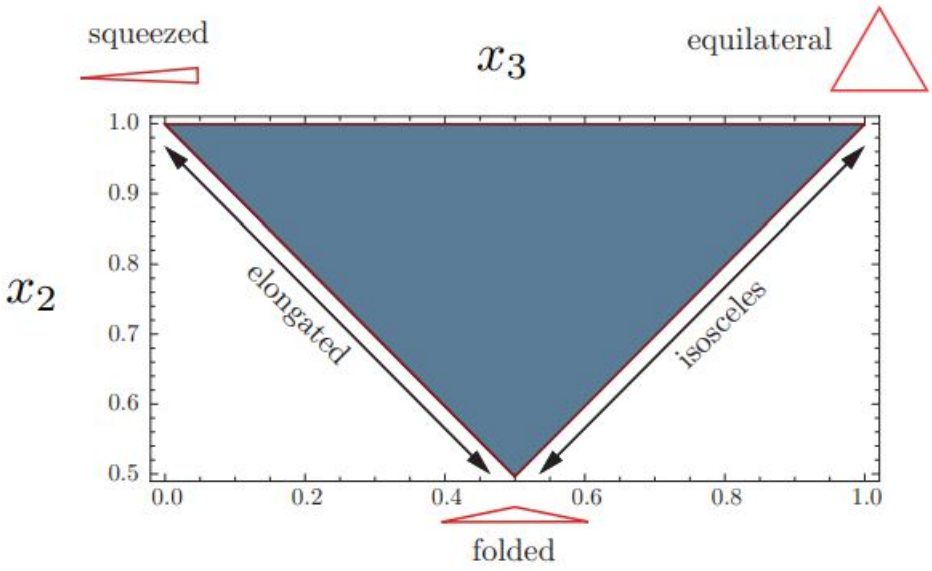

Figure 2.7 Shapes of non-Gaussianity

so these triangles may have different shapes, where we denote the shape function as:

$$S(k_1, k_2, k_3) \equiv N(k_1, k_2, k_3)^2 B(k_1, k_2, k_3) \quad , \tag{2.225}$$

we can establish the shape function for the local and equilateral models as:

$$S^{local}(k_1, k_2, k_3) \propto \frac{k_1^3 k_2^3 k_3^3}{\Delta_1^3 (k_1 k_2 k_3)} \quad , \tag{2.226}$$

$$S^{equil}(k_1, k_2, k_3) \propto \frac{3(k_1^3 k_2^3 k_3^3) - 2(k_1 + k_2 + k_3)}{\Delta_1^3 (k_1 k_2 k_3)} \quad , \tag{2.227}$$

where with the rescaling $x_i \equiv k_i / k_1$ we have the shapes of non-Gaussianity as Figure 2.7.

2.11 3 point correlation function

The three point correlation function (3PCF)is a valuable statistic tool which contains information that cannot be extracted from the 2PCF. The three point correlation is an indicator of the deviation from Gaussian statistics. To account for it, instead of counting pairs, for the 3PCF we are counting triplets (i.e. triangles), and some important information will be in the different configuration of triangles. If we had a perfectly gaussian distribution, the correlation functions of order higher than two would all be written in terms of the 2PCF. The bispectrum is defined as the Fourier transform of the three point correlation, which means

$$\xi^{(3)}(\boldsymbol{r}_1, \boldsymbol{r}_2, \boldsymbol{r}_3) = \frac{1}{(2\pi)^6} \int d^3\boldsymbol{k}_1 d^3\boldsymbol{k}_2 d^3\boldsymbol{k}_3 B(\boldsymbol{k}_1, \boldsymbol{k}_2, \boldsymbol{k}_3) \times e^{i(\boldsymbol{k}_1\cdot\boldsymbol{r}_1 + \boldsymbol{k}_2\cdot\boldsymbol{r}_2 + \boldsymbol{k}_3\cdot\boldsymbol{r}_3)} \delta_D(\boldsymbol{k}_1 + \boldsymbol{k}_2 + \boldsymbol{k}_3) \tag{2.228}$$

There are three known sources for a non-zero bispectrum [1].

a) Primordial non-gaussiantiny: This can be described by the local expression for Bardeen's curvature perturbations during the matter era

$$\Phi(\boldsymbol{x}) = \Phi_G(\boldsymbol{x}) + f_{NL}^{loc}\left[\Phi_G^2(\boldsymbol{x}) - \Phi_G^2(\boldsymbol{x})\rangle\right] \tag{2.229}$$

where $\Phi_G(\boldsymbol{x})$ is a Gaussian field and f_{NL}^{loc} is the amplitude of primordial non-gaussianity in the so-called local limit. The contribution of this amplitude to the bispectrum is given by

$$B_\Phi^{local} = 2 f_{NL}^{loc}\, C_\Phi^2 \left[\frac{1}{k_1^{4-n} k_2^{4-n}} + \text{cyc.}\right] \quad , \tag{2.230}$$

which quantifies the variations on the power spectrum. The primordial matter bispectrum is then given by

$$B_I(k_1, k_2, k_3) = M(k_1)M(k_2)M(k_3)B_\Phi(k_1, k_2, k_3) \quad , \tag{2.231}$$

The reduced bispectrum is often used in order to have a more visual representation. The reduced bispectrum for B_I is

$$Q(k_1, k_2, k_3) = \frac{B_I(k_1, k_2, k_3)}{P(k_1)P_(k_2) + \text{cyc.}} \quad . \tag{2.232}$$

b) Due non-linear gravitational evolution As time goes by, matter interacts via gravitational forces, which produces a deviation from even the primordial distribution making the actual distribution non-linear. On large scales the density fluctuations can be studied with perturbation theory (described in Chaper 3), up to second order in δ is

$$\delta_{\boldsymbol{k}} \simeq \delta^{(1)}_{\boldsymbol{k}} + \int d^3q1 d^3q_2 \delta_D(\boldsymbol{k} - \boldsymbol{q}_{12}) F_2(\boldsymbol{q}_1, \boldsymbol{q}_2) \delta^{(1)}_{\boldsymbol{q}_1} \delta^{(1)}_{\boldsymbol{q}_2} \quad , \tag{2.233}$$

where $F_2(\boldsymbol{q}_1, \boldsymbol{q}_2)$ is the kernel for the evolution of the perturbation. And the contribution to the bispectrum is given by

$$B_g(k_1, k_2, k_3) = 2F_2(\boldsymbol{q}_1, \boldsymbol{q}_2) P_L(k1) P_L(k2) + \text{cyc.} \quad . \tag{2.234}$$

The bispectrum of matter density fluctuation is given by the primordial bispectrum (equation (2.230)) and the one due the gravitational evolution (equation (2.234))

$$B(k_1, k_2, k_3) = B_I(k_1, k_2, k_3) + B_G(k_1, k_2, k_3) \tag{2.235}$$

The reducen bispectrum is

$$Q(k_1, k_2, k_3) = Q_I(k_1, k_2, k_3) + Q_G(k_1, k_2, k_3) = \\ \frac{B_I(k_1, k_2, k_3)}{P(k_1)P_(k_2) + \text{cyc.}} + \frac{B_G(k_1, k_2, k_3)}{B_I(k_1, k_2, k_3)} P(k_1)P_(k_2) + \text{cyc.} \quad . \tag{2.236}$$

c) Due non-linear galaxy bias We can assume that galaxy formation is a local process and depends only on the local matter density field. We can expand in Taylor series the matter overdensity as

$$\delta_g \boldsymbol{x} \simeq b_1 \delta(\boldsymbol{x}) + \frac{1}{2} b_2 \delta^2(\boldsymbol{x}) \quad , \tag{2.237}$$

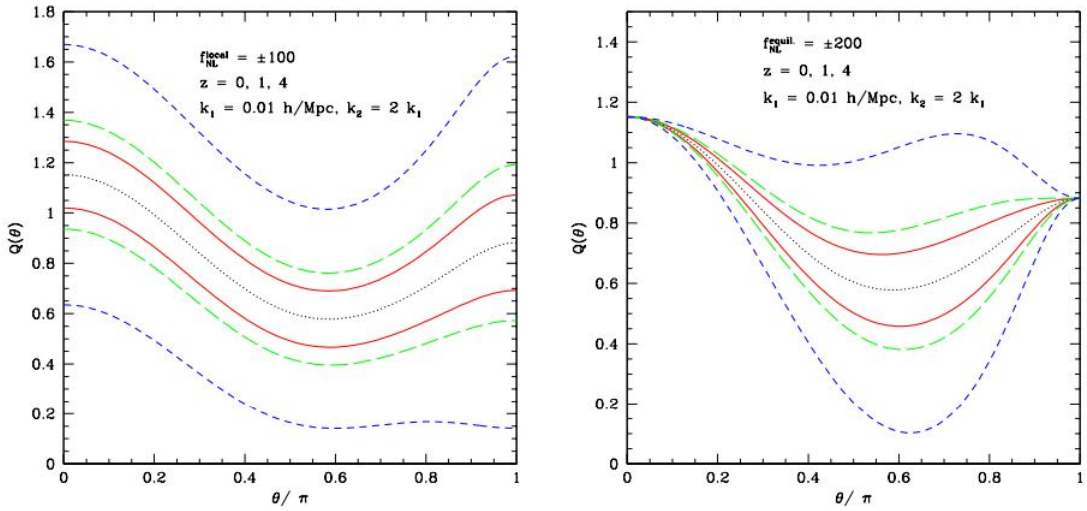

Figure 2.8 Configuration dependence of the reduced bispectrum of dark matter distribution from Gaussian and non-Gaussian initial conditions, as a function of an angle θ [1].

where b_1 and b_2 are the linear and non-linear bias parameters. The galaxy bispectrum is then

$$B_g(k_1, k_2, k_3) \simeq b_1^3 B(k_1, k_2, k_3) + b_1^2 b_2 [P_L(k_1)P_L(k_2) + \text{cyc.}] \quad . \quad (2.238)$$

In Figure 2.8 one can appreciate the reduced bispectrum for different values of an inital f_{NL} and different redshifts.

We can see how the different contributions to the bispectrum **a), b)** and **c)** affect the shape and the triplet counts.

2.12 Covariance matrix

As of late the covariance matrix has been an important tool to precision cosmology because it can be employed in many different ways. It can be used for measuring statistical properties of different realizations of simulated artificial catalogs or given a data set of cosmological parameters.

The covariance matrix can also be used for estimating the dependence between different scales analyzing the non-diagonal data of the covariance matrix. Defining the 2 point correlation function of a density field δ in cells i, j as:

$$\xi_{ij} = \delta_i \delta_j \tag{2.239}$$

$$\begin{aligned}\mathrm{Cov}(\xi_{ij}, \xi_{kl}) = \langle \xi_{ij}\xi_{kl} \rangle - \langle \xi_{ij} \rangle \langle \xi_{kl} \rangle = \langle \delta_i \delta_j \delta_k \delta_l \rangle - \langle \delta_i \delta_j \rangle \langle \delta_k \delta_l \rangle = \\ \langle \xi_{ijkl} \rangle + \langle \xi_{ik} \rangle \langle \xi_{jl} \rangle + \langle \xi_{il} \rangle \langle \xi_{jk} \rangle\end{aligned} \tag{2.240}$$

Recent studies have proposed new calculations for covariance matrices using an expansion of the two point correlation function. Firstly it is considered a two point correlation function estimator in radial-angular space (r, μ), where $\mu = \cos\theta$, in this case, the Landy-Szalay estimator yields:

$$\hat{\xi}(r, \mu) = \frac{NN(r, \mu)}{RR(r, \mu)} \quad , \tag{2.241}$$

considering a simulation or galaxy catalog as D and a random distribution R, then $N = (D - R)$. Taking a bin for the radial and angular coordinates a and c respectively:

$$\hat{\xi}^a_c = \frac{NN^a_c}{RR^a_c} \quad , \tag{2.242}$$

the terms of the fraction are defined as:

$$NN^c_a = \sum_{i \neq} n_i n_j w_i w_j \Theta^a(r_{ij}) \Theta^c(\mu_{ij}) \delta_i \delta_j \quad , \tag{2.243}$$

$$RR^c_a = \sum_{i \neq} n_i n_j w_i w_j \Theta^a(r_{ij}) \Theta^c(\mu_{ij}) \quad , \tag{2.244}$$

where Θ is the binning matrix that takes the value of 1 if contains the points i, j and 0 if not. So equation (2.240) is:

$$cov(\hat{\xi}_c^a, \hat{\xi}_d^b) \equiv C_{cd}^{ab} = \left\langle \hat{\xi}_c^a \hat{\xi}_d^b \right\rangle - \left\langle \hat{\xi}_c^a \right\rangle \left\langle \hat{\xi}_d^b \right\rangle =$$
$$\frac{1}{RR_c^a RR_c^b} \sum_{i \neq j} \sum_{j \neq l} n_i n_j n_k n_l w_i, w_j w_k w_l \Theta^a(r_{ij}) \Theta^c(\mu_{ij}) \Theta^b(r_{kl}) \Theta^d(\mu_{kl})$$
$$[\langle \delta_i \delta_j \delta_k \delta_l \rangle - \langle \delta_i \delta_j \rangle \langle \delta_k \delta_l \rangle] \quad , \tag{2.245}$$

where:

$$\langle \delta_i \delta_j \delta_k \delta_l \rangle - \langle \delta_i \delta_j \rangle \langle \delta_k \delta_l \rangle = \xi_{ijkl}^{(4)} + \xi_{ik}\xi_{jl} + \xi_{il}\xi_{jk} \quad , \tag{2.246}$$

where $\xi_{ijkl}^{(4)}$ is the four point correlation function

$$\langle \delta_i \delta_j \delta_k \delta_l \rangle - \langle \delta_i \delta_j \rangle \langle \delta_k \delta_l \rangle \sim \frac{\alpha}{n_j} \langle (1 + \delta_i) \delta_i \delta_k \rangle = \frac{\alpha}{n_i} \sim (\zeta ijk + \xi_{ik}) \tag{2.247}$$

α is the shot-noise rescaling factor. ζ_{ijk} is the three point correlation function, and the equation can be rewritten in terms of the the weight function as:

$$\langle \delta_i \delta_j \delta_k \delta_l \rangle - \langle \delta_i \delta_j \rangle \langle \delta_k \delta_l \rangle \sim \frac{\alpha^2}{n_i n_j} \langle (1 + \delta_i) \delta_i \delta_k \rangle = \frac{\alpha^2}{n_i n_j} \sim (1 + \xi_{ij}) \quad . \tag{2.248}$$

Using the identity:

$$\sum_{i \neq j} \sum_{k \neq l} X_{ij} \tag{2.249}$$

So the full covariance matrix is:

$$C_{cd}^{ab} = {}^4C_{cd}^{ab} + \alpha \times {}^3C_{cd}^{ab} + \alpha^2 \times {}^2C_{cd}^{ab} \tag{2.250}$$

2.12.1 Fisher Matrix

The Fisher Information Matrix if often used to compute the accuracy of cosmological parameters from simulations, which is the expectation value

of a given quantity Θ in the point $\Theta = \Theta_0$ (where $\Theta = (\theta_1, \theta_2, ..., \theta_m)$) coincides in the maximum likelihood point on average. It relates to the covariance matrix as:

$$F_{ij} = C_{ij}^{-1} \quad . \tag{2.251}$$

The Fisher Matrix can be interpreted as how quick the likelihood function converges around the maximum likelihood point. This is defined as:

$$F_{i,j} = -\left\langle \frac{\partial \ln f}{\partial\theta_i \partial\theta_j} \right\rangle \quad , \tag{2.252}$$

where L is the likelihood function. From a Gaussian distribution:

$$F_{ij} = \frac{1}{2}\mathrm{tr}\left[C^{-1}\frac{\partial C}{\partial\theta_i}C^{-1}\frac{\partial C}{\partial\theta_j}\right] + \frac{\partial\mu^t}{\partial\theta_i}C^{-1}\frac{\partial C}{\partial\theta_i} \quad . \tag{2.253}$$

We take the inverse of the squared Fisher matrix of equation (2.254) to compute the variance given a certain volume [44]; that is,

$$F_{i,j} = \frac{V_s}{4\pi^2}\int_{-1}^{1} d\mu \int_{k_{min}}^{k_{max}} dk \frac{\partial P(k,\mu)^S}{\partial p_i}\left(P(k,\mu) + \frac{1}{n}\right)^{-2}\frac{\partial P(k,\mu)^S}{\partial p_j} \quad . \tag{2.254}$$

Chapter Three

Implementation in numerical simulations

We studied Perturbation theory which allow us to have an analysis at a slightly non-linear but analytical regime. Using numerical techniques, we can have a (nearly) fully non-linear evolution. With current technological improvements, numerical simulations has been widely used in astronomy and astrophysics, from stats formations to the study of large scale structures for cosmological volumes. In this work, we focus on cosmological N-body simulations.

First, we analyze de impact of the different solutions for the power spectrum. In Figure 3.1 we can find the power spectrum fully described in Section 3.1, where it can be seen that the higher order (the orange line, where nonlinear 2LPT approximation described below)) generates larger amplitude at high k, but at large-scales the three approximations have a good agreement.

3.1 N-body simulations with COLA method

The COLA method has a more accurate approximation than 2LPT, with less computation time. For this method, the prescription for the second

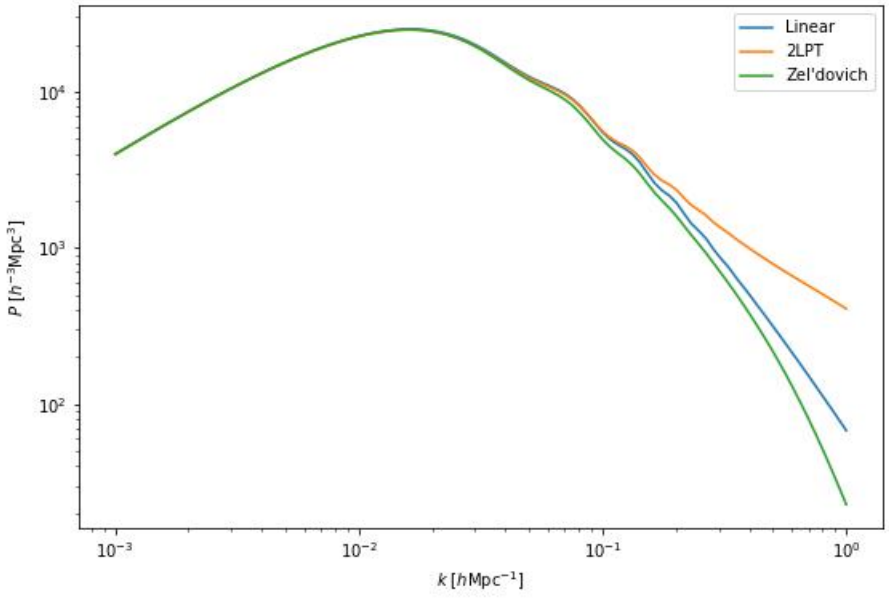

Figure 3.1 Matter power spectrum computed through several approximations. First is the linear Eulerian result in blue. The green line corresponds to the linear Lagrangian or Zel'dovich approximation, and the second order (2LPT) approximation is given by the orange line.

order of the growth function in a ΛCDM background is:

$$D_2(\tau) = -\frac{3}{7} D_1^2(\tau) \Omega_m(\tau)^{-1/143} \quad . \tag{3.1}$$

The equation for the displacement is split as follows:

$$T[\Psi_{res}] + T[D_1]\Psi^{(1)} + T[D_2]\Psi_2 + \nabla^2 \Psi = 0 \tag{3.2}$$

where Ψ_{res} is the remaining displacement when we subtract the quasilinear 2LPT displacements from the full, non-linear displacement for each particle, and the operator $T[X]$ is:

$$T[X] = \frac{d^2 X}{d\tau^2} + \mathcal{H} \frac{dX}{d\tau} \quad . \tag{3.3}$$

For the gradient of Φ the Particle-Mesh algorithm in Fourier space is used as:

$$\nabla\Phi = IFFT\left[\frac{3}{2}\frac{\Omega_{m,0}\boldsymbol{k}}{ak^2} \times FFT[\rho(\boldsymbol{x}) - 1]\right] \tag{3.4}$$

The equation (3.2) is discretized using the Kick-Drift-Kick algorithm where at each iteration the velocity and position of each particle is updated based on the gravitational potential Φ and the stored 2LPT displacements.

$$\boldsymbol{v}_{i+1/2} = \boldsymbol{v}_{i-1/2} - T[\Phi_{res}]\Delta a_1 \quad , \tag{3.5}$$

$$\boldsymbol{r}_i = \boldsymbol{r}_i\boldsymbol{v}_{i+1/2}\Delta a_2 + \Delta D_1\Psi_1 + \Delta D_2\Psi_2 \quad , \tag{3.6}$$

where $\Delta D = D_{i+1} - D_i$ is the change in time of the growth functions. Δa_i are the time intervals for each time-step:

$$\Delta a_1 = \frac{H_0}{nLPT}\frac{a_{i+1/2}^{nLPT} - a_{i-1/2}^{nLPT}}{a_i^{nLPT-1}} \quad , \tag{3.7}$$

$$\Delta a_1 = \frac{H_0}{a_{i+1/2}^{nLPT}}\int_{a_1}^{a_i+1}\frac{a^{nLPT-3}}{H(a)}da \quad , \tag{3.8}$$

where the choice for Δa_i is arbitrary, also $nLPT$ but the value of 25 has shown the best results. The COLA method [7], [8] employs a fixed particle mesh using PM algorithm (Particle-Mesh), where a mesh is placed over the particles and solve for the gravitational interactions at each mesh point then, the force is interpolated to find the values for each particle. The steps at each iteration is:

- Linear interpolation via Cloud-in-cell method to establish the mass density $\rho(x)$ at each mesh point.

- Use the Fourier transform to solve the comoving Poisson equation:

$$k^2\phi(\boldsymbol{k}) = \frac{3}{2}\frac{\Omega_{m,0}}{a}(\rho(\boldsymbol{k}) - 1) \tag{3.9}$$

- Then with the gravitational potential and the inverse Fourier Transform, the force in each direction in real space is generated.
- The acceleration is calculated using the Cloud-in-Cell interpolation.

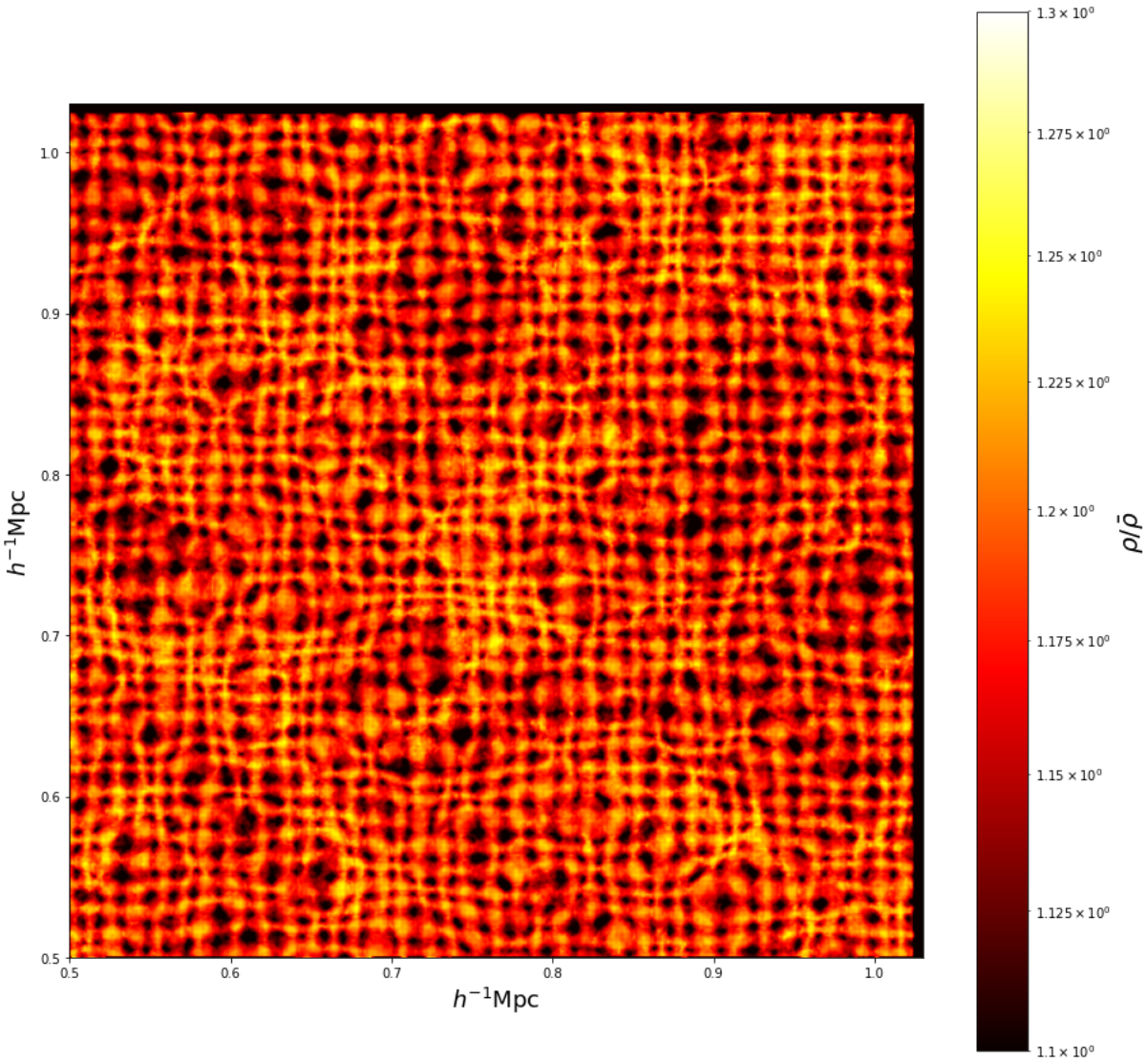

Figure 3.2 Initial conditions of a Gaussian simulation

In Figure 3.2 is the initial conditions for a Gaussian simulation with 1024^3 particles. In Figure 3.3 is the result of the gravitational evolution

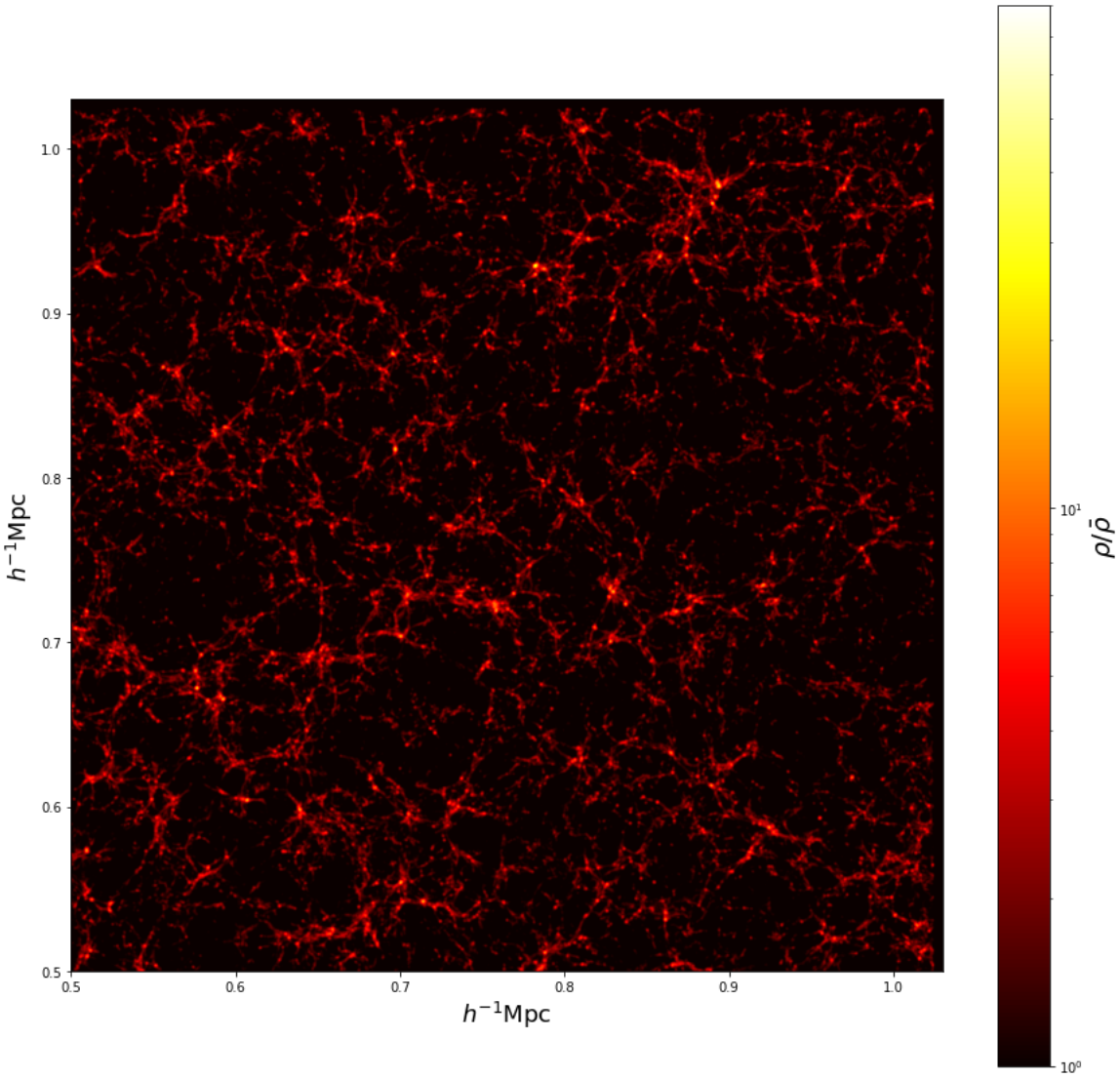

Figure 3.3 Evolution at $z = 1$ for the Gaussian initial conditions

in 70 steps until a redshift of $z = 1$. We can observe the formation of high density zones (white) and very low density zones called *voids* (black). In the following sections we will mention the difference with the relativistic and PNG initial conditions.

3.1.1 Numerical effects in simulations

Given the initial conditions with the same box size, the number of particles will determine the resolution of the simulation as:

$$Res = \frac{Number\ of\ particles}{Length\ of\ the\ box} \quad . \tag{3.10}$$

Figure 3.4 is a ΛCMD simulation in L-PICOLA where all the parameters are constant (Boxsize=1024 MPc, steps=40) except for the number of particles. The nomenclature is as follows: l corresponds to low resolution where the number of particles is 256, m corresponds to medium resolution where the number of particles is 512 and h corresponds to low resolution where the number of particles is 1024. The initial conditions established at redshift $z = 49$. It can be seen that for redshift $z = 0$ the non-linearities due evolution at $k = 1$ have more amplitude in h resolution than m resolution and l resolution can not detect those scales due the number of particles. The "hook-like" morphology at the highest k for the power spectra are an effect of the boxsize and number of particles, it is not a physical effect.

3.1.2 Effects due to number of steps

The number of steps in cosmological simulations determines the quality of how the equations of motion will be numerically solved. In Figures 3.5 and 3.6 one can observe that the non-linearities at small scales are the most affected when choosing the number of steps, the higher they are, the better the non-linearities can be reproduced, also this factor has more of an impact at small redshift z where the non-Gaussianity due evolution is higher and not very well reproduced when choosing a small number of steps.

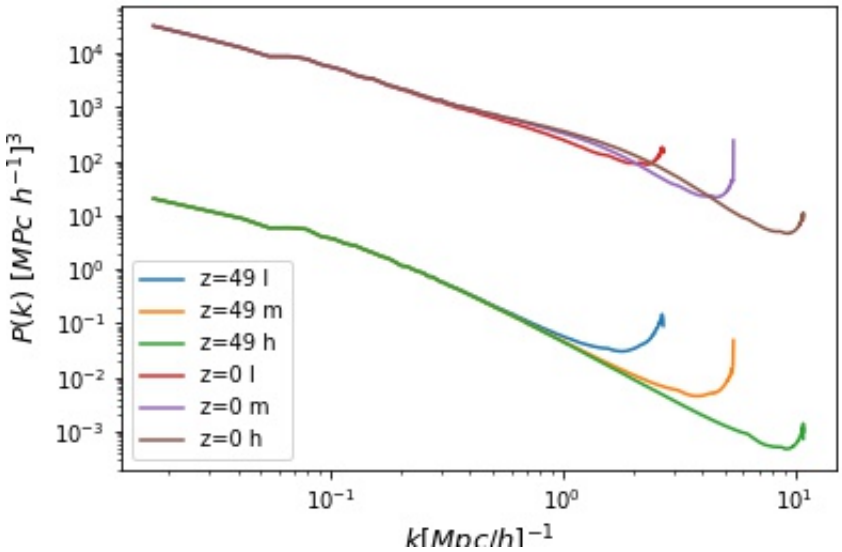

Figure 3.4 Cosmological simulations with different resolutions

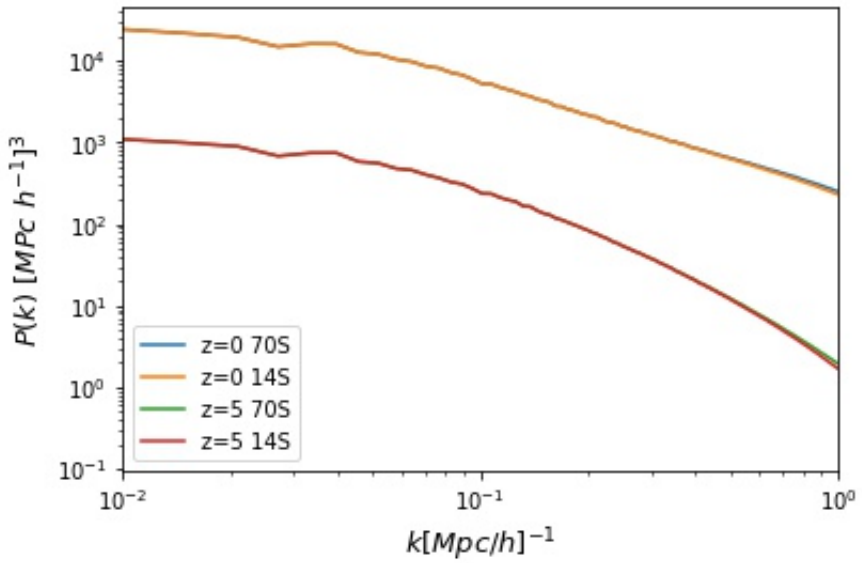

Figure 3.5 Power spectrum for cosmological simulations with same parameters except for the number of steps.

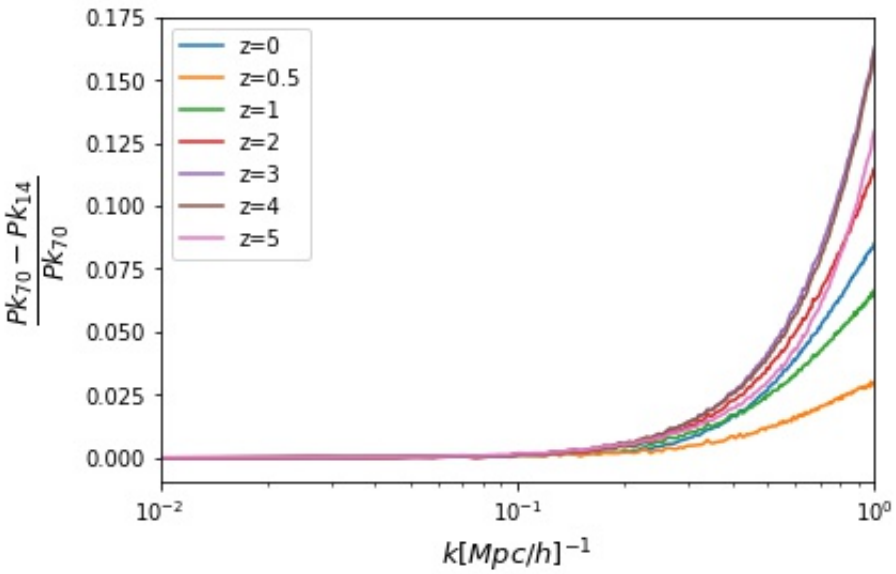

Figure 3.6 Power spectrum ratio for cosmological simulations with same parameters except for the number of steps.

3.1.3 Effects of the volume in the Fisher Matrix

Because the Fisher Matrix is used for survey error analysis, it is important to have a sensitivity of how the parameters behave. One off these parameters is how the volume affects the the different scales. In the Figure 3.7, we used equation (2.254) for different seen area from a survey. The orange shadow corresponds to a Eucid like-survey.

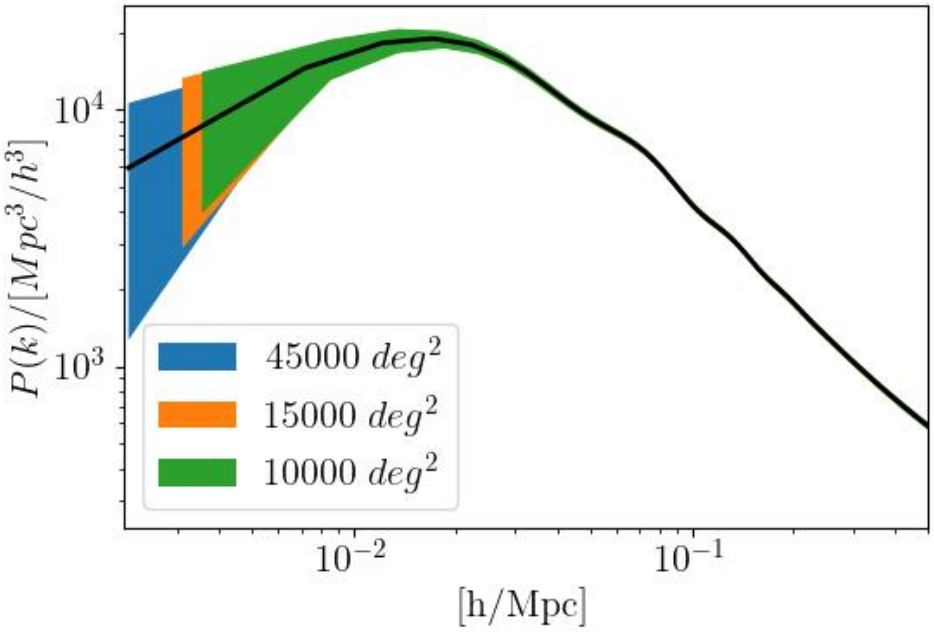

Figure 3.7 Sensitivity for different areas detected by a survey.

3.2 Initial Condition implementation and Numerical Evolution

The main objective in this thesis is the implementation of the PNG and relativistic contributions of Eqs. (2.170) and (2.171) into L-PICOLA, for this is needed to change from the density contrast to the gravitational field. This modifications are relevant because now we are capable to have primordial contributions in Newtonian evolution for cosmological simulations in order to study the early Universe. As a first approximation this was implemented into a fixed-mesh code and for future works this also can be tested for adaptive-mesh and more computational resources demanding codes as Gadget or also into full-GR evolution codes as GRAMES of GEVOLUTION.

In order to introduce a set of initial values of the density field suitable for L-PICOLA, we modify the 2LPTic code [9], and more specifically

the extension in [45], originally produced to include PNG initial conditions. Our modification incorporates the relativistic solutions previously presented in Sec. 2. Specifically, we implement a modification to the kernel of the gravitational potential which meets Poisson's equation at all perturbative orders

$$\nabla^2\phi = \frac{3}{2}\mathcal{H}^2\Omega_m\delta \quad , \tag{3.11}$$

where δ is given by the expression (2.160). The Newtonian potential coincides with the comoving curvature perturbations at first-order, so that at linear level we write

$$\phi_{lin} = \frac{3}{5}Rc \approx -\frac{5}{3}\zeta^{(1)} \, . \tag{3.12}$$

in an equivalence valid for the large scales and early times, where our initial conditions are set.

Since the initial conditions code assumes the Poisson equation as valid at all orders, we introduce to that equality the expressions for the Fourier-space equivalent of the density contrast at second and third order in Eqs. (2.170) and (2.171). By rewriting these contributions in terms of the linear potential we can express the non-linear initial potential as a sum of kernels of up to third order as

$$\phi_{lin} = \phi^{(1)} + \frac{1}{2}\phi^{(2)} + \frac{1}{6}\phi^{(3)} \quad , \tag{3.13}$$

with

$$\phi^{(2)} = -\frac{72}{625}\left[(\nabla\phi_{lin})^2(\frac{5}{12} + f_{\rm NL}) + \phi_{lin}\nabla^2\phi_{lin}(\frac{5}{3} - f_{\rm NL})\right] \tag{3.14}$$

$$\begin{aligned}\phi^{(3)} = &-\frac{972}{15625}\left[2\phi_{lin}(\nabla\phi_{lin})^2\left(g_{\rm NL} - \frac{5}{9}f_{\rm NL} - \frac{25}{54}\right) + \right. \\ &\left.\phi_{lin}^2\nabla^2\phi_{lin}\left(g_{\rm NL} - \frac{10}{3}f_{\rm NL} + \frac{50}{27}\right)\right.\end{aligned} \tag{3.15}$$

It is through these expressions that we modify the 2LPTic code using its own aliases for all of the terms contributing to the matter initial conditions.

3.2.1 The perturbative one-loop power spectrum and bispectrum

As a check-up for the consistency of our simulations at the largest scales, we compare the output power spectrum with the perturbative matter power spectrum at one-loop. Both methods should present the same signal at large scales, while differences are expected at the quasi-linear scales and smaller. The perturbative spectrum is given by

$$P(k,\eta) = P_L + 2P^{(1,3)}(k,\eta) + P^{(2,2)}(k,\eta) \quad , \tag{3.16}$$

where P_L corresponds to the linear contribution and $P^{(1,3)}, P^{(2,2)}$ are the one-loop corrections with contributions of the perturbative second and third order respectively. These can be written as

$$P^{(2,2)}(k,\eta) = 2\int \frac{d^3q}{(2\pi)^3} P_L(q,\eta) P_L(|\boldsymbol{k}-\boldsymbol{q}|,\eta)[F^{(2)}(\boldsymbol{q},\boldsymbol{k}-\boldsymbol{q},\eta)]^2 \quad , \tag{3.17}$$

$$P^{(1,3)}(k,\eta) = 3F^{(1)}(\boldsymbol{k}) P_L(k,\eta) \int \frac{d^3q}{(2\pi)^3} P_L(q,\eta) F^{(3)}(\boldsymbol{k},\boldsymbol{q},-\boldsymbol{q},\eta) \quad . \tag{3.18}$$

where $F^{(2)}$ and $F^{(3)}$ are kernels with Newtonian and relativistic contributions at second and third order in Fourier space in the Eulerian frame [37], [42].

Additionally, the tree-level bispectrum is defined as

$$B(k_1,k_2,k_3) = 2P_L(k_1,\eta)P_L(k_2,\eta)F^{(2)}(\boldsymbol{k_1},\boldsymbol{k_2}) + (2 \text{ cyclic.}) \quad , \tag{3.19}$$

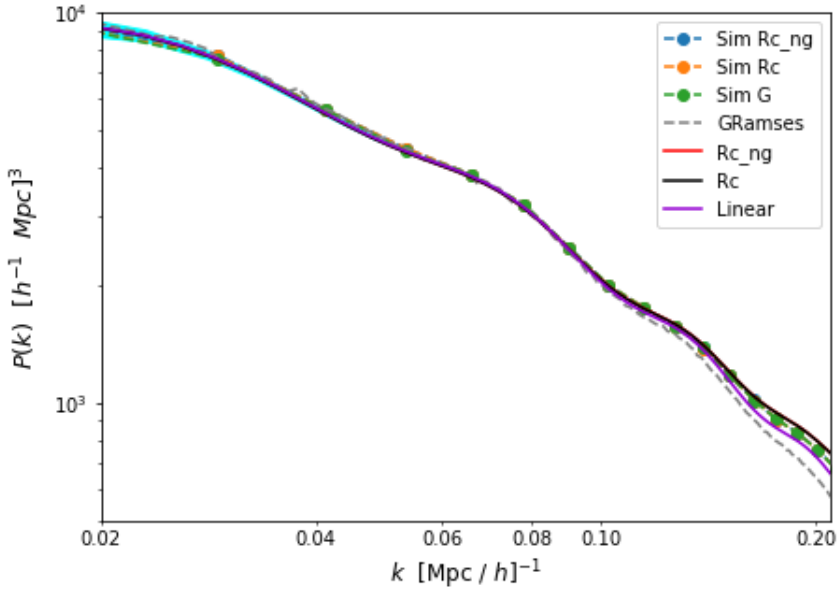

Figure 3.8 Power spectrum from one-loop (lines) and simulations (dots) for relativistic (Rc) contributions, for relativistic plus non-Gaussian contributions (Rc_ng), and Gaussian (i.e. linear; G) initial conditions. The gray line shows a `GRamses` simulation from [12]. The turquoise shaded area represents the variance of a survey with an observable area of $A = 14\ 000\text{deg}^2$ (DESI-like).

where density field kernel can de computed by:

$$F_n^{(s)}(\boldsymbol{q}_1, ..., \boldsymbol{q}_n) = \frac{1}{n!} \frac{\boldsymbol{k} \cdot \boldsymbol{q}_1}{q_1^2} ... \frac{\boldsymbol{k} \cdot \boldsymbol{q}_n}{q_n^2} \tag{3.20}$$

3.3 Power spectrum and bispectrum comparison

We computed the power spectrum and bispectrum from each of the simulations described previously, with the aid of the Pylians (Python libraries for the analysis of numerical simulations) script [46]. In order

to compare the three cases studied, namely the non-Gaussian relativistic, the Gaussian relativistic, and the Gaussian Newtonian case. For all cases, we used the same seed in such a way residuals are due to the intrinsic differences between the models.

In Figure 3.8 we present the power spectrum at $z = 1$ for the L-PICOLA output considering the kernel of Section 3.2 as initial conditions, and the corresponding one-loop power spectrum from cosmological perturbation theory. The 3 cases presented are, *Rc*: relativistic contributions with $f_{\rm NL} = 0$ $g_{\rm NL} = 0$, *Rc_ng*: relativistic contributions with $f_{\rm NL} = -4.2$ $g_{\rm NL} = -7000$, and *G*: The reference Gaussian initial conditions. The plotted scales are limited by the fundamental frequency (The box size) $f_{\rm fun} = 2\pi/Lenght$, which in our specific case is $f_{\rm fun} = 0.002\ h/Mpc$.

The shaded area in this figure represents the variance expected in an DESI-like survey [3] for an observable area of $A = 14\ 000 {\rm deg}^2$ (no particular geometry is considered) computed with the Fisher Matrix from equation (2.254).

We have included in Figures 3.9 and 3.10 the data from the full relativistic code `GRamses` [12]. The suppression observed for the amplitude at low scales is due to the low resolution of that simulation, but we find a good agreement for large scales with our power spectrum (within the errors, and up to $k = 0.07$), where the dominant effect takes place.

In Figure 3.9 we compare the perturbative power spectrum at one-loop, as well as our simulations against the no-wiggle power spectrum. In the lower panel where we present the difference with respect to the Gaussian simulations (green dots). On large scales we find an increment up to 4% (2%) in the amplitude of the power spectrum in relativistic simulations with (without) non-Gaussianity. At smaller scales, i.e. $k0.1\ h\ {\rm Mpc}^{-1}$, find that the discrepancy with the Gaussian simulation vanishes, and recover the well-known divergence of the one-loop perturbative estimation (shown, for example, in Refs. [47], [48]).

In order to ease the small-scale differences, we have included the counterterm c_s^2 of effective field theory (see e.g. [49]) to match the perturbative power spectrum with the numerical (Gaussian) simulations and make it consistent, specially for the small scales. We adopt the

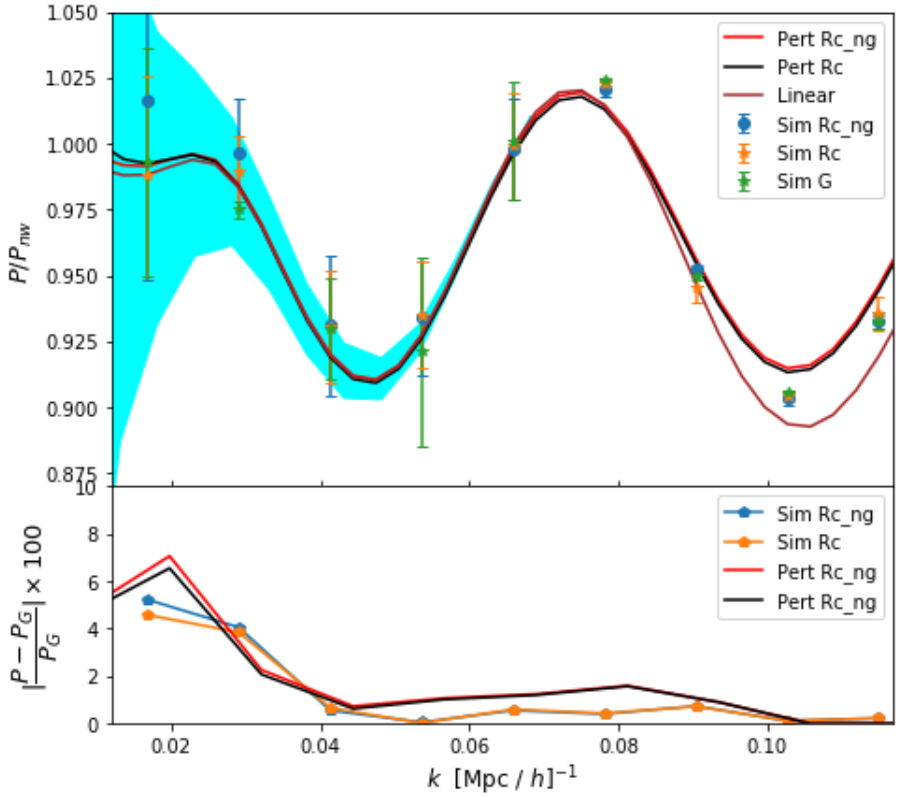

Figure 3.9 Top panel: Power spectrum from one-loop (lines) and simulations (dots) normalized to the no-wiggle power spectrum. Initial conditions are set to Gaussian (G) or including relativistic contributions with (Rc_ng) and without (Rc) primordial non-Gaussianity. The gray line is a GRamses simulation from [12]. The turquoise shade is the same as in Fig. 3.8. The pink line represents a one-loop perturbative powerspectrum corrected through a counter-term addition. Bottom panel: the percentage difference between relativistic and Gaussian cases.

counterterm contribution to the power spectrum at lowest-order from EFT (Effective field theory), defined as:

$$P_{ctr,1loop} \equiv -2k^2 c_s^2 P_{11}. \tag{3.21}$$

As is usual, the counterterm coefficient was calculated after subtracting the one-loop power spectrum from the mean power spectrum from the simulations [50]. The resulting value shown in Figure 3.9 is $c_s^2 = 12.4$. With the one-loop power spectrum corrected in this manner we find that the differences with simulations are below 2 percent throughout the range of scales of Figure 3.9, and that simulations correctly reproduce the one-loop effect of relativistic and non-Gaussianity contributions at large scales.

With the power spectrum in good agreement with the theoretical prediction and fully relativistic simulations, we explore the effects of our model in the bispectrum. For local non-Gaussianities and at leading order in relativistic effects, we find that the amplitude of the bispectrum is most prominent in the *squeezed* configuration [51]. In Figure 3.10 we present the bispectrum as a function of scale, for triangles with sides $k_1 = k_2 = k$ and $k_3 = 0.013k$. Also, the shaded area around the tree-level bispectrum in this figure represents the variance expected in an DESI-like survey [3] for an observable area of $A = 14\ 000\text{deg}^2$ (no particular geometry is considered) [52]. The lower panel of that figure shows the relative difference with respect to the Gaussian simulations (green dots). We observe that the difference increases with the size of the triangle. The percentage deviations from the Gaussian amplitude are of order 10% (8%), for the relativistic initial conditions with (without) non-Gaussianity. Note that at small scales, the PNG contribution vanishes, with a feature at small scales also reported in the literature (see e.g. [53]). Once again, for $k0.08\ h\ \text{Mpc}^{-1}$ the perturbative analysis is divergent from the results of simulations.

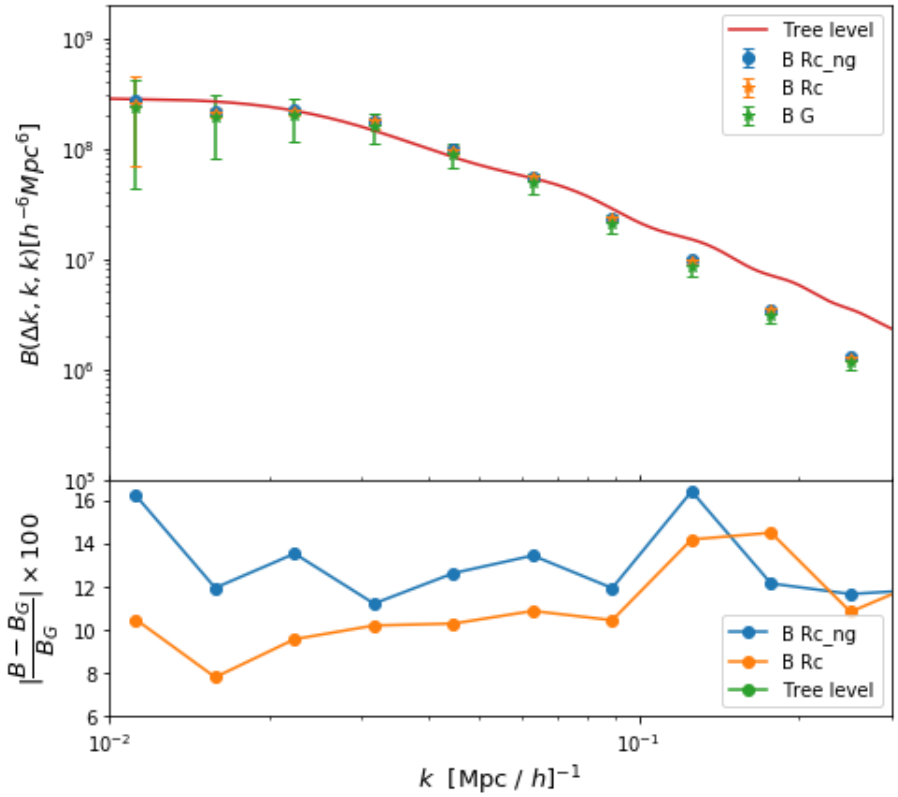

Figure 3.10 Bispectrum sensitivity to GR and PNG effects. Top panel: Bispectrum computed at tree-level in relativistic perturbations (red line, Eq. (3.19)), and from numerical simulations (averaged over 10 realizations) of Gaussian (green dots), relativistic ICs (Orange dots) and the relativistic non-Gaussian (blue dots) cases, at $z = 1$, the blue shadow is the variance from a DESI-like survey. Bottom panel: the percentage difference of the bispectrum for relativistic initial conditions simulations with respect to the Gaussian case. ; Rc_{ng} is for relativistic corrections and non-Gaussianity, Rc for just relativistic corrections.

In Figure 3.11 we show the reduced bispectrum defined as:

$$Q = \frac{B(k_1, k_2, k_3)}{P(k_1)P(k_2) + P(k_2)P(k_3) + P(k_3)P(k_1)} \quad , \tag{3.22}$$

The bottom panel of that figure shows the difference of the studied cases with respect to the Gaussian ICs. We can see that the difference is most prominent at squeezed configurations (low values of the aperture angle θ), which is the reason behind the choice of triangle shape in the plots of Figure 3.10.

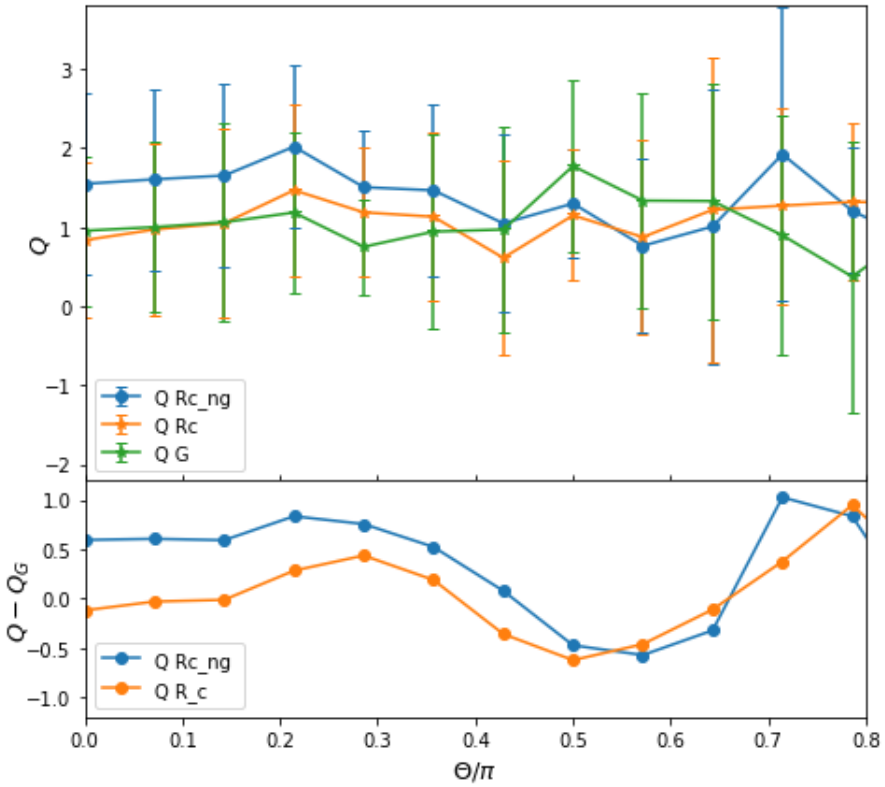

Figure 3.11 Reduced bispectrum sensitivity to GR and PNG effects. Top panel: reduced bispectrum (Eq. (3.22)) for the mean of the 10 realizations of Gaussian simulations (Q_G) and non-Gaussian simulations (Q_R and Q_N) at $z = 1$ with $k_1 = k_2 = 0.01$. Bottom Panel: Difference of the reduced bispectrum for non-Gaussian and relativistic IC simulations with respect to the Gaussian ones.

3.3.1 Voids

The cosmic voids are very low density zones in the universe where the matter is so sparse that the gravitational interaction is almost null. This can help to have a clear detection of the perturbations of the early universe (PNG). We computed the void power spectrum of the voids using PYLIANS code as shown in Figure 3.12 We can observe that the de-

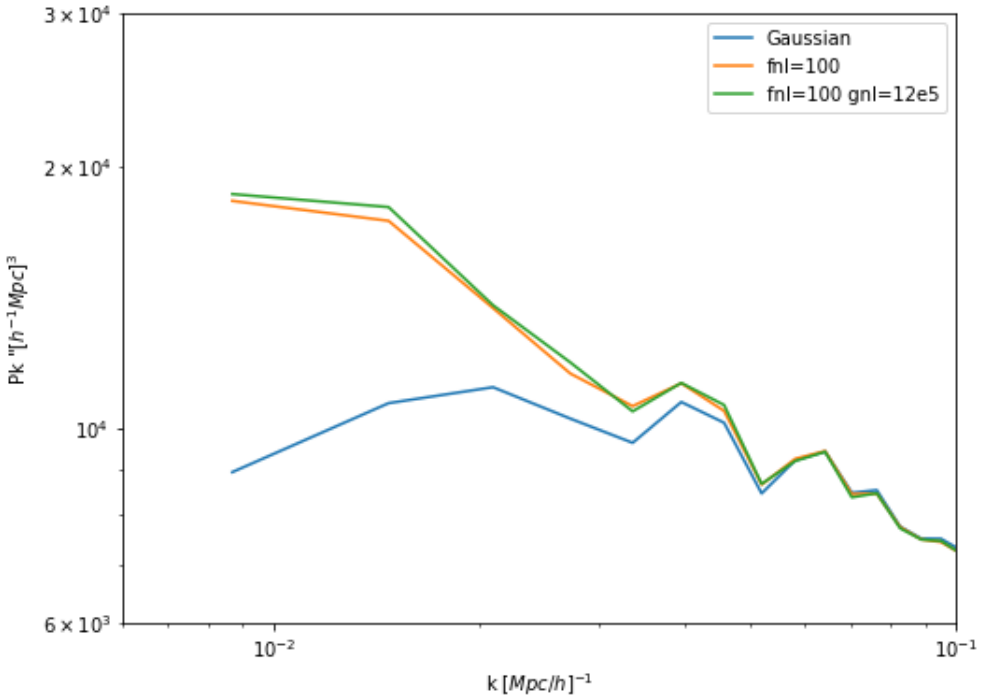

Figure 3.12 Power spectrum of the voids for Gaussian, PNG and PNG with relativistic contributions.

viation for the PNG and PNG with relativistic contributions from the Gaussian simulation is considerably higher than the one of the matter power spectrum of Figure 3.8. This are promising preliminary results because further studies are needed; such as the study of the sensitivity of the void detection and analyze the void mass function that are beyond

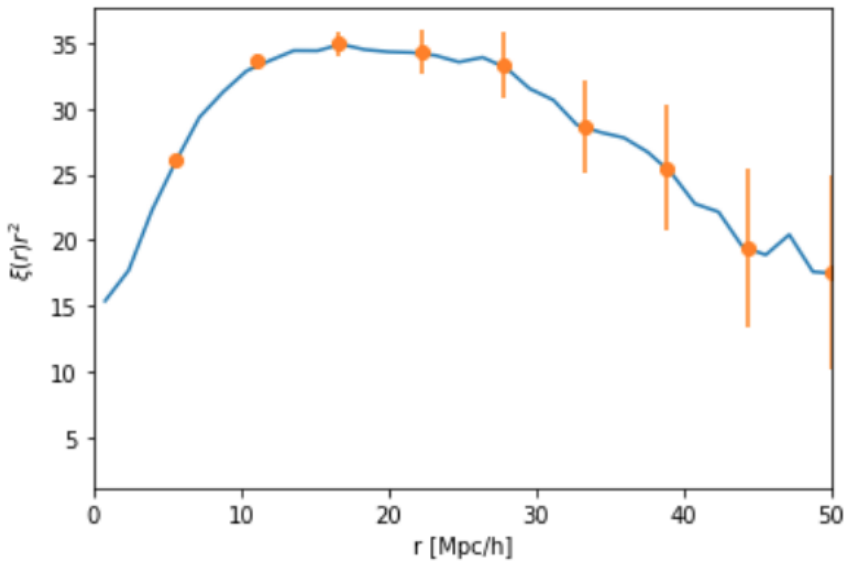

Figure 3.13 2PCF from the DESI Mock Challenge simulation where the error bars are the diagonal from the covariance matrix from RascalC.

the scope of this thesis.

3.4 Mock Challenge participation

We participated in the Mock Challenge Project of the DESI collaboration in estimating covariance matrices and 2PCF using RascalC (Rapid Sampler for Large Covariance Matrices). This package uses the formalism presented previously programmed in C++. In this project we compared this is in contrast with the method where several realizations are used. In Figure (3.14) are the covariance matrices for different methods, C corresponds to a conventional method where several realizations were used to compute the covariance matrix, and M corresponds to the computation with RascalC where just one realization was used. It can be seen that there are no compromising differences.

In Figure 3.13 is the 2PCF with the error bars from the diagonal of the

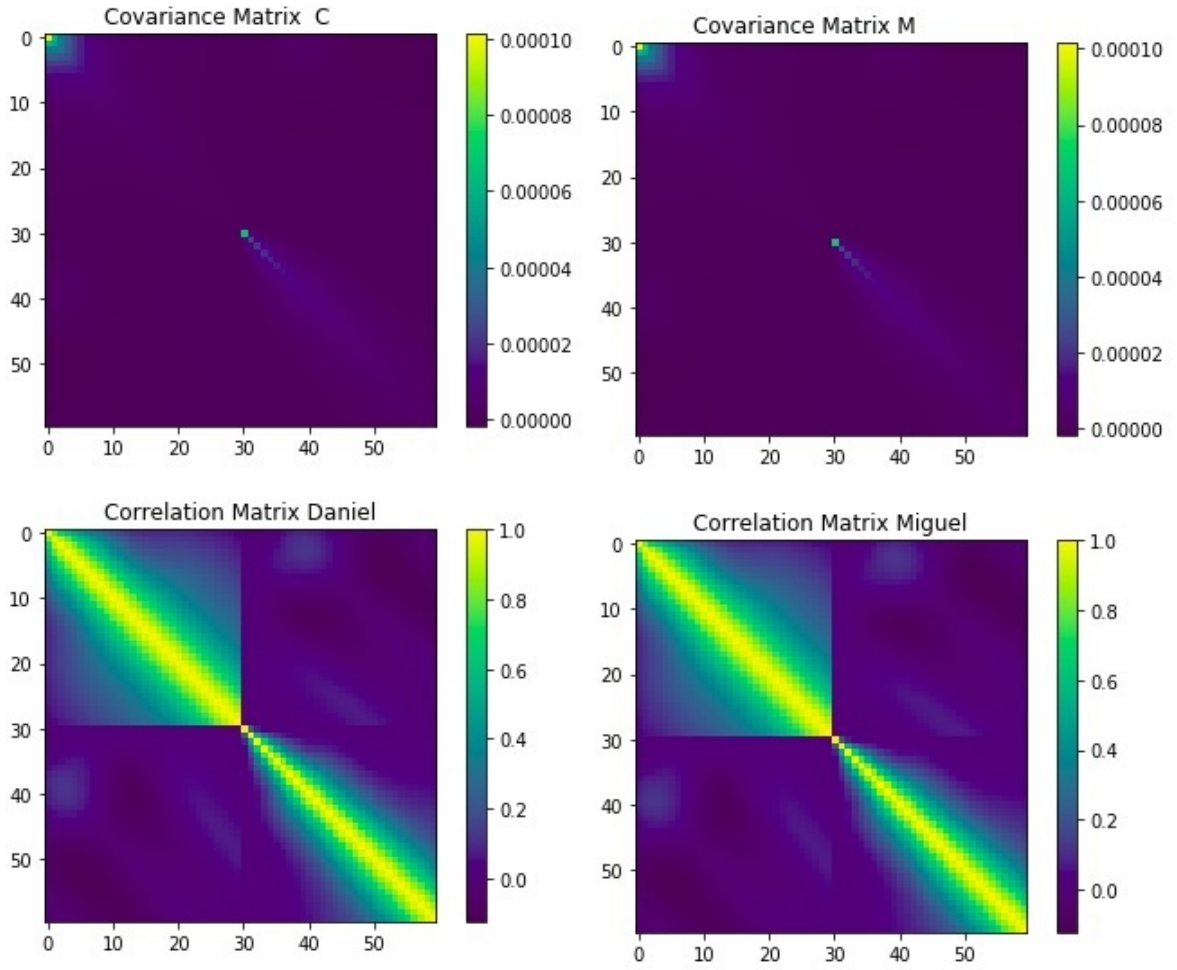

Figure 3.14 Covariance matrix with 2 different method from the DESI Mock Challenge.

covariance matrix. We concluded that the approximation via RascalC method, requires less computational resources and only one realization without loosing much accuracy [4].

Chapter Four

Conclusions and future work

The cosmological simulations have been an important tool to analyze different model varying the cosmological ingredients. In this work we produced L-PICOLA simulations with an input from purely relativistic contributions, as well as from primordial non-Gaussianity, introduced through a modification to the initial conditions provided by the 2LPTic code. The input is given in terms of the gravitational potential kernel, which for our work takes corrections at 1-loop including the relativistic terms and primordial non-Gaussianities from $f_{\rm NL}$ and $g_{\rm NL}$ on the local configuration. Using the limit values of the PNG parameters, as imposed by Planck satellite observations [54], we find higher percentage deviation from the Gaussian case in the bispectrum (as shown in Figures 3.10 and 3.11) than for the power spectrum (Figure 3.9). Similar differences are obtained when considering exclusively relativistic contributions without primordial non-Gaussianity. The most significant deviations from the Gaussian case were detected at larges scales ($k < 0.05$), and for the squeezed triangle configurations, as expected.

The consistency of the numerical simulations with the 1-loop analytic corrections, and with fully relativistic simulations, in the matter

power spectrum, allow us to extend the analysis of a relativistic and non-Gaussian signal to smaller scales. The presented technique can, of course, be used to include non-Gaussianities in other configurations (e.g. equilateral), via the 2LPTic prescriptions. We thus have at hand a practical tool to incorporate both the relativistic contributions as well as the correct (gauge-invariant) input from Primordial non-Gaussianity in the initial conditions of codes like L-PICOLA and GADGET-2, as well as other Nbody codes (e.g. [38], [55]), and even hydrodynamical codes (e.g. [39]), in order to capture the effects in the large scale structure observables. The modifications are public in a GitHub repository in *https://github.com/miguelevargas/lpicola_mod* and is available upon request.

While the above results remain within the variance error of the present galaxy surveys, a more refined error analysis can be employed in order to have a better control of errors for the power spectrum and bispectrum. For example, one can use simulations with inverted phases and look at the relation of the power spectrum and its statistical properties with the covariance matrix [56].

Regarding the contribution in the DESI Mock Challenge project, the method of [52], has shown a good agreement with the usual covariance matrix computation in less time with less realizations. This is an important improvement for the new era of precision cosmology where simulations of high resolutions are needed and conventional statistical methods are not sufficient to process big data amounts in a reasonable time.

We explained also how not all the amplitudes in power spectrum may be due physical effects, there are several numerical effects that have to be analyzed before to make a physical interpretation. Specifically in this work, the small scales were the more affected due the numerical methods that are used in the code, similar studies may be done for adaptive-mesh codes, for example Gadget-2.

4.1 Future research

There are a variety of applications and future possible work derived from this Thesis. After several realizations, one can compute the covariance matrix of the relativistic and non-Gaussian matter spectrum, and observe the scale and amplitude of mode-mixing [57]–[59] to quantify the impact in the correlation between scales.

On the other hand, through a galaxy occupation method (such as HOD [60]), one can probe the galaxy bias parameters which modulate the contribution of the relativistic and PNG terms in the powers spectrum (see e.g. [61]–[63]) and forecast constraints to PNG parameters from the resulting polyspectra (see e.g. [64]).

Similarly, one can study how these contributions change the evolution inside the voids; because of the low density inside of them, primordial effects can be maintained more prominently than in zones with high matter density, where the non-linearities of matter due evolution as minimal. This may be analyzed in the power spectrum and bispectrum (see e.g. [65], [66]).

Also, having more computational resources, there may be full-GR simulations with the PNG initial conditions with codes such as GEVOLUTION and GRAMSES. All these tasks and improvements may be studied in future works.

REFERENCES

[1] E. Sefusatti and E. Komatsu, "Bispectrum of galaxies from high-redshift galaxy surveys: Primordial non-gaussianity and nonlinear galaxy bias," *Physical Review D*, vol. 76, no. 8, Oct. 2007, ISSN: 1550-2368. DOI: 10.1103/physrevd.76.083004. [Online]. Available: http://dx.doi.org/10.1103/PhysRevD.76.083004.

[2] M. Enrıquez, J. C. Hidalgo, and O. Valenzuela, "Including relativistic and primordial non-Gaussianity contributions in cosmological simulations by modifying the initial conditions," *JCAP*, vol. 03, no. 03, p. 048, 2022. DOI: 10.1088/1475-7516/2022/03/048. arXiv: 2109.13364 [astro-ph.CO].

[3] DESI Collaboration *et al.*, "The desi experiment part i: Science,targeting, and survey design," *arXiv e-prints*, arXiv:1611.00036, arXiv:1611.00036, Oct. 2016. arXiv: 1611.00036 [astro-ph.IM].

[4] D. Collaboration, vol. 164, no. 5, p. 207, Oct. 2022. DOI: 10.3847/1538-3881/ac882b. [Online]. Available: https://dx.doi.org/10.3847/1538-3881/ac882b.

[5] A. Blanchard, S. Camera, C. Carbone, *et al.*, "Euclid preparation," *Astronomy & Astrophysics*, vol. 642, A191, Oct. 2020, ISSN: 1432-0746. DOI: 10.1051/0004-6361/202038071. [Online]. Available: http://dx.doi.org/10.1051/0004-6361/202038071.

[6] V. Springel, "The cosmological simulation code gadget-2," *Monthly Notices of the Royal Astronomical Society*, vol. 364, no. 4, pp. 1105–1134, Dec. 2005, ISSN: 1365-2966. DOI: 10.1111/j.1365-2966.2005.

09655.x. [Online]. Available: http://dx.doi.org/10.1111/j.1365-2966.2005.09655.x.

[7] C. Howlett, M. Manera, and W. J. Percival, "L-PICOLA: A parallel code for fast dark matter simulation," *Astronomy and Computing*, vol. 12, pp. 109–126, Sep. 2015. DOI: 10.1016/j.ascom.2015.07.003. arXiv: 1506.03737 [astro-ph.CO].

[8] S. Tassev, M. Zaldarriaga, and D. Eisenstein, "Solving Large Scale Structure in Ten Easy Steps with COLA," *JCAP*, vol. 06, p. 036, 2013. DOI: 10.1088/1475-7516/2013/06/036. arXiv: 1301.0322 [astro-ph.CO].

[9] M. Crocce, S. Pueblas, and R. Scoccimarro, *2LPTIC: 2nd-order Lagrangian Perturbation Theory Initial Conditions*, Jan. 2012. ascl: 1201.005.

[10] O. Hahn and T. Abel, "Multi-scale initial conditions for cosmological simulations,", vol. 415, no. 3, pp. 2101–2121, Aug. 2011. DOI: 10.1111/j.1365-2966.2011.18820.x. arXiv: 1103.6031 [astro-ph.CO].

[11] J. Adamek, D. Daverio, R. Durrer, and M. Kunz, "gevolution: a cosmological N-body code based on General Relativity," *"JCAP"*, vol. 2016, no. 7, 053, p. 053, Jul. 2016. DOI: 10.1088/1475-7516/2016/07/053. arXiv: 1604.06065 [astro-ph.CO].

[12] C. Barrera-Hinojosa and B. Li, "GRAMSES: a new route to general relativistic N-body simulations in cosmology. Part I. Methodology and code description," *"JCAP"*, vol. 2020, no. 1, 007, p. 007, Jan. 2020. DOI: 10.1088/1475-7516/2020/01/007. arXiv: 1905.08890 [astro-ph.CO].

[13] J. L. Cervantes-Cota and G. Smoot, "Cosmology today-A brief review," *AIP Conf. Proc.*, vol. 1396, no. 1, L. A. Urena-Lopez, H. A. Morales-Tecotl, R. Linares-Romero, E. Santos-Rodriguez, and S. Estrada-Jimenez, Eds., pp. 28–52, 2011. DOI: 10.1063/1.3647524. arXiv: 1107.1789 [astro-ph.CO].

[14] E. Hubble, "A relation between distance and radial velocity among extra-galactic nebulae," *Proceedings of the National Academy of Sciences*, vol. 15, no. 3, pp. 168–173, 1929, ISSN: 0027-8424. DOI: 10.1073/pnas.15.3.168.

[15] A. A. Penzias and R. W. Wilson, "A Measurement of Excess Antenna Temperature at 4080 Mc/s.,", vol. 142, pp. 419–421, Jul. 1965. DOI: 10.1086/148307.

[16] O. Lahav and A. R. Liddle, "The Cosmological Parameters 2010," *arXiv e-prints*, arXiv:1002.3488, arXiv:1002.3488, Feb. 2010. arXiv: 1002.3488 [astro-ph.CO].

[17] J.-P. Luminet, *Lemaitre's big bang*, 2015. arXiv: 1503.08304 [physics.hist].

[18] L. Hernquist, N. Katz, D. H. Weinberg, and J. Miralda-Escudé, "The lyman-alpha forest in the cold dark matter model," *The Astrophysical Journal*, vol. 457, no. 2, Feb. 1996. DOI: 10.1086/309899.

[19] L. Damone, M. Barbagallo, M. Mastromarco, *et al.*, "^{7}Be$(n,p)^{7}$Li Reaction and the cosmological lithium problem: Measurement of the cross section in a wide energy range at n$_{t}ofatcern$," *Phys. Rev. Lett.*, vol. 121, p. 042 701, 4 Jul. 2018.

[20] H. Bondi and T. Gold, "The Steady-State Theory of the Expanding Universe," *Monthly Notices of the Royal Astronomical Society*, vol. 108, no. 3, pp. 252–270, Jun. 1948, ISSN: 0035-8711. DOI: 10.1093/mnras/108.3.252.

[21] T. L. Chow, *Gravity, Black Holes, and the Very Early Universe*. New York : Springer, 2008.

[22] F. Pacucci, "The first black holes in the cosmic dark ages," Ph.D. dissertation, Jan. 2016. DOI: 10.5281/zenodo.164889.

[23] P. Murdin, *Encyclopedia of astronomy and astrophysics*. 2001.

[24] S. van den Bergh, "The early history of dark matter," *Publications of the Astronomical Society of the Pacific*, vol. 111, no. 760,

pp. 657–660, Jun. 1999, ISSN: 1538-3873. DOI: 10.1086/316369. [Online]. Available: http://dx.doi.org/10.1086/316369.

[25] A. Doroshkevich, V. Lukash, and E. Mikheeva, "A solution to the problems of cusps and rotation curves in dark matter halos in the cosmological standard model," *Physics-uspekhi - PHYS-USP*, vol. 55, Sep. 2012. DOI: 10.3367/UFNr.0182.201201a.0003.

[26] D. P. Stark, A. J. Bunker, R. S. Ellis, L. P. Eyles, and M. Lacy, "A new measurement of the stellar mass density at z5: Implications for the sources of cosmic reionization," *The Astrophysical Journal*, vol. 659, no. 1, pp. 84–97, Apr. 2007, ISSN: 1538-4357. DOI: 10.1086/511325. [Online]. Available: http://dx.doi.org/10.1086/511325.

[27] V. Vavryčuk, "Universe opacity and Type Ia supernova dimming," *Monthly Notices of the Royal Astronomical Society: Letters*, vol. 489, no. 1, pp. L63–L68, Aug. 2019, ISSN: 1745-3925. DOI: 10.1093/mnrasl/slz128.

[28] F. Bezrukov and M. Shaposhnikov, "The standard model higgs boson as the inflaton," *Physics Letters B*, vol. 659, no. 3, pp. 703–706, Jan. 2008, ISSN: 0370-2693. DOI: 10.1016/j.physletb.2007.11.072.

[29] E. Villa, S. Matarrese, and D. Maino, "Cosmological dynamics: from the Eulerian to the Lagrangian frame. Part I. Newtonian approximation," *"JCAP"*, vol. 2014, no. 6, 041, p. 041, Jun. 2014. DOI: 10.1088/1475-7516/2014/06/041. arXiv: 1403.6806 [astro-ph.CO].

[30] G. F. R. Ellis, "Relativistic cosmology," *Proc. Int. Sch. Phys. Fermi*, vol. 47, pp. 104–182, 1971. DOI: 10.1007/s10714-009-0760-7.

[31] G. F. R. Ellis and M. Bruni, "Covariant and gauge-invariant approach to cosmological density fluctuations," *Phys. Rev. D*, vol. 40, pp. 1804–1818, 6 Sep. 1989. DOI: 10.1103/PhysRevD.40.1804. [Online]. Available: https://link.aps.org/doi/10.1103/PhysRevD.40.1804.

[32] M. Bruni, P. K. S. Dunsby, and G. F. R. Ellis, "Cosmological Perturbations and the Physical Meaning of Gauge-invariant Variables,", vol. 395, p. 34, Aug. 1992. DOI: 10.1086/171629.

[33] G. F. R. Ellis, M. Bruni, and J. Hwang, "Density-gradient-vorticity relation in perfect-fluid robertson-walker perturbations," *Phys. Rev. D*, vol. 42, pp. 1035–1046, 4 Aug. 1990. DOI: 10.1103/PhysRevD.42.1035. [Online]. Available: https://link.aps.org/doi/10.1103/PhysRevD.42.1035.

[34] M. Bruni, J. C. Hidalgo, and D. Wands, "Einstein's signature in cosmological large-scale structure," *The Astrophysical Journal*, vol. 794, no. 1, p. L11, Sep. 2014. DOI: 10.1088/2041-8205/794/1/l11. [Online]. Available: https://doi.org/10.1088/2041-8205/794/1/l11.

[35] F. Bernardeau, S. Colombi, E. Gaztañaga, and R. Scoccimarro, "Large-scale structure of the universe and cosmological perturbation theory," *Physics Reports*, vol. 367, no. 1-3, pp. 1–248, Sep. 2002, ISSN: 0370-1573. DOI: 10.1016/s0370-1573(02)00135-7. [Online]. Available: http://dx.doi.org/10.1016/S0370-1573(02)00135-7.

[36] M. Bruni, J. C. Hidalgo, N. Meures, and D. Wands, "Non gaussian initial conditions in Λcdm: Newtonian, relativistic and primordial contributions," *The Astrophysical Journal*, vol. 785, no. 1, p. 2, Mar. 2014, ISSN: 1538-4357. DOI: 10.1088/0004-637x/785/1/2. [Online]. Available: http://dx.doi.org/10.1088/0004-637X/785/1/2.

[37] H. A. Gressel and M. Bruni, "$f_{NL}-g_{NL}$ mixing in the matter density field at higher orders," *JCAP*, vol. 06, p. 016, 2018. DOI: 10.1088/1475-7516/2018/06/016. arXiv: 1712.08687 [astro-ph.CO].

[38] R. Teyssier, "Cosmological hydrodynamics with adaptive mesh refinement. a new high resolution code called ramses," *Astronomy & Astrophysics*, vol. 385, pp. 337–364, Apr. 2002. DOI: 10.1051/0004-6361:20011817. arXiv: astro-ph/0111367 [astro-ph].

[39] R. Weinberger, V. Springel, and R. Pakmor, "The arepo public code release," *The Astrophysical Journal Supplement Series*, vol. 248, no. 2, p. 32, Jun. 2020, ISSN: 1538-4365. DOI: 10.3847/1538-4365/ab908c. [Online]. Available: http://dx.doi.org/10.3847/1538-4365/ab908c.

[40] A. J. Christopherson, J. C. Hidalgo, C. Rampf, and K. A. Malik, "Second-order cosmological perturbation theory and initial conditions for N -body simulations," *"Phys. Rev. D"*, vol. 93, no. 4, 043539, p. 043 539, Feb. 2016. DOI: 10.1103/PhysRevD.93.043539. arXiv: 1511.02220 [gr-qc].

[41] I. Delgado Gaspar and T. Buchert, "Lagrangian theory of structure formation in relativistic cosmology. vi. comparison with szekeres exact solutions," *arXiv e-prints*, arXiv:2009.06339, arXiv:2009.06339, Sep. 2020. arXiv: 2009.06339 [gr-qc].

[42] R. Martinez-Carrillo, J. De-Santiago, J. C. Hidalgo, and K. A. Malik, "Relativistic and non-Gaussianity contributions to the one-loop power spectrum," *JCAP*, vol. 04, p. 028, 2020. DOI: 10.1088/1475-7516/2020/04/028. arXiv: 1911.04359 [astro-ph.CO].

[43] T. Matsubara, "Resumming cosmological perturbations via the lagrangian picture: One-loop results in real space and in redshift space," *Physical Review D*, vol. 77, no. 6, Mar. 2008, ISSN: 1550-2368. DOI: 10.1103/physrevd.77.063530. [Online]. Available: http://dx.doi.org/10.1103/PhysRevD.77.063530.

[44] K. Markovic, B. Bose, and A. Pourtsidou, "Assessing non-linear models for galaxy clustering I: unbiased growth forecasts from multipole expansion," *The Open Journal of Astrophysics*, vol. 2, no. 1, 13, p. 13, Nov. 2019. DOI: 10.21105/astro.1904.11448. arXiv: 1904.11448 [astro-ph.CO].

[45] R. Scoccimarro, L. Hui, M. Manera, and K. C. Chan, "Large-scale bias and efficient generation of initial conditions for nonlocal primordial non-Gaussianity," *"Phys. Rev. D"*, vol. 85, no. 8, 083002,

p. 083 002, Apr. 2012. DOI: 10.1103/PhysRevD.85.083002. arXiv: 1108.5512 [astro-ph.CO].

[46] F. Villaescusa-Navarro, *Pylians: Python libraries for the analysis of numerical simulations*, Nov. 2018. ascl: 1811.008.

[47] J. Carlson, M. White, and N. Padmanabhan, "A critical look at cosmological perturbation theory techniques," *Phys. Rev. D*, vol. 80, p. 043 531, 2009. DOI: 10.1103/PhysRevD.80.043531. arXiv: 0905.0479 [astro-ph.CO].

[48] Z. Vlah, U. Seljak, and T. Baldauf, "Lagrangian perturbation theory at one loop order: Successes, failures, and improvements," *"Phys. Rev. D"*, vol. 91, no. 2, 023508, p. 023 508, Jan. 2015. DOI: 10.1103/PhysRevD.91.023508. arXiv: 1410.1617 [astro-ph.CO].

[49] L. Fonseca de la Bella, D. Regan, D. Seery, and S. Hotchkiss, "The matter power spectrum in redshift space using effective field theory," *Journal of Cosmology and Astroparticle Physics*, vol. 2017, Apr. 2017. DOI: 10.1088/1475-7516/2017/11/039.

[50] T. Baldauf, L. Mercolli, and M. Zaldarriaga, "Effective field theory of large scale structure at two loops: The apparent scale dependence of the speed of sound," *Phys. Rev. D*, vol. 92, p. 123 007, 12 Dec. 2015. DOI: 10.1103/PhysRevD.92.123007. [Online]. Available: https://link.aps.org/doi/10.1103/PhysRevD.92.123007.

[51] S. Matarrese, L. Pilo, and R. Rollo, "Resilience of long modes in cosmological observables," *JCAP*, vol. 01, p. 062, 2021. DOI: 10.1088/1475-7516/2021/01/062. arXiv: 2007.08877 [astro-ph.CO].

[52] O. H. E. Philcox, "Cosmology without window functions. ii. cubic estimators for the galaxy bispectrum," *Phys. Rev. D*, vol. 104, p. 123 529, 12 Dec. 2021. DOI: 10.1103/PhysRevD.104.123529. [Online]. Available: https://link.aps.org/doi/10.1103/PhysRevD.104.123529.

[53] E. Sefusatti, M. Crocce, and V. Desjacques, "The matter bispectrum in N-body simulations with non-Gaussian initial conditions,"

Monthly Notices of the Royal Astronomical Society, vol. 406, no. 2, pp. 1014–1028, Aug. 2010. DOI: 10.1111/j.1365-2966.2010.16723.x. arXiv: 1003.0007 [astro-ph.CO].

[54] Planck Collaboration, N. Aghanim, Y. Akrami, M. Ashdown, J. Aumont, and et al., "Planck 2018 results. VI. Cosmological parameters,", vol. 641, A6, A6, Sep. 2020. DOI: 10.1051/0004-6361/201833910. arXiv: 1807.06209 [astro-ph.CO].

[55] Y. Feng, M.-Y. Chu, U. Seljak, and P. McDonald, "Fastpm: A new scheme for fast simulations of dark matter and haloes," *Monthly Notices of the Royal Astronomical Society*, vol. 463, no. 3, pp. 2273–2286, Aug. 2016, ISSN: 1365-2966. DOI: 10.1093/mnras/stw2123. [Online]. Available: http://dx.doi.org/10.1093/mnras/stw2123.

[56] A. Klypin and F. Prada, "Dark matter statistics for large galaxy catalogues: Power spectra and covariance matrices," *Monthly Notices of the Royal Astronomical Society*, vol. 478, no. 4, pp. 4602–4621, Jun. 2018, ISSN: 1365-2966. DOI: 10.1093/mnras/sty1340. [Online]. Available: http://dx.doi.org/10.1093/mnras/sty1340.

[57] K. C. Chan and L. Blot, "Assessment of the Information Content of the Power Spectrum and Bispectrum," *Phys. Rev. D*, vol. 96, no. 2, p. 023 528, 2017. DOI: 10.1103/PhysRevD.96.023528. arXiv: 1610.06585 [astro-ph.CO].

[58] D. Gualdi, H. Gil-Marín, R. L. Schuhmann, M. Manera, B. Joachimi, and O. Lahav, "Enhancing boss bispectrum cosmological constraints with maximal compression," *Monthly Notices of the Royal Astronomical Society*, vol. 484, no. 3, pp. 3713–3730, Jan. 2019, ISSN: 1365-2966. DOI: 10.1093/mnras/stz051. [Online]. Available: http://dx.doi.org/10.1093/mnras/stz051.

[59] M. (Wang, W. J. Percival, S. Avila, R. Crittenden, and D. Bianchi, "Cosmological inference from galaxy-clustering power spectrum: Gaussianization and covariance decomposition," *Monthly Notices of the Royal Astronomical Society*, vol. 486, no. 1, pp. 951–965,

Mar. 2019, ISSN: 1365-2966. DOI: 10.1093/mnras/stz829. [Online]. Available: http://dx.doi.org/10.1093/mnras/stz829.

[60] R. Voivodic and A. Barreira, "Responses of Halo Occupation Distributions: a new ingredient in the halo model & the impact on galaxy bias," *JCAP*, vol. 05, p. 069, 2021. DOI: 10.1088/1475-7516/2021/05/069. arXiv: 2012.04637 [astro-ph.CO].

[61] P. McDonald, "Primordial non-Gaussianity: Large-scale structure signature in the perturbative bias model," *Phys. Rev. D*, vol. 78, no. 12, 123519, p. 123 519, Dec. 2008. DOI: 10.1103/PhysRevD.78.123519. arXiv: 0806.1061 [astro-ph].

[62] A. Barreira, "On the impact of galaxy bias uncertainties on primordial non-gaussianity constraints," *Journal of Cosmology and Astroparticle Physics*, vol. 2020, no. 12, pp. 031–031, Dec. 2020. DOI: 10.1088/1475-7516/2020/12/031. [Online]. Available: https://doi.org/10.1088/1475-7516/2020/12/031.

[63] R. Martinez-Carrillo, J. C. Hidalgo, K. A. Malik, and A. Pourtsidou, "Contributions from primordial non-Gaussianity and General Relativity to the galaxy power spectrum," Jul. 2021. arXiv: 2107.10815 [astro-ph.CO].

[64] M. Tellarini, A. J. Ross, G. Tasinato, and D. Wands, "Galaxy bispectrum, primordial non-Gaussianity and redshift space distortions," *"JCAP"*, vol. 2016, no. 6, 014, p. 014, Jun. 2016. DOI: 10.1088/1475-7516/2016/06/014. arXiv: 1603.06814 [astro-ph.CO].

[65] M. Jaber, M. Peper, W. A. Hellwing, M. A. Aragon-Calvo, and O. Valenzuela, "Hierarchical structure of the cosmic web and galaxy properties," Apr. 2023. arXiv: 2304.14387 [astro-ph.GA].

[66] N. Hamaus, M.-C. Cousinou, A. Pisani, M. Aubert, S. Escoffier, and J. Weller, vol. 2017, no. 07, p. 014, Jul. 2017. DOI: 10.1088/1475-7516/2017/07/014. [Online]. Available: https://dx.doi.org/10.1088/1475-7516/2017/07/014.

DRA. LINA ANDREA RIVILLAS ACEVEDO
COORDINADORA DEL POSGRADO EN CIENCIAS
PRESENTE

Atendiendo a la solicitud para emitir DICTAMEN sobre la revisión de la TESIS titulada: **Correlación en simulaciones cosmológicas**, que presenta el alumno **Miguel Enríquez Vargas (10021244)** para obtener el título de **Doctor en Ciencias.**

Nos permitimos informarle que nuestro voto es:

NOMBRE	DICTAMEN	FIRMA
Dr. Rolando Pérez Ávarez CInC – UAEM	APROBADO	
Dr. Markus Franziskus Muller CInC – UAEM	APROBADO	
Dr. Nodari Vakhania Maizuradze CInC – UAEM	APROBADO	
Dr. Octavio Valenzuela Tijerino ICF - UNAM	APROBADO	
Dr. Lorena Díaz González CInC - UAEM	APROBADO	
Dr. Raúl Salgado García CInC – UAEM	APROBADO	
Dr. Juan Carlos Hidalgo Cuellar ICF – UNAM	APROBADO	

Se expide el presente documento firmado electrónicamente de conformidad con el ACUERDO GENERAL PARA LA CONTINUIDAD DEL FUNCIONAMIENTO DE LA UNIVERSIDAD AUTÓNOMA DEL ESTADO DE MORELOS DURANTE LA EMERGENCIA SANITARIA PROVOCADA POR EL VIRUS SARS-COV2 (COVID-19) emitido el 27 de abril del 2020.

El presente documento cuenta con la firma electrónica UAEM del funcionario universitario competente, amparada por un certificado vigente a la fecha de su elaboración y es válido de conformidad con los LINEAMIENTOS EN MATERIA DE FIRMA ELECTRÓNICA PARA LA UNIVERSIDAD AUTÓNOMA DE ESTADO DE MORELOS emitidos el 13 de noviembre del 2019 mediante circular No. 32.

Sello electrónico

MARKUS FRANZISKUS MULLER | Fecha:2023-05-23 14:01:09 | Firmante

aAzjR/O3rTQoR/IGFZiQymJXf2TzjJL7cXMNBPrhghEyV0ulAeoY50zppOy3Y/XmU011zlt6lCRLPT2K2n5x3J3lpEgv9zdB5XVTJnx3QkjZ8zJlhjhLZL2Obo/pGRr74CY1eHFEsQCF
WPbi4URyK4OH2aAG/J8g61IQnOu5jsMDjtj9DuelTNtfI5oQ3kfvvtye+tF4c8XOU0ORpe7nFjeZIamhyCffH+DIWs/wsCFPNETtpDdQHzfXTD6Ljqs1CkvmQDZffIYRWU9oYkx7mBtO
tbuqUltQJK7v1Us46uRD9GbMRKbAp/GuzOZJoQT/99te8XZs4jcsS091mgkNCw==

JOSÉ OCTAVIO VALENZUELA TIJERINO | Fecha:2023-05-23 14:12:52 | Firmante

B6AHH/qJM5P0DumrvFdF1OGkc9FVu8+dw76SVI7jdm3DPqQKgfPtCc0W2EvXZ3XUq/rGnPGEOfpzBoLk8hneKfTMnT7r7xbLWr/gYdLkfzASrZX0+0B1v3sN5u/zlGOBmzrcwu0s
VNttH5PW9BORLFG0m6DifWnpHK6Ow8uFZ6zqCAYdM9pt8EP6oqTS4/MR3h0OR00h+kHCcwxluLBeUxfyiESQUSKWyj3qHBCsFkg0BqDEngzZ2f75ziUeiDoMsprG2PODFtPvt
2rE0rJrARLMjnUmCKlD+6wCi2jbWLxCFT7RyeEmBr2BYUAX5uYOSTuLjIFIXxRgyCZiIogaXQ==

ROLANDO PEREZ ALVAREZ | Fecha:2023-05-23 14:37:42 | Firmante

SYqB9wbiFeQ+x8IY11eLQHFBuPoWPxrWv+yWyJuTiLra1JnQbnEpX9VF8wMAEikfRamg2RAL5WpQIffYr2YoPBeeDt39Xp4tKk448mF2dzw72IHsublqUJT1OgsDXVpbeU4yGE
SCGPLvRP0SmvMvC7XdKDeGinBp7aUXtSvoGdr7iAK3cWnma+E/1rI1Isz+ezfPO3d2Y3UbfhQCcDAlZAdlcN6yTfzXhqlufT+V1jr9LTmBsZlFv1nyR6KcPjkCfTfUPT7AH0nRUFWS
C39dt/7VXzxsfB9wSuyvzMOU5vJwKPqSCxzNeSKqLxyVjm9x/GZ886slAM91ihbh7nvA0w==

RAUL SALGADO GARCIA | Fecha:2023-05-24 07:42:32 | Firmante

azESlXx6+jbCphA70R2LjQtWt5BixG3o0mmuIZ4qGWsY/9+GXH82Gxjb2hKnROrDQ681S/eL3XBFunLDDJBIutNkH0cocQyLLxmMXgvUqjGZirE3RtHCRzP68HXxEkAxh5iP0HiU
Y9Hgx2I5h/+L7kjmrYi2im1DtUA6C98m+IGR/FJOfIN7XHh6rber1E0sadSr5OjHPCRc13hM4Wckiis2vfQc30YXdHPDQqjdA9nsf+yaH1LC9612mAHL8EsG7uXAl2RnLapn2yJVKpJr
hGpsjo0YtJXuVYgMCTNPlpAxEgIVKMY+0VqzqH+qvsrBsvvh+CMP0w3V3lK5+Bcohw==

LORENA DIAZ GONZALEZ | Fecha:2023-05-24 11:20:25 | Firmante

wcY1TFtgMWliLSWFfsbKeIP3bsoPfchDyA5z6XdcSKLNADn1Vm1jpDOo6qhbwsg7STy9IrCa/e5HgisF1KZoC09JTiQR4ugwBJSWRCofHXV72cSRzPl+dRSGaRrp7LpxhnRhVetK
I0mqb/hM556gLqHqcUKhq1X84GiDemBrc6sOoRZLEU+OQlkgqS85yK1fsToqHldxEbM+vq8tmFYqqCXypFDqFYxY3OYN9a+XpETL21clKoVYL4REQWxezXJN4i0LSsVXxtZ7wg
N5AOAXsvFGyYYz0Ve4rTjWZmbPTZtpIwTKVws8+xQ7964m7UUr2vIGukiVEehVacOfWENfGQ==

NODARI VAKHANIA MAISURADZE | Fecha:2023-05-25 10:50:44 | Firmante

Dr+8UfOhCwwHeoU7KdodauVgXFGBg/Qfs65IPC27mbjiPYv04u07ElzexG90eHte+XBat0abzDq4RKIQqYkVWr6RKQy7O/wMJ2EijplS1os4UNkNzcn5nBIabCWIsp/XSpv42g5sk+
OvCdwJ+8IVksFeTreC8xt74EX0hR5ll9ZK2r0hAyCw/fO9MWlo9Ico0ZSHJI8fmC15NMowhV3+AKgQN13suHxUT22xAOSAfeNpiMA2Ea01fs0aKk6jo/nnrtMq7ubhWkUmzIENTZL
KCAEGNVc8IfcKNgjMEPVd+SnPQP4VEnD6XibEzzLTYZeZMey4JqEcxGTPwUx64aA6Ag==

JUAN CARLOS HIDALGO CUELLAR | Fecha:2023-05-26 22:37:41 | Firmante

f8LSa5OspmLdmlbBZ4jJdCJiHPQfRFeAyE4g5UoWR7jSkJlrCJwaYJQLifa6GT6calrZ5EDyJBgFI5QBL01M0z6tWUirXNZ8Zv6hgDZdSpzVzagEo/0FfJWu6FOhnbgrDd/fxsdmSrg9
ZYyruMlxIPc4T4v8c6+lf18i3JNPnQBcFtfav85uJn0GLkd9burjU5fgxdXj/HY+5zprZI+NwWXyofkBiHW98/in1sLXYdsW8DF+uuNoI0neBZ8vZVodXsME3CM2CqwyMR+NzgxOffyj25
UnxDG1PIk3HaKKQx9VFkakhR7bBNyGTvGv37wveFFSlgZDreIQIXwQFrXwig==

Puede verificar la autenticidad del documento en la siguiente dirección electrónica o escaneando el código QR ingresando la siguiente clave:

9AhpUPB3b

https://efirma.uaem.mx/noRepudio/ptMZLEP5G7bmv7EqsVz6C7QJjTJG6AVX